AD-A062 299 ARMY ARMAMENT RESEARCH AND DEVELOPMENT COMMAND ABERD--ETC F/G 19/1
OBSERVATIONS OF SHAPED-CHARGE JET/M30 PROPELLANT REACTIONS.(U)
SEP 78 J N MAJERUS, A B MERENDINO

UNCLASSIFIED ARBRL-TR-02108 SBIE-AD-E430 142 NL

1 OF 2
ADA
062299

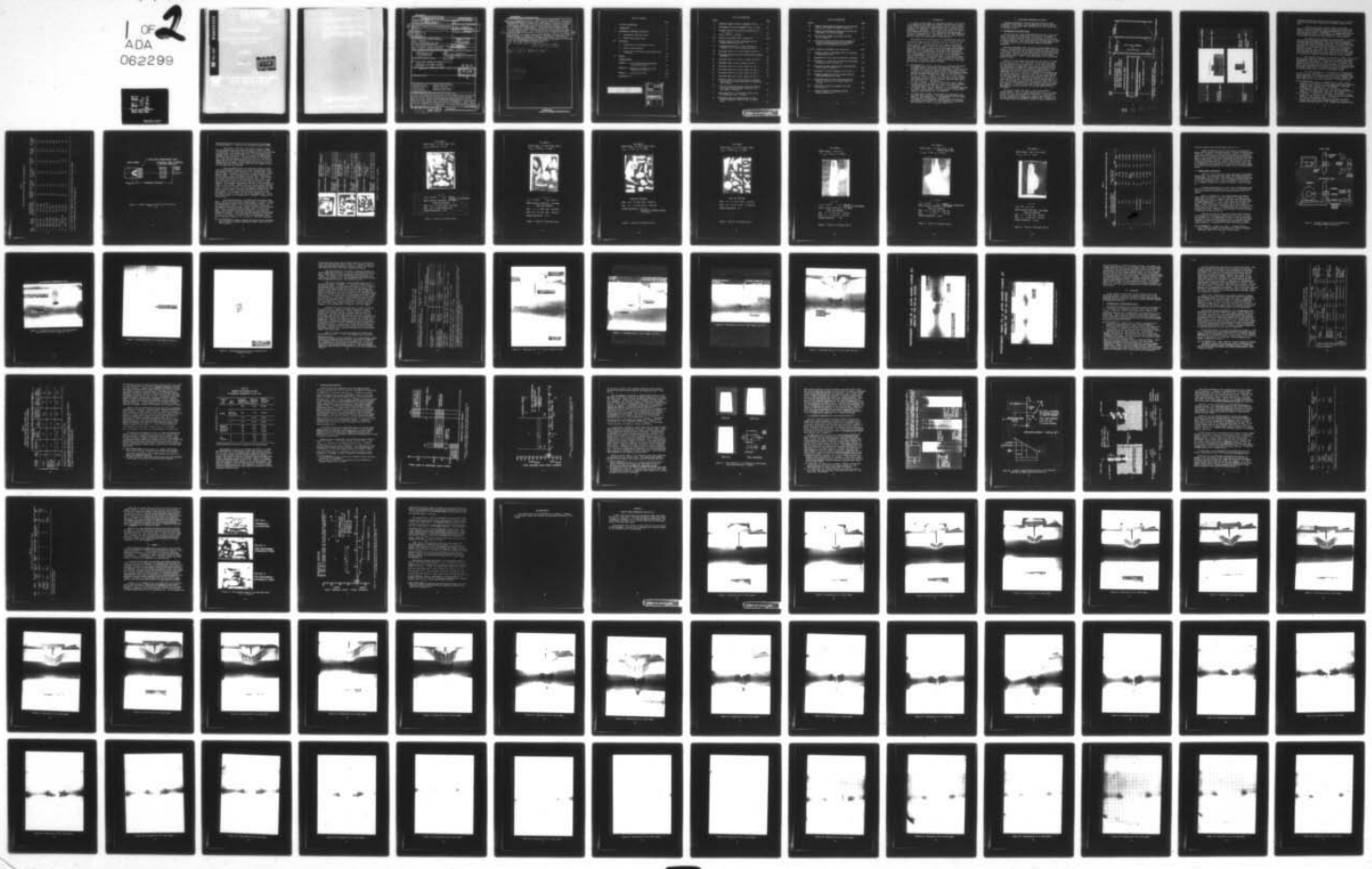

DDC FILE COPY AD A062299

DDC
RECEIVED
DEC 19 1978
B

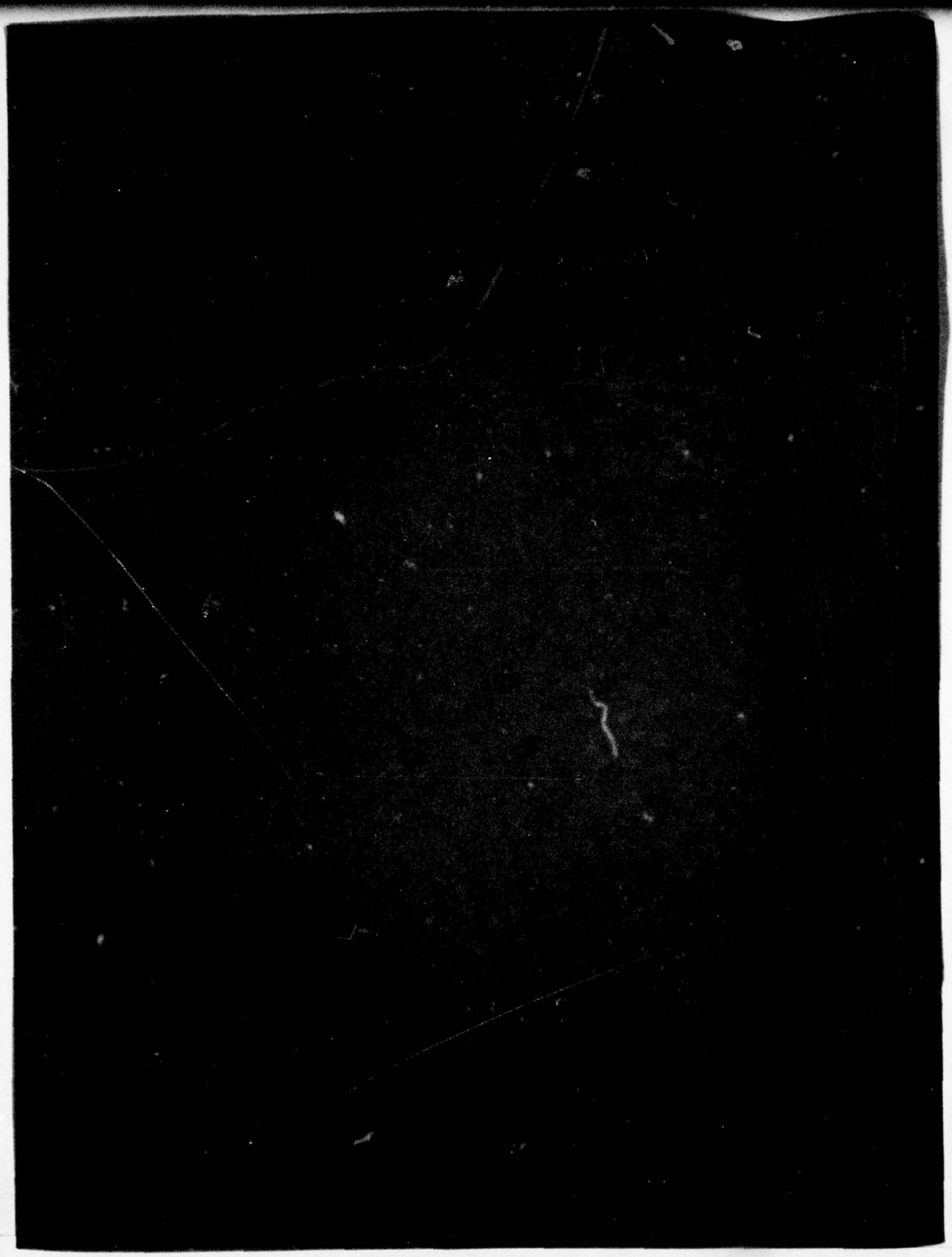

UNCLASSIFIED

SECURITY CLASSIFICATION OF THIS PAGE (When Data Entered)

REPORT DOCUMENTATION PAGE	READ INSTRUCTIONS BEFORE COMPLETING FORM
1. REPORT NUMBER (14) TECHNICAL REPORT ARBRL-TR-02108 / 2. GOVT ACCESSION NO.	3. RECIPIENT'S CATALOG NUMBER (9)
4. TITLE (and Subtitle) (6) OBSERVATIONS OF SHAPED-CHARGE JET/M30 PROPELLANT REACTIONS,	5. TYPE OF REPORT & PERIOD COVERED FINAL Sept. 3
	6. PERFORMING ORG. REPORT NUMBER
7. AUTHOR(s) (10) J.N. Majerus, A.B. Merendino	8. CONTRACT OR GRANT NUMBER(s)
9. PERFORMING ORGANIZATION NAME AND ADDRESS U.S. Army Ballistic Research Laboratory (ATTN: DRDAR-BLT) Aberdeen Proving Ground, MD 21005	10. PROGRAM ELEMENT, PROJECT, TASK AREA & WORK UNIT NUMBERS (16) RDT&E 1L162618AH80
11. CONTROLLING OFFICE NAME AND ADDRESS U.S. Army Armament Research & Development Command U.S. Army Ballistic Research Laboratory (ATTN: DRDAR-BL) Aberdeen Proving Ground, MD 21005	12. REPORT DATE (11) SEPT [redacted] 78 / 13. NUMBER OF PAGES 115
14. MONITORING AGENCY NAME & ADDRESS (if different from Controlling Office) (18) SBIE (12) 116p.	15. SECURITY CLASS. (of this report) UNCLASSIFIED
	15a. DECLASSIFICATION/DOWNGRADING SCHEDULE

16. DISTRIBUTION STATEMENT (of this Report)

Approved for public release; distribution unlimited.

(19) AD-E430 142

DDC RECEIVED DEC 19 1978 B

17. DISTRIBUTION STATEMENT (of the abstract entered in Block 20, if different from Report)

18. SUPPLEMENTARY NOTES

19. KEY WORDS (Continue on reverse side if necessary and identify by block number)

shaped-charge jets	framing camera observations
propellant reactions	ranking of violence
M-30 propellant	deposited kinetic-energy
violent reactions	threshold energy values
hypervelocity particles	

20. ABSTRACT (Continue on reverse side if necessary and identify by block number) (hmn)

This investigation assesses both the violence of shaped-charge jet/propellant reactions and the pertinent jet-characteristics associated with this violence. The tests involved impacting 105 mm rounds which were instrumented with crush-gages and velocity screens. This instrumentation was augmented by framing camera observations (4 μs between frames) taken during two of the tests. The violence of each test was ranked by crush-gage pressures and cartridge-case damage. The test results show that there are three types of violence associated with shaped- (over)

DD FORM 1 JAN 73 1473 / EDITION OF 1 NOV 65 IS OBSOLETE

UNCLASSIFIED

SECURITY CLASSIFICATION OF THIS PAGE (When Data Entered)

microseconds

393 471

charge jet/propellant reactions: These types were labeled as: (1) non-violent, ~~type which is~~ similar to hydrostatically rupturing the case due to a localized pressure; (2) moderately-violent type whose violence is similar to an electrically ignited round; and (3) severely-violent type whose violence is similar to a deflagration of high explosive. The deposited kinetic-energy was found to yield the best *a priori* prediction for both the type of reaction and the ranking within each type. It was hypothesized that the reaction can be characterized via two threshold-energy values E_I and E_{II}, and two threshold-widths ΔE_I and ΔE_{II}. Tests employing hypervelocity particles confirmed the threshold-energy hypothesis, with E_I = 10 kJ and E_{II} = 50 kJ for the 105-mm round. However, the hypervelocity particle and shaped charge jet data show that good *a priori* predictions can be made only if multiple off-axis impacts are accounted for.

E sub 1 = approximately 10 KJ and
E sub 2 = approximately 50 KJ

E sub 1 and E sub 2,

Delta E sub 1 and Delta E sub 2.

TABLE OF CONTENTS

		Page
	LIST OF ILLUSTRATIONS	5
I.	INTRODUCTION	7
II.	EXPERIMENTAL PROCEDURES AND RESULTS	8
	A. Instrumented 105mm Heat Rounds	8
	B. Framing Camera Observations	24
III.	DISCUSSION	37
	A. Interpretation of Experimental Results	37
	B. Kinetic Energy Hypothesis	43
	C. Verification of Hypothesis Using Hypervelocity Particles	48
IV.	SUMMARY	55
	ACKNOWLEDGEMENTS	59
	APPENDIX A. Set of Framing-Camera Photographs Obtained During Test 7	61
	APPENDIX B. Experimental Procedure for Using Hypervelocity Particles	99
	APPENDIX C. Ionization-Probe Test	109
	DISTRIBUTION LIST	113

[redacted]

ACCESSION for
NTIS White Section
DDC Buff Section
UNANNOUNCED
JUSTIFICATION
BY
DISTRIBUTION/AVAILABILITY CODES
Dist. AVAIL. and/or SPECIAL
A

LIST OF ILLUSTRATIONS

Figure		Page
1	Schematic Diagram of Basic Arrangement of Test.	9
2	Photographs of Actual Arrangement Prior to a Test	10
3	Schematic Diagram Illustrating the Definition of $< P >_{105}$	13
4	Results of Tests 1 through 3.	15
5-11	Results of Individual Tests 4 through 10.	16-22
12	Schematic Diagram of Test Arrangement Used for Framing Camera Observations	25
13	Photograph of Spall Debris and 105 mm Round at a Time of 0.5 μs Prior to Impact for Test 6	26
14	Photograph taken 52.5 μs after Impact for Test 6.	27
15	Photograph showing Jet Debris Striking Top of Witness for Test 6.	28
16	Photograph Taken 4.0 μs Prior to Impact for Test 7. . . .	30
17	Photograph Taken at Time of Impact for Test 7	32
18	Photograph Taken 48.0 μs after Impact for Test 7.	33
19	Photograph Taken 52.0 μs after Impact for Test 7.	34
20	Photograph Taken 88.0 μs after Impact for Test 7.	35
21	Photograph Taken 112 μs after Impact for Test 7	36
22	Schematic Diagram of the Three Regions of Violence with Respect to Pressure Magnitudes and Deposited Kinetic-Energy.	44
23	A Plot of the Deposited Kinetic Energy and Average Crush-Gage Pressure-Readings Associated with Tests Number 1 through 10	45
24	Holes Induced in 9.7 mm Thickness of RHA by Jets Associated with Tests 1 through 3	47
25	Radiographs Taken of a Shaped-Charge Jet after Passing Through M30 Propellant Beds of Various Sizes	49

PRECEDING PAGE BLANK-NOT FILMED

LIST OF ILLUSTRATIONS

Figure		Page
26	Schematic Diagram Showing Influence of Jet Curvature Upon the Jet Length ΔL and Exit Velocity V_e	50
27	Schematic Diagram Showing Influence of Particle Yaw Upon Number of Particles Consumed	51
28	Cartridge-Case Remnants Associated with Tests No. 11 through 13	56
29	Correlation Between Deposited Kinetic-Energy and Average Crush-Gage Pressures for Both Shaped-Charge Jets and Hypervelocity Particles	57
A.1-A.35	Sequential Photographs Taken During Test 7	63-97
B.1	Schematic Diagram of Arrangement Used for Obtaining a Hypervelocity "Rod"	101
B.2	Radiograph of a Free Flight Jet Without an Inhibitor	102
B.3	Radiograph of an Inhibited Jet After Passing Through the Material Shown in Figure C.1	103
B.4	Photograph of Steel Witness-Plates Associated With the Jet Shown in Figure B.3	104
B.5	Photograph of Overall Arrangement for Test No. 11	105
B.6	Schematic Diagram of Air-Cavity Charges Used for Producing Hypervelocity Disks	106
B.7	Radiograph Taken of a Free Flight Hypervelocity Disk Associated With an Air-Cavity Depth of 7.62 mm	107
B.8	Photographs of Overall Arrangement for Tests No. 12 and 13	108
C.1	Schematic Diagram of Arrangement Used for Ionization-Probe Test	111

I. INTRODUCTION

In order to design ammunition compartments properly, the reaction of the ammunition to an impact by a shaped charge jet must be known. Earlier tests[1-6] showed that, depending upon the hit location and the stimulant, the ammunition's reaction ranges from a slow burn of the propellant to a detonation. These results indicate that the violence of the ammunition's reaction can be controlled by limiting the conditions of the impacting jet. This implies that the armor design does not have to completely stop a shaped-charge jet, but rather condition the jet so that it does not induce a violent reaction.

The purpose of this investigation is to quantitatively assess the pertinent jet-characteristics associated with the violence of a propellant reaction[7]. The approach taken was to impact instrumented (crush gages and velocity screens) 105 mm rounds with shaped-charge jets of various diameters, velocities, axial alignment and penetration capability. This was augmented by taking high-speed framing-camera observations (4 μs between frames) during two of the instrumented tests. The violence of each event was ranked by the crush-gage pressures and deformation of the cartridge case. The jet parameters required for a violent reaction were studied by comparing the ranked violence with various jet-parameters, such as penetration capability, tip velocity, jet diameter, impulse (momentum) delivered to the round, and the kinetic energy deposited in the round.

---

1. J.N. Majerus, DF entitled, "Test Matrix For Propellant Initiation via Shaped Charges, the Required Instrumentation, and other Associated Tests Concerned with Ammo Compartments," dated 9 May 1974.
2. G. Melani, R.B. Frey and S. Margene Carter, "Determination of the Residual Jet Parameters Required to Initiate Cased Explosive Charges," Ballistic Research Laboratory Memo. Report No. 2753, May 1977.
3. R. Frey, G. Melani, J. Waddell, B. Taylor, and C. Ruth, "Pressure Measurements in Highly Confined M456 Cartridge Cases After Primer and Cookoff Ignition," Ballistic Research Laboratory Memo Report No. 2764, June 1977. (AD #B020522L)
4. R. Frey, R. Prenatt, G. Melani, B. Taylor and V. Boyle, "Explosive Reactions in Propellant Beds," Ballistic Research Laboratory Interim Memo Report No. 568, August 1977. (not available)
5. D.F. Menne, and F.T. Brown, "Sensitivity of 105 mm M456A1 Ammunition to Attack by Shaped Charges," Ballistic Research Laboratory Memo Report No. 2543, October 1975. (AD #B008041L)
6. D.F. Menne and F.T. Brown, "Vented Ammunition Compartment Tests With Live 105 mm Ammunition, " Ballistic Research Laboratory Memo Report No. 2564, December 1975. (AD #B008755L)
7. J.N. Majerus and A.B. Merendino, "Shaped Charged Jet/Propellant Interactions," Proceedings of the 2nd Symposium on Vulnerability and Survivability," Vol II, pp 63-80, January 1977.

II. EXPERIMENTAL PROCEDURES AND RESULTS

The main investigation involved impacting various jets upon instrumented 105 mm rounds. This procedure and its results are discussed first. The framing camera observations are then discussed in a subsequent section.

A. Instrumented 105 mm HEAT Rounds

The test site was a three sided earth-barricade with a steel roof. Sheets of plywood were placed across the entrance in an attempt to confine the unburnt propellant within the barricade. After each test a search was made of both the barricade and the entrance area for pieces of unburnt propellant. These pieces were collected and weighed so that an estimate could be made of the consumed (burned and powdered) propellant.

The basic arrangement used in the tests is shown schematically in Figure 1. The shot line of the attacking warhead was always located at a distance of 216 mm from the base and 19 mm off the axial center line of the round. This shot line was chosen because it missed the internal primer section, and was the shot-line used in the earlier compartmentalization tests[5]. Figure 2 shows photographs of an actual set-up prior to a test.

Several (2-4) crush gages were located near the nose of the round (at the finned section of the projectile) and four additional gages were positioned at the base of the round. In the first three tests two aluminum and two copper gages were located at the base position. The aluminum gage is limited to a pressure of approximately 53 M Pa (7700 psi) and is calibrated with respect to lower pressures. The copper gage is limited to a pressure of approximately 131 M Pa (19,000 psi) and is not as sensitive to pressure as the aluminum gage. The indicated pressures of the first three tests were quite high and the gages were damaged by impacting various elements around the test site. Consequently, the remaining tests employed two iron and two copper gages at the base, and two copper and two aluminum gages at the nose. The iron gages are calibrated for a pressure range of 86.4 to 345 M Pa (12.5 to 50 thousand psi), and provided a check on the copper gage readings. It should be noted that the crush gage readings have been found to be fairly indicative of the actual pressure[3] of the environment.

The velocity screens (see Figures 1 and 2) were used for several purposes. First, the time elapsed between the jet's striking screen #1 ($t \equiv 0$), and the breaking of screen #2, is a measure[2] of the type of propellant reaction, i.e., times on the order of 50 μs would be indicative of a propagating detonation wave. Secondly, the time elapsed between the breaking of screens #2 and #3 allows one to

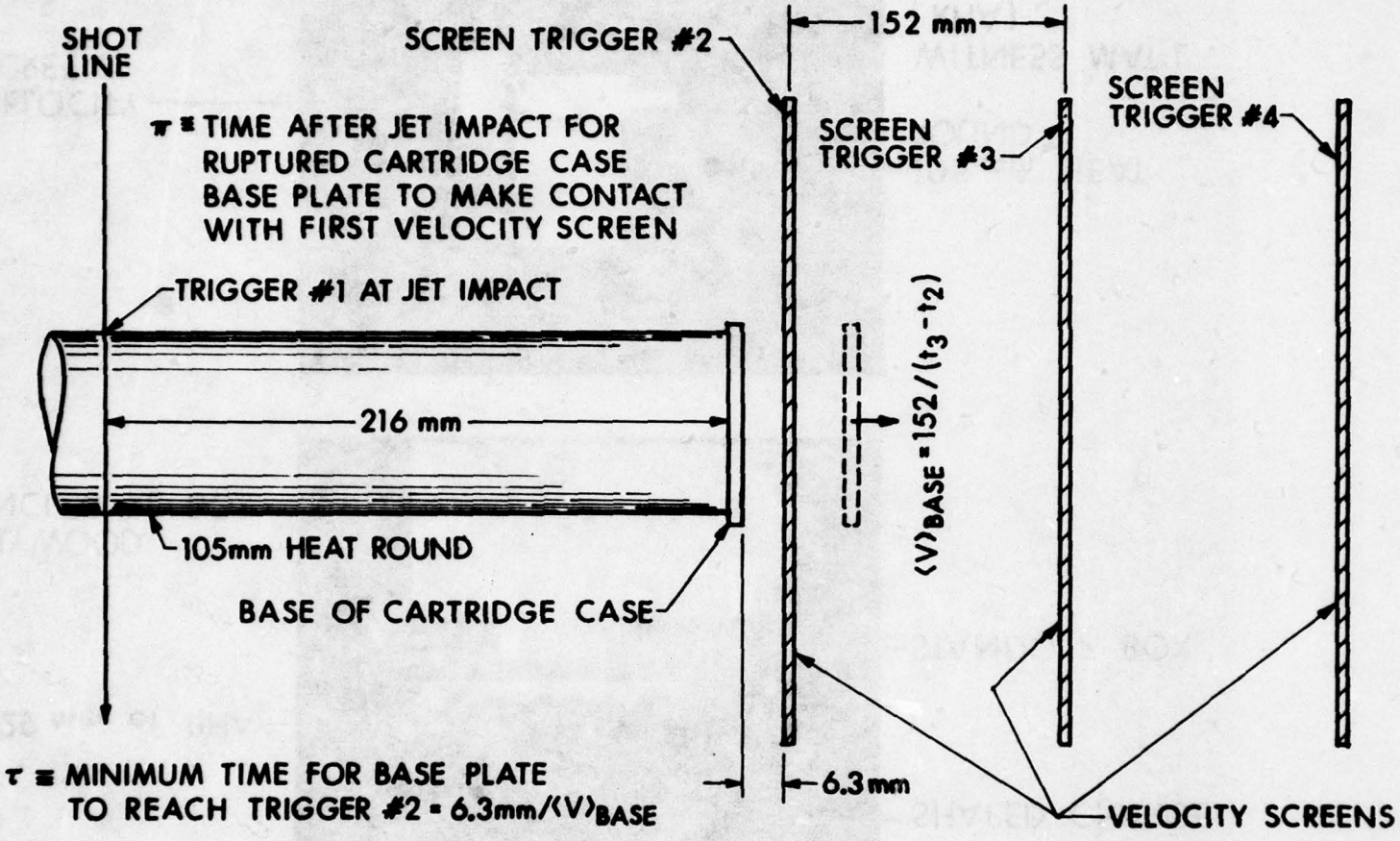

Figure 1. Schematic Diagram of Basic Arrangement of Test

AD-A124 041 11 82

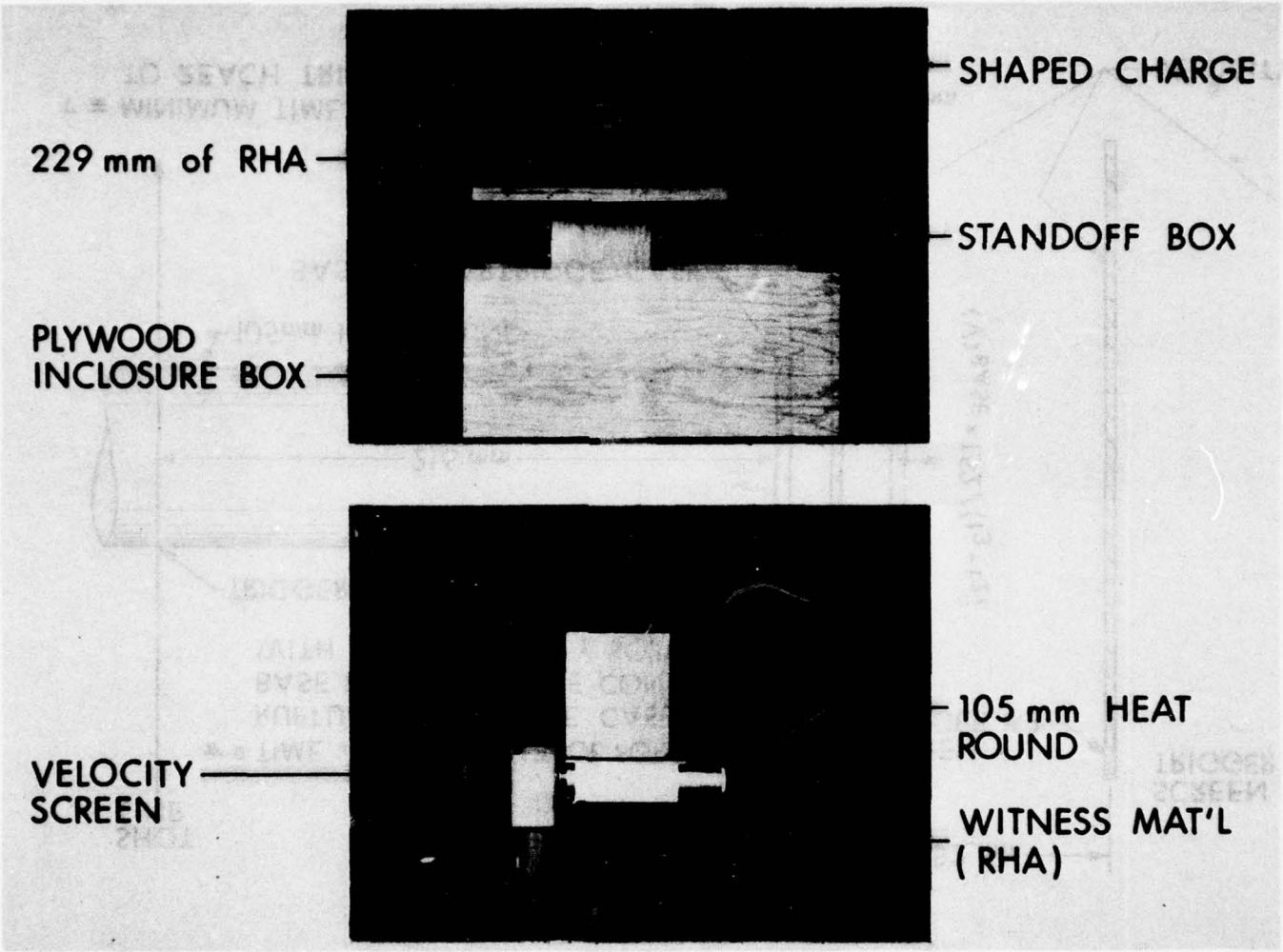

Figure 2. Photographs of Actual Arrangement Prior to a Test

calculate the velocity of the base of the cartridge case. In general, this base velocity should increase with increasing violence of the event.

Initially, only three velocity screens were employed. In order to be sure of obtaining a velocity reading of the base another velocity screen (screen #4) was added and the majority of the tests used four velocity screens. Unfortunately, the triggering of the last three screens was erratic and the readings are dubious. Therefore, the calculated velocities are shown listed with a question mark.

The shaped charge conditions are listed in Table I. The first seven tests were concerned with medium caliber warheads attacking a simulated ammunition compartment. The 81 mm round is representative of a post-1980 shoulder-fired HEAT projectile. The 86 mm round can be considered as a threat associated with a penetrator forming type of a land mine. The last three tests were concerned with an ammunition attack by automatic cannon rounds with a shaped-charge warhead[8]. It should be noted that tests Nos. 6 and 7 were used for the framing camera observation and did not utilize any velocity screens. The target in all tests was a complete 105 mm HEAT round with an inert warhead.

The simulated compartment walls mentioned in Table I refer to two plates used to represent a compartment wall and a storage tube around the ammunition (see Figure 3). In some tests, materials were placed along the jet's path in order to reduce the jet's tip velocity. The striking velocity (when less than the free-flight tip value) listed in Table I was calculated using a modified version[9] of the DiPersio, Simon and Merendino equations[10]. These equations have been shown[9,11] to yield jet striking velocities close to experimental values.

Also shown in Figure 3 is an illustration of the meaning of the term $< p >_{105}$. The value of $< p >_{105}$ refers to the average penetration capability of the shaped-charge into a rolled homogeneous armor (RHA) target placed at the location of the 105mm round. Another penetration value used is the witness penetration. This refers to the

8. R. DiPersio, W.H. Jones, A.B. Merendino and J. Simon, "Characteristics of Jets From Small Caliber Shaped Charges With Copper and Aluminum Liners," Ballistic Research Laboratories, Memorandum Report No. 1866, September 1967. (AD #823839)
9. A. Merendino, H. Jonas, and W. Jones, "The Effects of Spaced Steel Plates on Shaped Charge Jets," Ballistic Research Laboratory Report No. 1573 (Classified), March 1972. (AD #521023L)
10. R. DiPersio, J. Simon and A.B. Merendino, "Penetration of Shaped Charge Jets into Metallic Targets," Ballistic Research Laboratories Report No. 1296, September 1965. (AD #476717)
11. J.N. Majerus, "A Model for Studying the Influence of Guidance Packages Upon Shaped Charge Warhead Performance," Ballistic Research Laboratory Report No. 1942, November 1976. (AD #B015399L)

TABLE I

TEST CONDITIONS AND SHAPED CHARGE JET CHARACTERISTICS

Test Number	Type of Warhead	Total Standoff Distance to Tgt. mm (cone diameter)	Simulated Compartment Walls	Jet Velocity Striking Tgt. mm/μs	Free Flight Jet Tip Velocity V_{jo} mm/μs	Jet Break-up Time μs	Avg. Jet Diameter mm	Avg. Particle Length mm
1	81mm,Cu 42°	756 (9.4CD)	Yes	3.5	7.6	122	2.9	13.7
2	81mm,Cu 42°	756 (9.4CD)	Yes	6.5	7.6	122	2.9	13.7
3*	81mm,Cu 42°	756 (9.4CD)	Yes	6.5	7.6	122	2.9	13.7
4	86mm,Cu Hemi	1577 (18.3CD)	Yes	3.6	3.7	221	6.3	20.5
5	86mm,Cu Hemi	515 (6CD)	Yes	2.5	3.7	221	6.3	20.5
6	86mm,Cu Hemi	515 (6CD)	Yes	3.4	3.7	221	6.3	20.5
7	86mm,Cu Hemi	515 (6CD)	No	3.7	3.7	221	6.3	20.5
8+	19mm,Cu 20°	19 (1CD)	No	8.9	8.9	12.7	0.5	1.5
9+	2 @ 19mm,Cu 20°	19 (1CD)	No	8.9	8.9	12.7	0.5	1.5
10+	19mm, Cu Cap	133 (7CD)	No	3.7	3.7	43.1	1.5	4.9

* This jet was made to have numerous particles traveling off the axis of charge symmetry.

\+ These jet characteristics were taken from Reference 8.

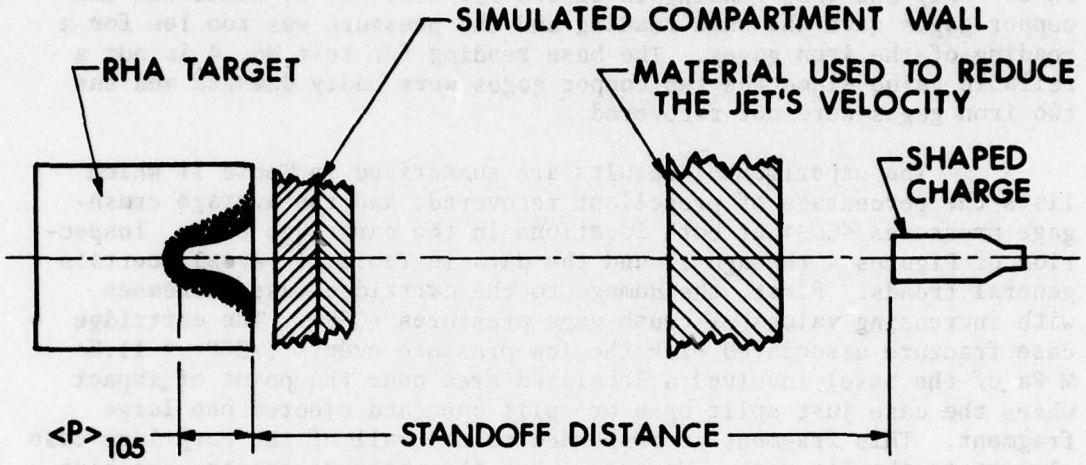

Figure 3. Schematic Diagram Illustrating the Definition of $< P >_{105}$

measured penetration of the jet into a steel witness located below the 105 mm round, i.e., after the jet has passed through the round.

The results of the first three tests are shown in Figure 4 and the remaining seven test results are shown in Figure 5 through 11 respectively. Each figure shows the remnants of the 105 mm cartridge case which were recovered after each test. The crush-gage pressure readings shown in each figure refer to the lowest and highest values recorded at each location i.e., the base and nose of the cartridge case. Only one base reading is listed for test No. 8, since the two copper gages gave the same reading and the pressure was too low for a reading of the iron gages. The base reading for test No. 4 is not a reliable value since the two copper gages were badly damaged and the two iron gages were not recovered.

The experimental results are summarized in Table II which lists the percentage of propellant recovered, and the average crush-gage pressures <CGP> at both locations in the cartridge case. Inspection of Figures 4 through 11 and the data in Table II reveal certain general trends. First, the damage to the cartridge case increases with increasing values of crush-gage pressures <CGP>. The cartridge case fracture associated with the low pressure events (<CGP> $\leq$ 11.7 M Pa of the base) involved a localized area near the point of impact where the case just split open or split open and ejected one large fragment. This fragment corresponded to the wall of the cartridge case closest to the jet path. However, when the pressure events were high (<CGP> $\geq$ 40 M Pa at the base), the cartridge case fragmented into many pieces. In many cases the cartridge case damage[3] was more severe than that observed for either electrical ignition[12] or cook-off of the 105 mm round. It also appears that for these high pressure events, the higher the value of <CGP>, the smaller the fragment size. In the most violent events, the cartridge case is completely stripped off of the base plate.

The second observation is concerned with the pressure magnitudes. The nose and base pressure readings appear to correlate in that the nose pressure increases when the base pressure increases. For the low pressure events (<CGP> < 11.7 M Pa at the base), the nose and base pressures are about the same. However, the nose and base pressure are different for the high pressure events (<CGP> $\geq$ 40 M Pa at the base). This is analogous to what was observed[3,12] for electrical ignition and cook-off , except that the ratio between the base and nose pressures is different. The ratios obtained from Table II range from 2.4 to 4.5 (the value of 5.0 for test No. 4 is questionable), with four of the ratios being 2.4, 2.5, 2.6 and 2.9. The ratio associated

12. C.R. Ruth and J.M. Frankle, "Rupture Pressures for Metal Cartridge Cases," Ballistic Research Laboratories, IMR NO. 236, June 1974. (not available)

JET CONDITIONS: V_s = 3.8 mm/μsec, SOME OFF-AXIS JET PARTICLES, $\langle P \rangle_{105}$ = 100 mm

MEASURED EVENTS: $\langle V_{BASE} \rangle$ = 34.1 m/s, τ_1 = 373 μsec, τ_2 = 185 μsec

CRUSH GAGE PRESSURE READINGS: Nose = 15.2, 16.6 MPa (2.2, 2.4 × 10^3 psi); Base = 38.6, 40.0 MPa (5.6, 5.8 × 10^3 psi)

JET CONDITIONS: V_s = 6.5 mm/μsec, AXIALLY ALIGNED JET, $\langle P \rangle_{105}$ = 300 mm

MEASURED EVENTS: $\langle V_{BASE} \rangle$ = NO COUNT, τ_1 = 291 μsec, τ_2 = NO COUNT

CRUSH GAGE PRESSURE READINGS: Nose = 22.1, 24.1 MPa (3.2, 3.5 × 10^3 psi); Base = 66.8 MPa (9.7 × 10^3 psi)

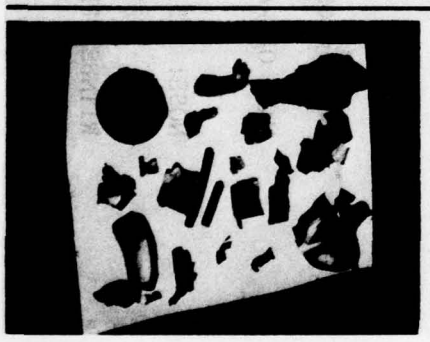

JET CONDITIONS: V_s = 6.5 mm/μsec, NON-ALIGNED JET, $\langle P \rangle_{105}$ = 100 mm

MEASURED EVENTS: $\langle V_{BASE} \rangle$ = 80.2 m/s, τ_1 = 296 μsec, τ_2 = 80 μsec

CRUSH GAGE PRESSURE READINGS: Nose = 36.6, 40.0 MPa (5.3, 5.8 × 10^3 psi); Base = 91.7, 107 MPa (13.3, 15.5 × 10^3 psi)

Figure 4. Results of Tests 1 through 3

TEST NUMBER 4

SHAPED CHARGE: 86.5 MM CU HEMI, COM B

$<_{105}>$ =1.75 MM, V_S = 3.6 Km/s

τ_{12} = NA

$<V_{12}>$ = 650 M/S $<V_{23}>$ = 190 M/S

Readings are questionable.

MASS OF RESIDUAL PROPELLANT = 855 GRAMS

CRUSH GAGE PRESSURES

NOSE: 15.9 - 35.2 MPa (2300 - 5100 PSI)

BASE: 133 (?) (GAGES DAMAGED) MPa

WITNESS PENETRATION: 41 MM

Figure 5. Results of Individual Tests 4.

TEST NUMBER 5

SHAPED CHARGE: 86.5 MM CU HEMI, COMP B

$\langle P_{105} \rangle$ = 100 MM, V_S = 2.5 MM/μS

τ_{12} = 315 μS

$\langle V_{12} \rangle$ = NA M/S, $\langle V_{23} \rangle$ = NA M/S

MASS OF RESIDUAL PROPELLANT = 499 GRAMS

CRUSH GAGE PRESSURES

NOSE: 9.3 - 19.3 MPa (1350 - 2800 PSI)

BASE: 41.3 - 44.7 MPa (6000 - 6500 PSI)

WITNESS PENETRATION: 35 MM

Figure 6. Results of Individual Test 5

TEST NUMBER 6

SHAPED CHARGE: 86.5 MM, CU HEMI, COMP B

$\langle P_{105} \rangle$ = 175 MM, V_{JO} = 3.4 MM/μS

CRUSH GAGE PRESSURES:

NOSE: 18.0 - 36.6 MPa (2600 - 5300 PSI)

BASE: 82.7 - 12.8 MPa (12000 - 18600 PSI)

WITNESS PENETRATION: 150 + MM
(Penetration exceeded thickness at witness)

Figure 7. Results of Individual Test 6

TEST NUMBER 7

SHAPED CHARGE: 86.5 MM, CU HEMI, COMP B

$\langle P_{105} \rangle$ = 200 MM, V_{JO} = 3.7 MM/μS

CRUSH GAGE PRESSURES

NOSE: 26.2 - 45.0 MPa (3,800 - 6,530 PSI)

BASE: 103 - 131 MPa (14,900 - 19,000 PSI)

WITNESS PENETRATION: 125

Figure 8. Results of Individual Test 7

TEST NUMBER 8

SHAPED CHARGE: 19 MM 20° CU

$< P >_{105}$ = 75 MM, V_S = 8.9 MM/μS

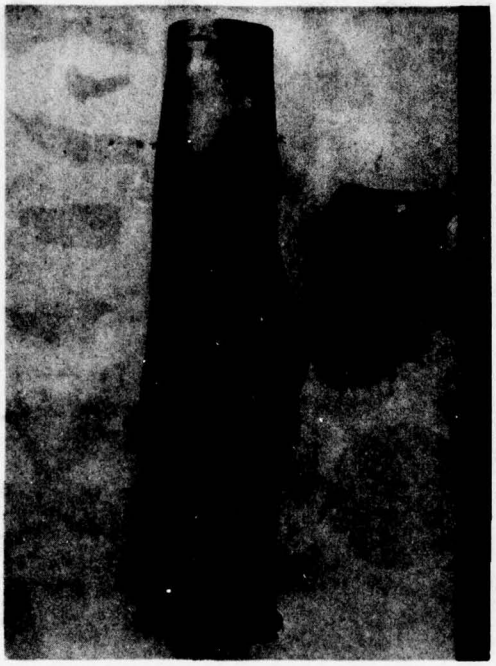

τ_{12} = NA

$< V_{12} >$ = 450 M/S $< V_{23} >$ = 445 M/S **Readings are questionable.**

MASS OF RESIDUAL PROPELLANT = 2278 GRAMS

CRUSH GAGE PRESSURES

NOSE: 3.0 - 14.5 MPa (440 - 2100 PSI)

BASE: 6.2 - 7.6 MPa (900 - 1100 PSI)

WITNESS PENETRATION: 1.6 MM

Figure 9. Results of Individual Test 8

TEST NUMBER 9

SHAPED CHARGE: 2@ 19 MM, 20° CU, 73 MM
BETWEEN CENTER LINES

$\langle P \rangle_{105}$ = 75 MM, V_S = 8.9 MM/μS

τ_{12} = 320 μS

$\langle V_{12} \rangle$ = 696 M/S $\langle V_{23} \rangle$ = 498 M/S
Readings are questionable.

MASS OF RESIDUAL PROPELLANT = 3635 GRAMS

CRUSH GAGE PRESSURES:

NOSE: 3.8 - 12.4 MPa (550 - 1800 PSI)

BASE: 11.7 MPa (1700 PSI)

WITNESS PENETRATION: 0.8 MM

Figure 10. Results of Individual Test 9

TEST NUMBER 10

SHAPED CHARGE: 18MM, CU CAP, COMP B

$\langle P \rangle_{105}$ = 50, V_S = 3.7/μS

τ_{12} = NA

$\langle V_{12} \rangle$ = NA, $\langle V_{23} \rangle$ = NA

MASS OF RESIDUAL PROPELLANT = 3599 GRAMS

CRUSH GAGE PRESSURES

NOSE: 2.3 - 4.8 MPa (330 - 700 PSI)

BASE: 2.1 - 4.8 MPa (300 - 700 PSI)

WITNESS PENETRATION: 0.8 MM

Figure 11. Results of Individual Test 10

TABLE II

RECOVERED PROPELLANT AND AVERAGE CRUSH GAGE PRESSURES ASSOCIATED WITH EACH TEST

Test Number	Percentage of Propellant Recovered after Impact (100*Recovered Mass/5.35kg)	Average Crush <CGP> Gage Pressure			
		Base		Nose	
		MPa	psi	MPa	psi
1	20.5	39.3	(5,700)	15.8	(2,300)
2	21.6	56.5	(8,200)	23.4	(3,400)
3	9.3	99.9	(14,400)	38.6	(5,600)
4	16.0	133?	Gages Damaged	26.9	(3,900)
5	9.2	43.5	(6,300)	15.2	(2,200)
6	Not Recovered	114	(16,600)	25.5	(3,700)
7	Not Recovered	119	(17,200)	35.2	(5,100)
8	42.5	6.9	(1,000)	7.6	(1,100)
9	68.0	11.7	(1,700)	7.6	(1,100)
10	67.2	3.4	(500)	3.4	(500)

electrical ignition and cook-off ranges from 1.8 to 2.1.

Another observation deals with the amount of recovered propellant and the average crush-gage pressures. Neither the high pressure (Tests No. 1 through 7), nor the low pressure (Tests No. 8 through 10) events exhibit an increase in pressure with decreasing recovered-propellant. Due to the difficulty of recovering the propellant even under ideal circumstances[13], this lack of correlation may be due to the inaccuracy of propellant recovery. However, there appears to be a definite demarcation between the high and low pressure events; about 50% of the propellant was recovered for all the low pressure events whereas less than 25% of the propellant was recovered for all the high pressure events.

B. Framing Camera Observations.

Tests No. 6 and 7 involved a direct observation of an impacted 105 mm round. This observation used a model 192 Beckman and Whitley framing-camera, which provides eighty frames and a maximum framing-rate of 1,440,000 frames per second. The only difference between tests No. 6 and 7 was the presence of a simulated compartment wall in test No. 6. A schematic diagram of the overall test set-up is shown in Figure 12.

A fixed reference-grid (25.4 x 25.4 mm) was superimposed upon the film by statically exposing the film to a back-lit precision grid which was located at the same distance from the camera as the jet impact.

Due to a malfunction in the timing mechanism the external light-source was on during only a small portion (16 frames) of the impact event in test No. 6. However, sufficient light was generated by the propellant reaction so that a faint image was evident for about 55 frames (separated by 4 μs for a total time of 220 μs) after jet impact. Figure 13 shows the spall-debris and the 105 mm round at a time of 0.5 μs after impact. Radiographs taken after a jet has exited a plate show that the jet tip is at the foremost edge of the debris along the jet's path. Therefore, using the debris cloud as a function of time gives the speed of the jet.

The gray line near the bottom of the round shown in Figure 14 corresponds to the luminosity induced by the jet as it exits from the cartridge case. The photograph in Figure 15 shows the jet debris striking the top of the witness material, that is, the dark horizontal line near the bottom of the photograph which corresponds to impact-induced luminosity. Based upon the distance from the exit location

13. J.D. Knapton, I.C. Stobie, R.H. Comer, L. Stansbury, and R.L. Mortz, "Vigorous Ignition of M30 Propellant," Ballistic Research Laboratory, IMR No. 397, June 1975. (not available)

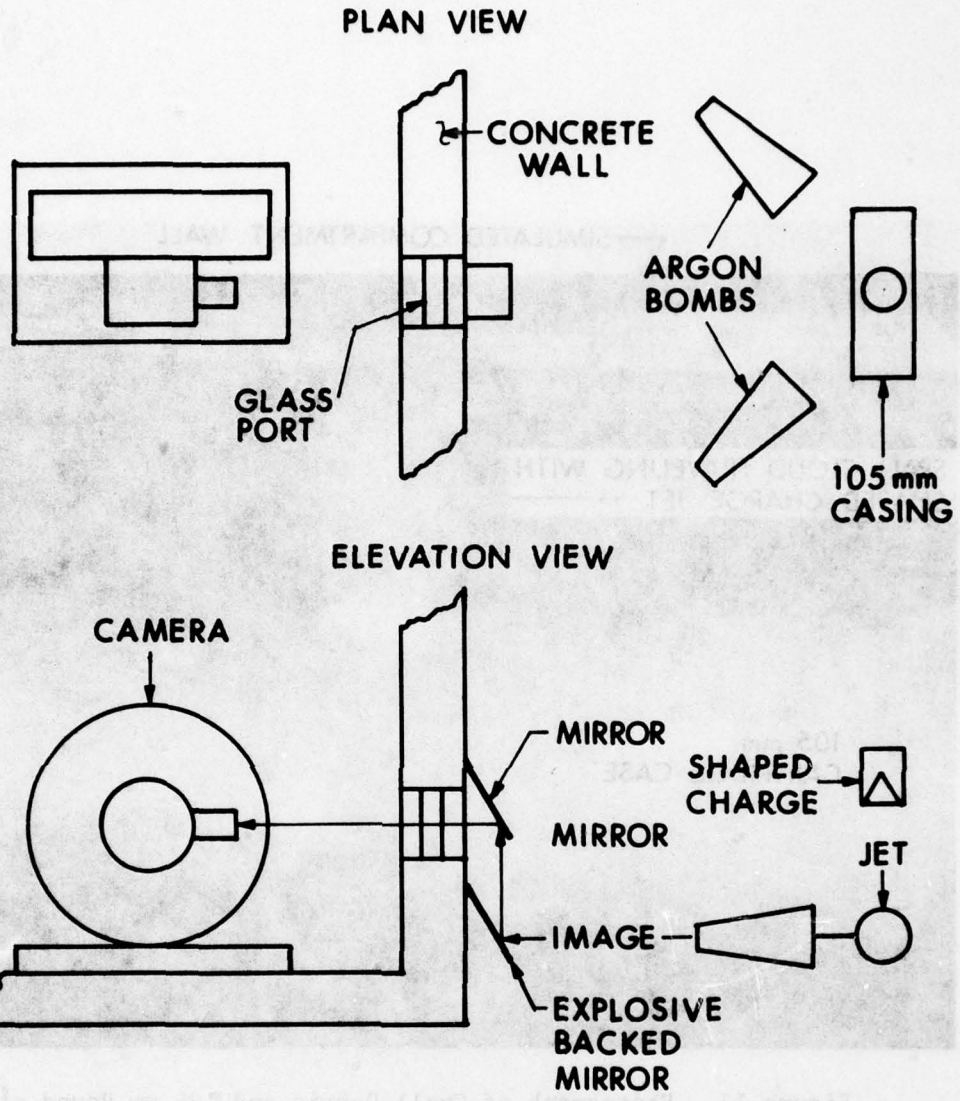

Figure 12. Schematic Diagram of Test Arrangement Used for Framing Camera Observations

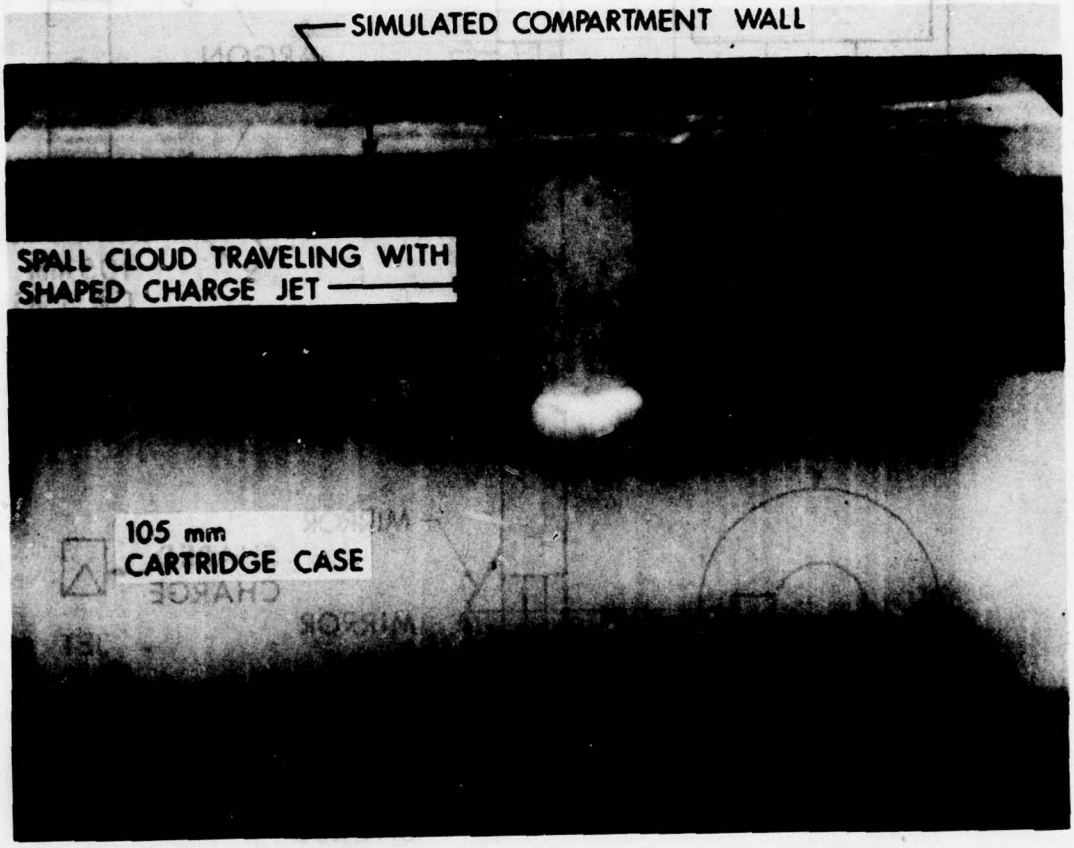

Figure 13. Photograph of Spall Debris and 105 mm Round at a Time of 0.5 μs Prior to Impact for Test 6

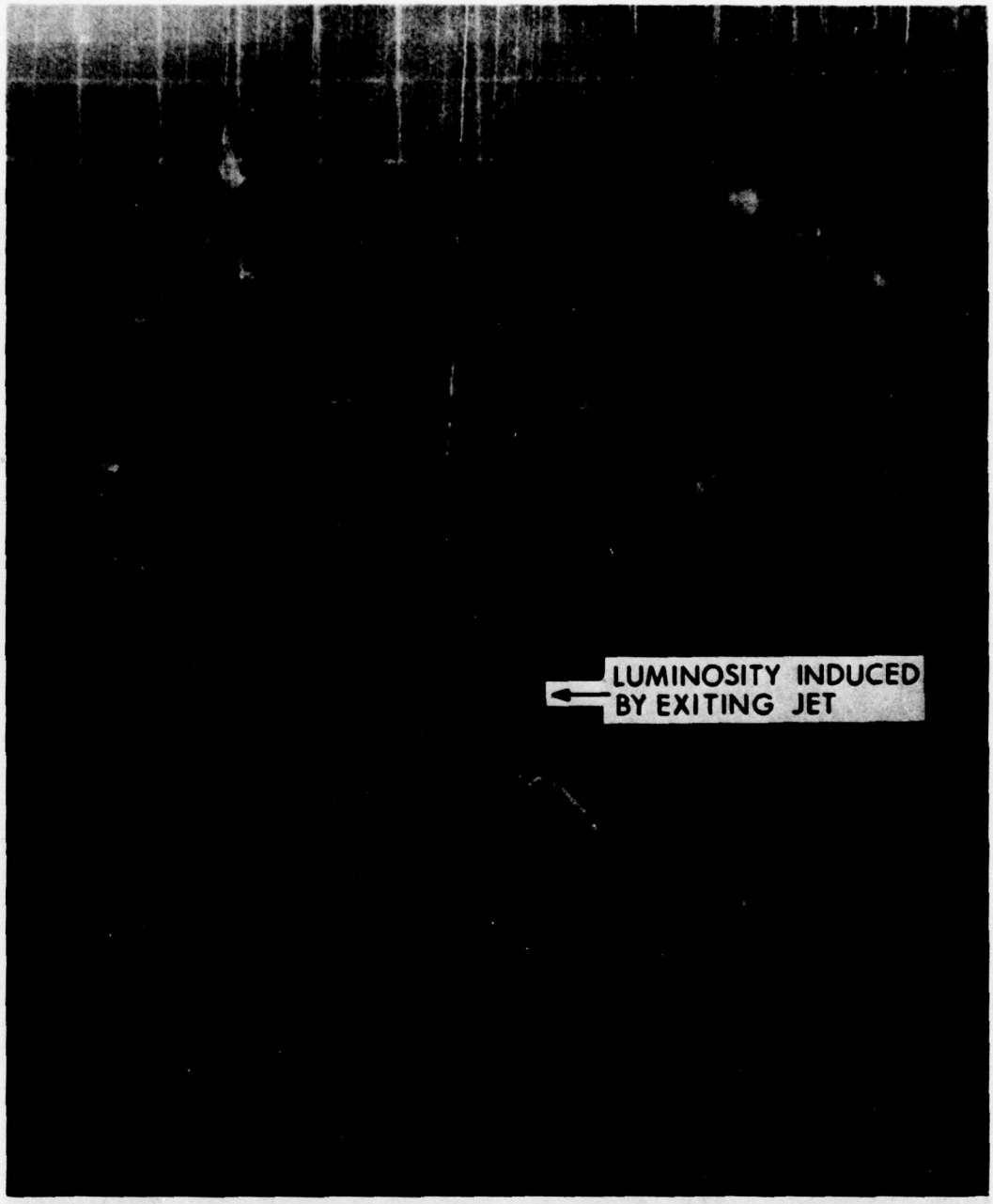

Figure 14. Photograph taken 52.5 μs after Impact for Test 6

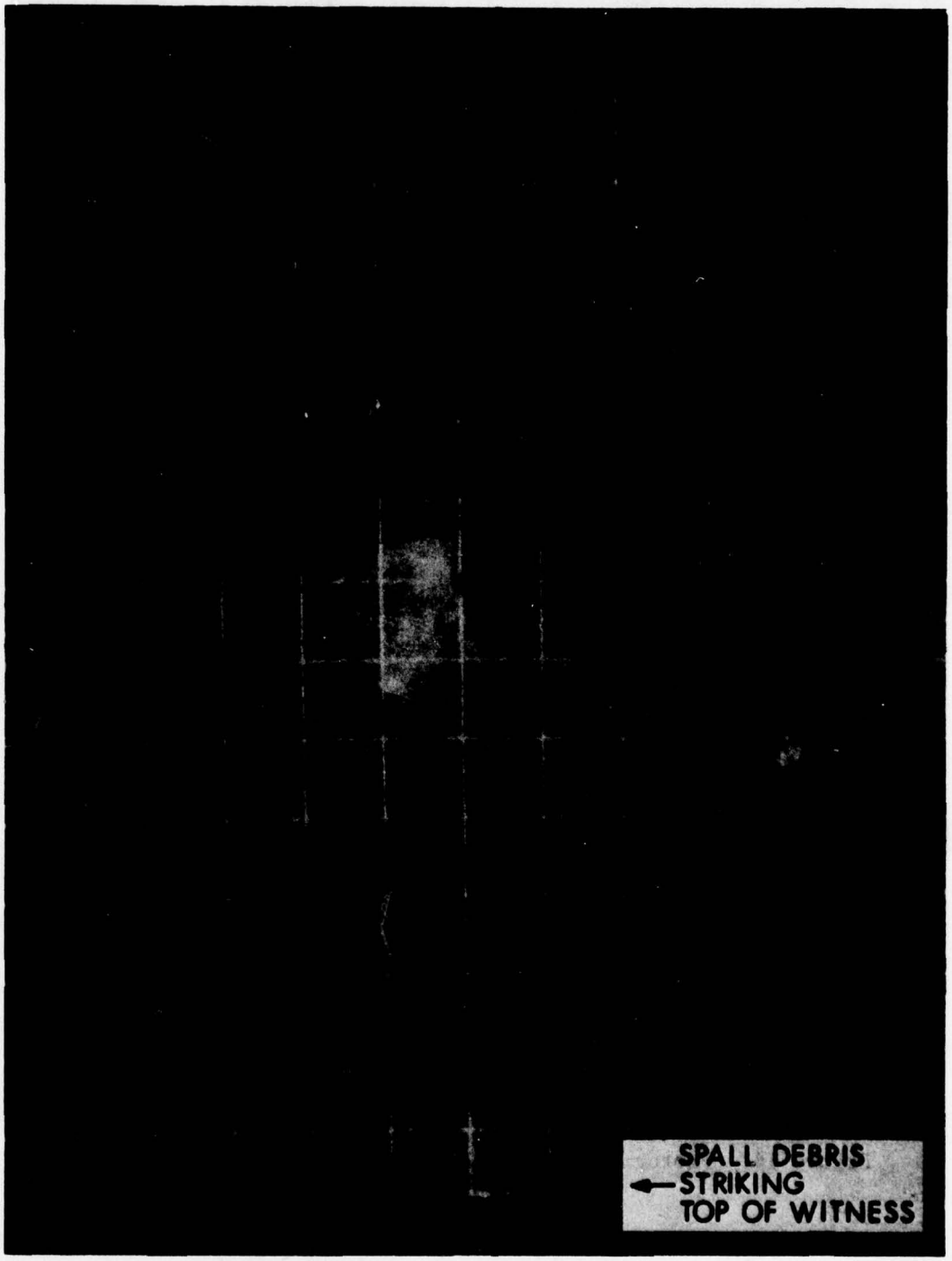

Figure 15. Photograph showing Jet Debris Striking Top of Witness for Test 6

to the top of the witness, and the lapsed time (40 μs) between the events, the average speed shown in Table III is obtained. Table III also lists other speeds measured in tests No. 6 and 7, and contains some theoretical values based upon incompressible theory*.

One other observation of test No. 6 involves the motion of the cartridge-case base plate. In the 39th frame taken after jet impact, a thin vertical-line corresponding to the base plate is still evident. The location of this line was measured with respect to a fixed vertical fiducial line. This measurement reveals that the base plate did not move during this time interval (156 μs).

Some of the photographic results obtained during test No. 7 are shown in Figures 16 through 21. A total of 67 frames were recorded after impact. The time between each frame is 4.0 μs and hence the cartridge case was observed for 268 μs after jet impact. The majority of the frame-by-frame observations are shown in Appendix A. Figure 16 shows the jet just prior to impact on the cartridge case. Note the rather massive jet-tip associated with this particular shaped-charge jet. Figure 17 shows the jet and cartridge case right at the time of impact. In Figure 18 the jet is beginning to exit the round at a time of 48 μs after impact. Multiple off-axis impacts on the bottom of the cartridge case are evident at a time of 52 μs after impact (see Figure 19). The top of the witness is struck by the jet at a time of 88 μs after impact (Figure 20). Figure 21 shows the remnants of the cartridge case at a time of 112 μs after impact.

The base plate of the cartridge case is clearly in view up to a time of 120 μs. Beyond this time the base plate is slowly obscured by the propellant gases. However, enough is visible to ascertain that the base plate had not moved during the 268 μs of observation. Note that the times recorded in tests No. 1-3 and 5, as the times required after impact for the base plate to perforate the second velocity-screen (see Figure 1), were 373, 291, 296 and 315 μs respectively. However, if a detonation occurs over the entire propellant bed, the disturbance should propagate at least on the order of a compressive wave[13] (≃ 3 km/s). Based on the impact location, no more than 70 μs would be required for a detonation wave to reach the base plate. Therefore, both the framing camera and velocity-screen observations indicate that a detonation did not occur over the entire length of the 105 mm round.

Table III contains the data associated with several other observations on test No. 7. First, case-fragments near the path of

*Penetration velocity is always decreased due to compressibility effects and hence the penetration time increases. Based upon the compressibility behavior of M-30 propellant as estimated by Dr. R. Frey of TBD, compressibility effects would account for about a five percent reduction in the average penetration velocity. The above framing-camera data indicates about a 10% reduction in the average penetration-velocity.

TABLE III

QUANTITIES MEASURED IN TESTS 6 AND 7, AND

COMPARISONS WITH SOME THEORETICAL* VALUES.

Average Speed of Jet Located Between the Simulated Compartment-Wall and the 105 mm Round		Measured: 3.44 + 0.07 - 0.12 km/s Predicted**: 3.57 km/s exiting wall 3.40 km/s striking 105 mm round	
		Test 6	Test 7
Time to Penetrate the 105 mm Round:	Measured	52.5 μs	48.0 μs
	Predicted	47.7 μs	44.1 μs
Average Speed of Jet Located Between 105 mm Round and the Witness:	Measured	2.5 km/s	2.81 ± 0.25 km/s
	Predicted	3.08 km/s	3.31 km/s
In-Plane Fragment Speeds (Test 7):	Small particles near impacted region ≃ 2 km/s Large fragment near bottom of cartridge case = 0.55 ± 0.2 km/s		
Average separation speed of two reflective areas in Test 7: 1.32 ± 0.2 km/s			
Axial cloud-speed near impact location in Test 7 ≃ 0.9 km/s			

* All predicted or theoretical values are based upon the imcompressible ideal-jet theory[9-11] and the measured striking-velocity of the shaped-charge jet.

**Velocity decreases due to the spaced-plate effect[9].

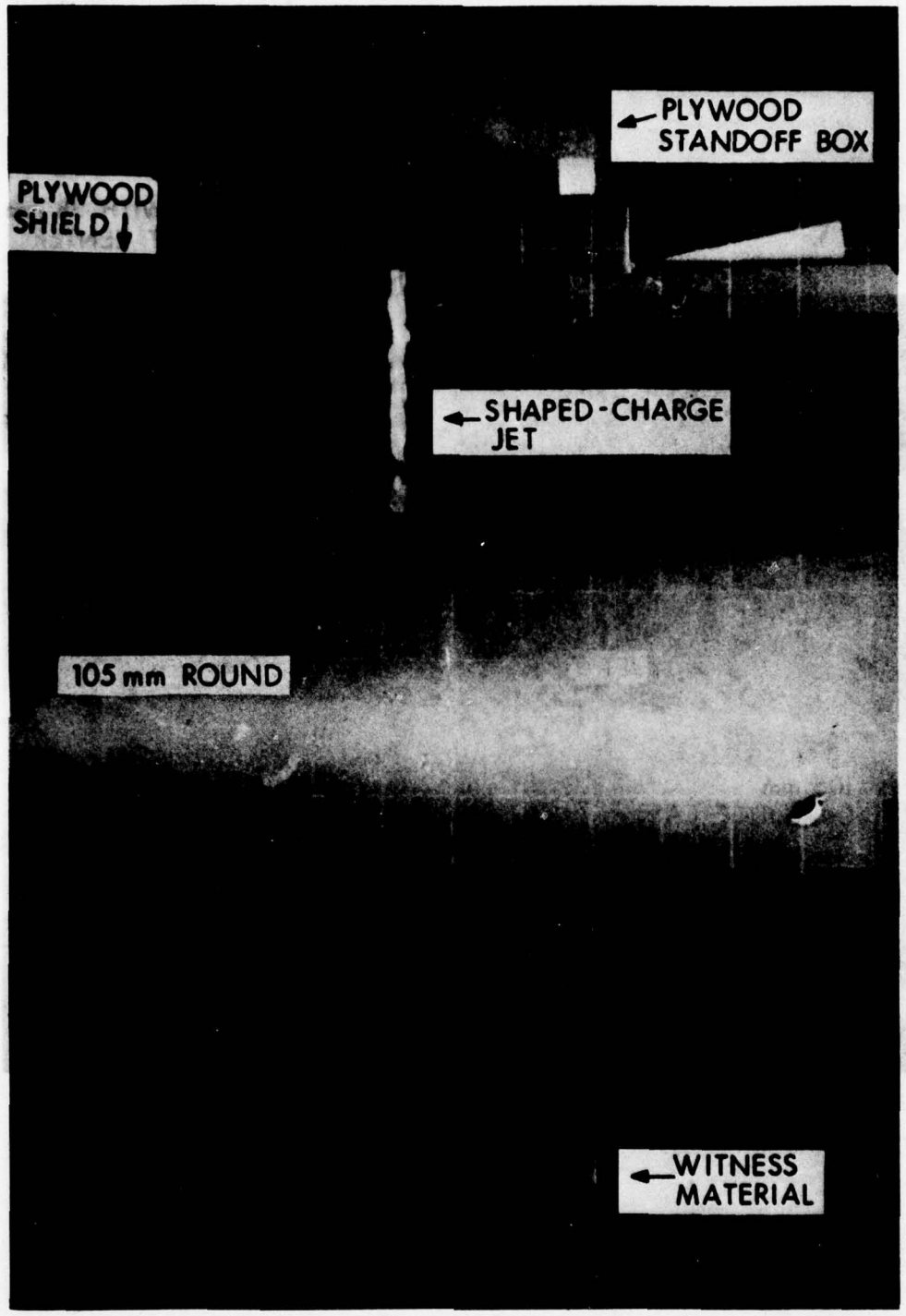

Figure 16. Photograph Taken 4.0 μs Prior to Impact for Test 7

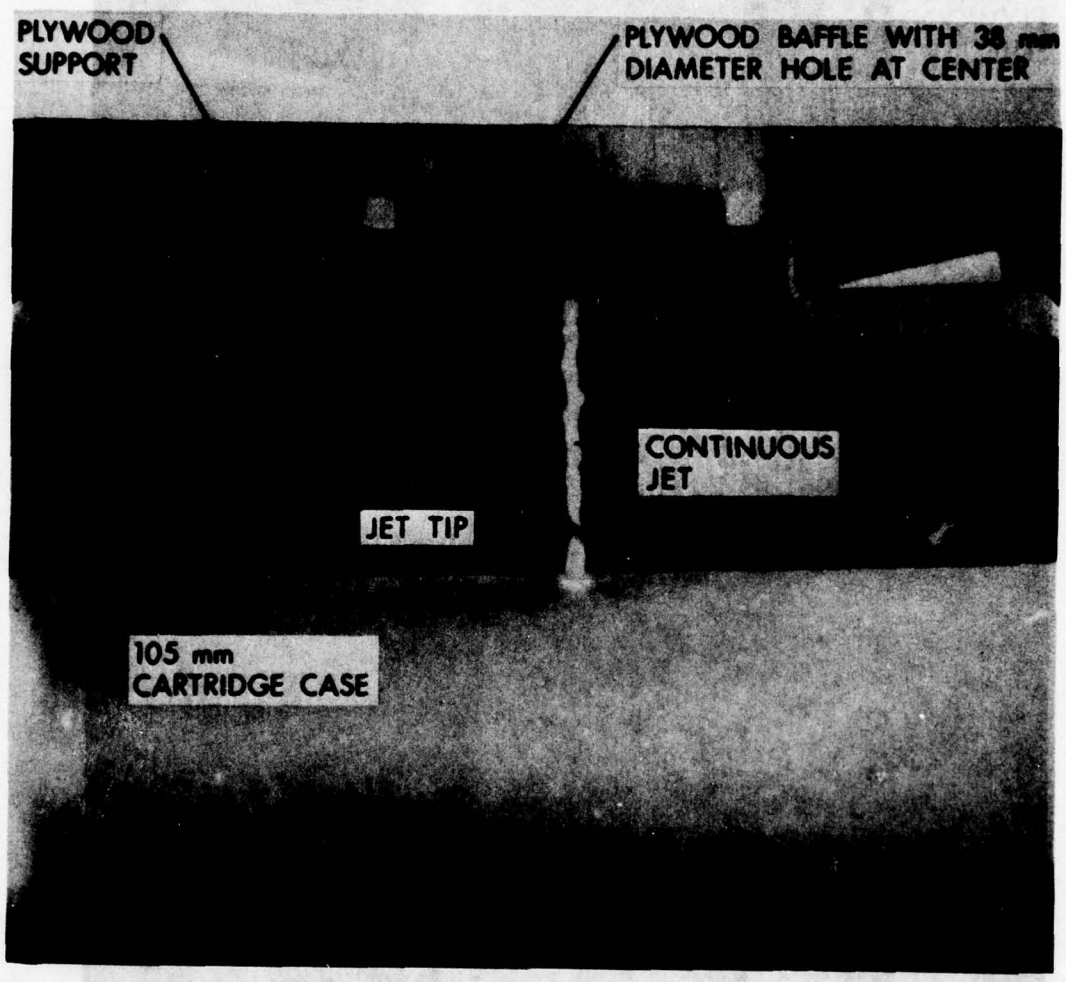

Figure 17. Photograph Taken at Time of Impact for Test 7

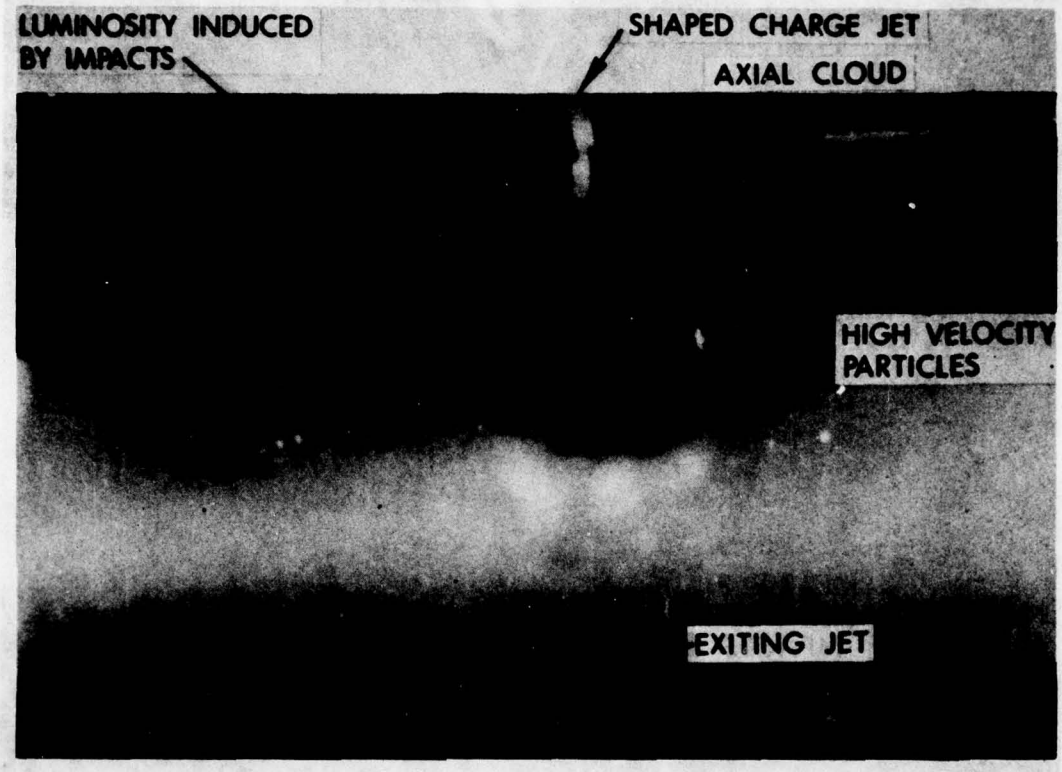

Figure 18. Photograph Taken 48.0 μs after Impact for Test 7

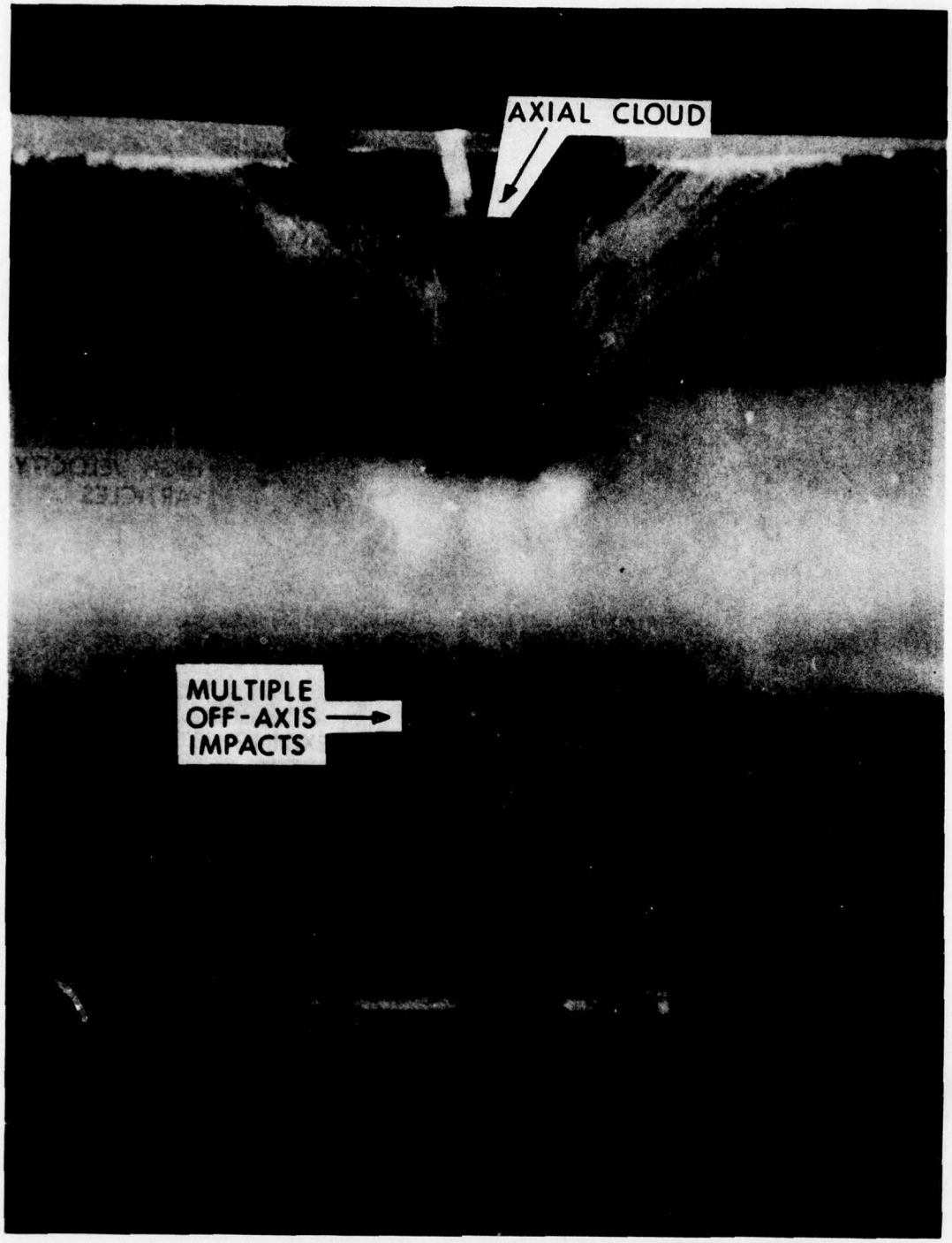

Figure 19. Photograph Taken 52.0 μs after Impact for Test 7

PHOTOGRAPH TAKEN 88 μs AFTER SHAPED CHARGE JET IMPACTED THE 105 mm ROUND

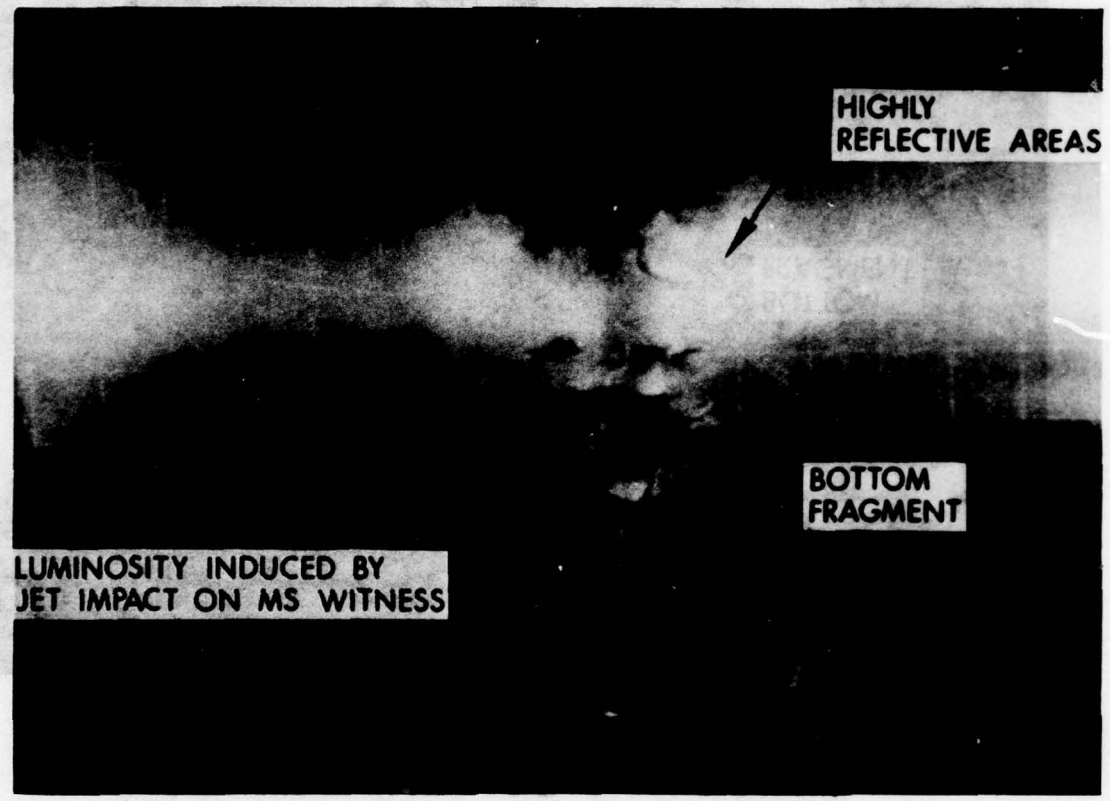

Figure 20. Photograph Taken 88.0 μs after Impact for Test 7

PHOTOGRAPH TAKEN 112 μs AFTER SHAPED CHARGE JET IMPACTED THE 105 mm ROUND

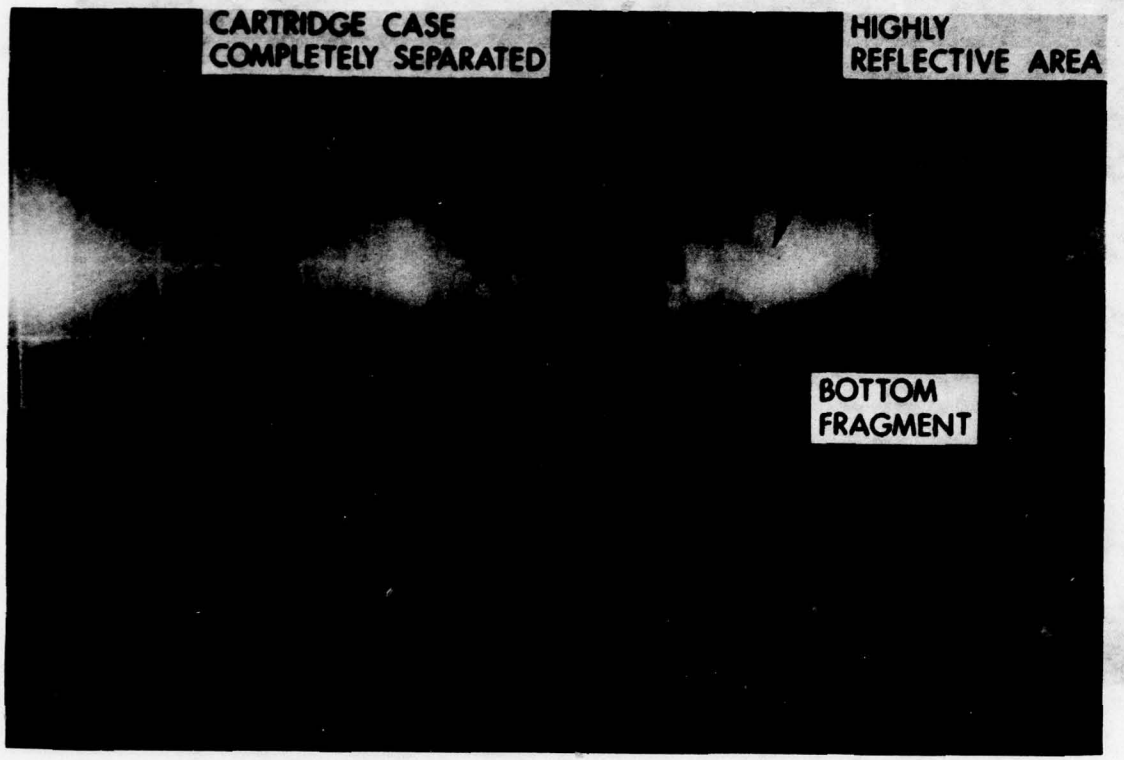

Figure 21. Photograph Taken 112 µs after Impact for Test 7

the jet may acquire a substantial amount of energy. For example, the average speed (see Table III) of the fragment labeled "Bottom Fragment" in Figures 20 and 21 was measured for twelve consecutive frames. This average speed, combined with the fragment's mass (≈ 10 gr), could induce a reaction if the fragment impacted another live 105 mm round[14]. Secondly, the two highly reflective areas illustrated in Figures 20 and 21 were monitored out to 168 μs after impact. The authors believe these two reflective areas to be highly distorted case-material which are driven by the propellant reaction. Therefore, monitoring these areas should provide insight into the propagating reaction*. The observed speed (1.32 ± 0.2 km/s) is fairly close to an estimated separation-speed of 1.1 km/s based upon a radiographically-inferred burning rate[15] of 0.55 km/s.

III. DISCUSSION

In this section we will review various interpretations of the experimental results, introduce the concept of three types of jet/propellant reaction, discuss the correlation between deposited kinetic-energy and the type of reaction, and lastly, present some data obtained for hypervelocity particles.

A. Interpretation of Experimental Results.

One possible interpretation of the data in Table II and Figures 4-11 is that there is no distinction between violent events, and that $\langle p \rangle_{105} \leq 75$ mm always induces a non-violent event. However, the authors will show that this interpretation is erroneous because of two observations. First, there are definitely various types of violent events** and second, unless one accounts for penetrator diameter, there is no *a priori* value of penetration which acts as a demarcation between the violent and non-violent events.

14. D.L. Collis, J.F. Forster, and J.P. McLain, "Vulnerability of Propellant-Filled Munitions to Impact by Steel Fragments," Ballistic Research Laboratory Contract Report No. 65, March, 1972.
15. J.N. Majerus, T.H. Martin and W.H. Jones, "Interaction Between Shaped Charge Jets and Granular Media," Ballistic Research Laboratory Memo. Report No. 2655, August, 1976. (AD #B013221L)

* Appendix C discusses an ionization probe test used to measure the propagating flame front. The results of this test indicate that the propagation rate rapidly slows down, and has a value around 0.8 km/s at a location 100 mm from jet impact.

**There are two other independent-sources of this observation. First, ammunition-compartment studies conducted at MTD have yielded reactions with <CGP> (at the base) ranging from ten MPa to several hundred MPa. Secondly, live 105 mm rounds which were impulsively loaded[4] using a sheet of explosive wrapped partially around an exterior sleeve, produced events whose violence ranges from that of electrical ignition to considerably more violent than electrical ignition.

The first observation deals with the violence of the event. This violence was qualitatively ranked using the average nose and base pressure readings, the variations in the readings and the cartridge case damage. The results of this qualitative ranking are shown in Table IV. Also listed are the crush-gage pressure values and the qualitative cartridge-case damage. Overall, there appear to be three types of reactions associated with the impacted 105 mm round. These three types will be referred to as severe, moderate and non-violent. The first type (severe) is reminiscent of a deflagration of high explosive whereas the second type (moderate) is similar to that observed for an unconfined 105 mm round electrically ignited. The last type (non-violent) is analogous to hydrostatically rupturing the case, possibly due to hydrodynamic jet-pressures. Table IV also ranks each test according to decreasing severity within each type of reaction. Tests No. 4 and 6 were estimated to be of the same severity and hence listed on the same line in Table IV.

Table V lists a* comparison of the observed ranking of violence with predicted ranking of violence based upon various jet-parameters. The jet parameters are striking velocity (see Table I), stagnation or impact pressure, jet diameter (see Table I), estimated penetration capability $\langle p \rangle_{105}$, and the jet's energy or momentum lost while perforating the propellant bed. Note that, since all the jets were of the same material, the ranking based on impact or stagnation pressure will be exactly the same as the ranking based on the striking velocity.

The estimated penetration-capability (on an average basis) was determined either from known penetration versus standoff behavior for free-flight jets (Tests No. 7-10), experimentally measured (Test No. 3), or else calculated using the modified DSM theory[9] and the known jet-characteristics and penetration-standoff data for each particular charge (Tests 1,2,4-6). The uncertainties (on an average basis) for these calculated penetrations are about ± 25 mm. The calculated values of deposited (lost) jet-energy and momentum are based upon the assumptions of an incompressible, constant diameter, ideal-jet perforating an incompressible propellant bed. The model and computer program used to calculate these values can be found in reference 16.

Certain observations can be made from inspection of Table V. First of all, striking velocity (or stagnation pressure or Hugoniot pressure) cannot be the critical parameter since two of the non-violent reactions are predicted to be severely violent, and three fourths of the severe reactions are predicted to be non-violent. The next parameter, jet diameter, predicted the tests to

16. J.N. Majerus, and J. Barb, "IMPULSE: Computer Program For Estimating Impulse, Energy and Pressure Applied by a Perforating Jet," Ballistic Research Laboratory Memorandum Report in preparation.

*Entries on the same line within a box indicate approximately - equal predicted violence.

TABLE IV

QUALITATIVE RANKING OF THE VIOLENCE INDUCED

BY A SHAPED-CHARGE JET IMPACTING A 105 mm ROUND

Violence of Event			Test Number	Crush-Gage Pressure Readings (MPa) Base Actual	Base Average	Nose Actual	Nose Average	Cartridge Case Damage
Decreasing Violence →	High Pressure Events	Severe Violence	7	103,123,131	119	26.2,35.2,45.1	35.5	Medium and small fragments
			3	91.8,107	99.4	36.5,40.3	38.4	" "
			4,6	4: Gages Damaged		15.9,30.0,35.2	27.0	" "
				6: 82.7,103,128	104.6	18.0,21.7,26.6, 36.6	25.7	" "
		Moderate: Similar to Electrical Ignition	2	45.6,66.8	56.2	22.3,24.2	23.3	Large and small fragments
			5	41.3,44.7	43.0	9.3,13.1,18.5, 19.3	15.2	" "
			1	38.6,40.0,42.1	40.2	15.0,16.7	15.9	" "
	Low Pressure Events	Non-Violent	9	11.7,11.7	11.7	3.8,5.0,8.3,12.4	7.4	Several tears + 1 fragment
			8	6.2,7.6	6.9	3.0,4.8,10.5,14.5	8.1	Split + 1 fragment
			10	2.1,4.8	3.4	2.3,3.8,4.1,4.8	3.8	Split open

TABLE V

COMPARISON OF OBSERVED TEST-VIOLENCE WITH

VIOLENCE PREDICTED USING VARIOUS JET-PARAMETERS

		Predicted Ranking of Test Violence Based Upon Various Jet-Parameters					
Violence of Event	Test Number	Striking Velocity v_s	Stagnation* or Impact** Pressure	Jet Diameter	Estimated Penetration Capability	Jet Momentum† Deposited	Jet Energy† Deposited
Severe	7 3 4,6	8,9	8,9	4-7	2 7,4,6	6,4,7 5	7 4,6
Moderate: Similar to Electrical Ignition	2 5 1	2,3	2,3	1-3	1,5,3	1-3	2,3,5 1
Non-Violent	9 8 10	1,4-7,10	1,4-7,10	10 8,9	8-10	8-10	8-10

+Decreasing Violence

* Stagnation pressure $\simeq 0.5\ \rho_T \left[v_s / \left(1 + \sqrt{\rho_T/\rho_j}\right) \right]^2$ GPa

** The Hugoniot pressure based upon the jet's striking velocity, and the material. Hugoniots associated with the propellant bed and the jet material.

† An ideal jet[12] perforating the propellant bed.

fall correctly within each type of reaction, except for tests No. 3 and 5. This indicates that jet diameter is strongly involved in governing the type of reaction. However, this parameter (jet-diameter) predicts no distinction between events within a specific type of reaction where the ranking is opposite to that observed. The remaining three jet parameters (penetration capability, and the jet's deposited momentum and energy) also predict the tests to fall correctly within each type of reaction, except for tests No. 2,3 and 5. Furthermore, these three parameters permit a ranking within each specific type of reaction. Hence, to select further from these parameters, one must compare the observed ranking for a specific test with the individual parameter for that particular test. If the parameter is the critical one, there should be a systematic change in the parameter with decreasing violence.

Table VI lists the observed test-violence and three jet-parameters corresponding to each test. Based upon the estimated penetration capability, test No. 2 should be the most violent. However, it yielded only a moderately violent reaction. Next, contrary to what was observed, tests No. 7,4 and 6 should be of equal violence (same penetration to within the uncertainty of ± 25mm), and less violent than test No. 2. Also, since the average penetration associated with test No. 1 is calculated (± 25 mm), it could be considered as having the same penetration capability as that associated with tests No. 8 and 9. This negates an inference that there is a 25 mm demarcation between the moderate and non-violent events, i.e., $\langle P \rangle_{105} \geq 100$ mm induces at least moderately violent events, whereas $\langle P \rangle_{105} \leq 75$ mm induces non-violent events.* This will be discussed further in Section III-C.

The remaining two parameters are the jet's deposited momentum and energy. Note that these parameters involve the jet's diameter which was already shown to strongly influence the type of reaction. Also, the value of energy or momentum associated with multiple jet impacts is obtained by adding together the individual values. This distinguishes between multiple and single impacts whereas this distinction is not possible using the penetration criteria. Therefore, it was intuitively felt that jet momentum or energy should yield a better correlation than penetration**.

---

* Also, private communication with Mr. F.T. Brown of VMT revealed that a value of $\langle p \rangle_{105} \simeq 60$ mm has caused violent high-pressure events when large-caliber shaped-charge warheads are involved in ammunition compartment studies.

** The impulsive tests[4] (which were conducted after the tests described in this report) have further substantiated this hypothesis.

TABLE VI

OBSERVED TEST-VIOLENCE AND SOME

JET-PARAMETERS CORRESPONDING TO EACH TEST

Violence of Event	Test Number	Estimated Penetration Capability(mm)	Momentum Deposited (kg-m/s)	Energy Deposited (Joules)
Severe	7	200	25.86	75,600
	3 (Off-Axis Particles)	100	9.42*	29,500*
	4	175	28.96	53,100
	6	175	31.33	56,500
Moderate: Similar to Electrical Ignition	2	300	9.42	29,500
	5	100	20.42	26,500
	1	100	6.23	12,900
Non-Violent	9	75	0.86	3,320
	8	75	0.43	1,660
	10	50	1.62	2,720

↓ Decreasing Violence

*These calculated values do not account for off-axis particles.

When momentum is used as the criterion (see Table V), it would have predicted all of the severely violent events (except for test No. 3). Also, none of the moderate events would have been predicted to be severely violent with the possible exception of test No. 5. However, the individual ranking of violence would be erroneously predicted. When energy is used, the individual ranking of violence is correctly predicted (except for test No. 3). Hence, it is hypothesized that deposited kinetic-energy is the critical parameter. Note that this parameter is also associated with the initiation of explosives[3] via shaped-charge jets. This hypothesis of a kinetic-energy criterion (associated with the three regions of violence) will now be discussed in further detail.

B. Kinetic Energy Hypothesis

Because of the small magnitudes of the crush-gage pressures $\langle CGP \rangle_{nose}$ associated with the nose location, the regions of violence are not dramatically illustrated using $\langle CGP \rangle_{nose}$. Therefore, the three regions of violence (non-violent, moderate and severe) are best seen using the average crush-gage pressures $\langle CGP \rangle_{base}$ at the base of the cartridge case. Figure 22 shows a schematic diagram of the three regions of violence with respect to pressure magnitudes and deposited kinetic-energy. The pressure levels shown for the various regions correspond to the pressure levels previously discussed, except that the upper bounds ($\simeq$ 20 and $\simeq$ 70 MPa) on the non-violent and moderate regions are somewhat arbitrary. No upper bound is shown if Figure 22 for the region of severe violence because it may be possible to achieve pressures on the order of 200 MPa. The two vertical dashed-lines denote the demarcations between the non-violent/moderate and the moderate/severe regions. These two demarcation-values of energy will be termed the *threshold-energy* values, E_I and E_{II}. Another important parameter shown in Figure 22 is the *threshold width* ΔE which is indicative of the uncertainty associated with the threshold energies. In general, a threshold width (ΔE_I and ΔE_{II}) may be associated with both of the threshold-energy values.

It is postulated that these threshold-energy values depend mainly upon the specific propellant*, whereas the influence of the jet/armor combination can be predicted using an appropriate jet-energy theory. Therefore, once the *threshold-energy values are determined experimentally* for a specific propellant*, *A posteriori* predictions of the level of violence could be made.

Figure 23 shows an application of the threshold-energy concept to the data in Table VI. This figure contains a plot of $\langle CGP \rangle_{nose}$ and $\langle CGP \rangle_{base}$ as a function of the deposited kinetic-energy. As noted earlier, there is a considerable difference in the crush-gage pressures associated with the nose and base locations. The threshold values E_I = 10 kJ and E_{II} = 50 kJ were somewhat arbitrarily selected. Since this study was not aimed at establishing specific criteria for M-30 propellant**, no attempt was made to ascertain the threshold widths.

---

* If the propellant casing is made from an energetic material the casing must also be considered.

** Such a study is currently being conducted using the methods and concepts presented in this report.

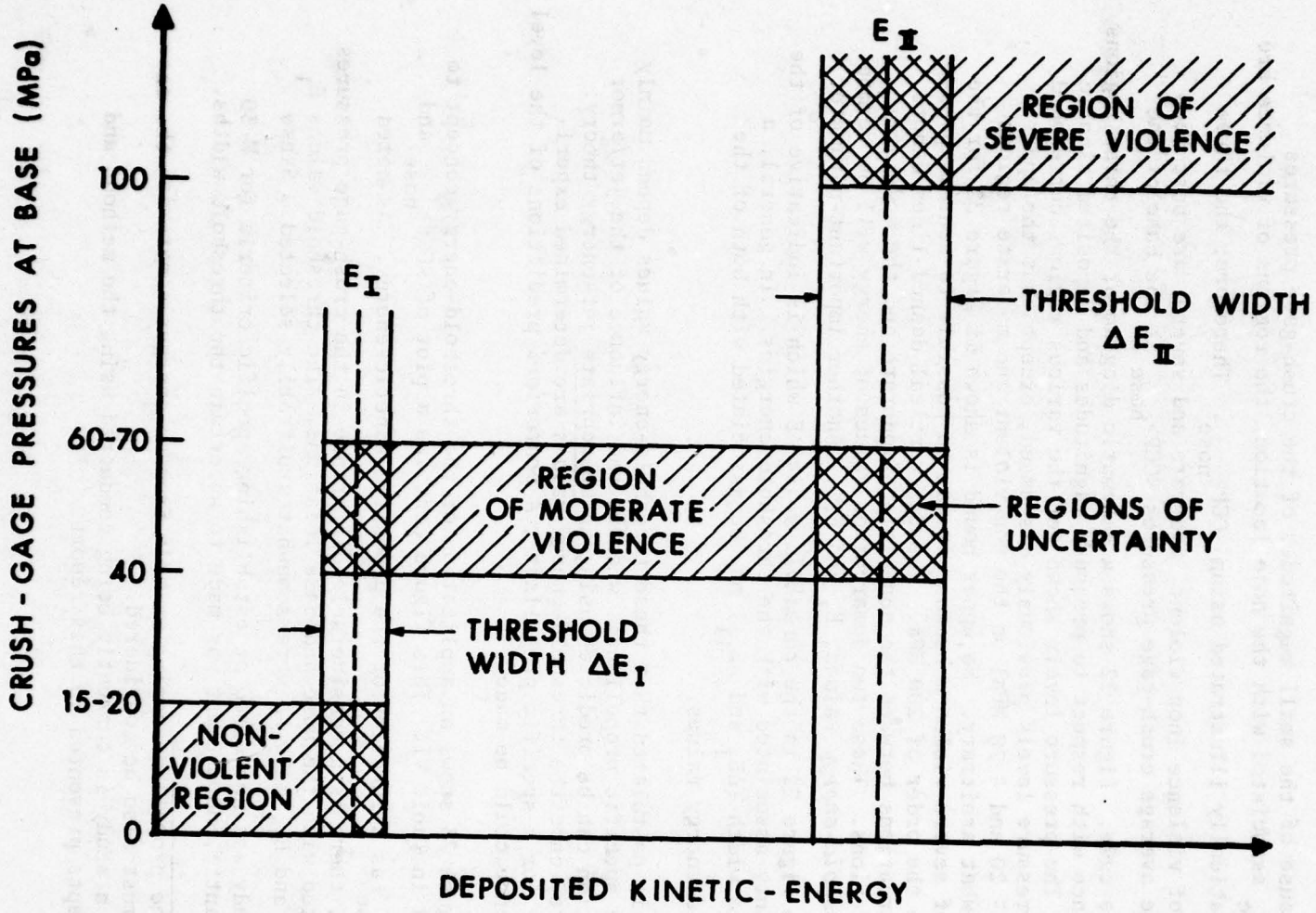

Figure 22. Schematic Diagram of the Three Regions of Violence with Respect to Pressure Magnitudes and Deposited Kinetic-Energy

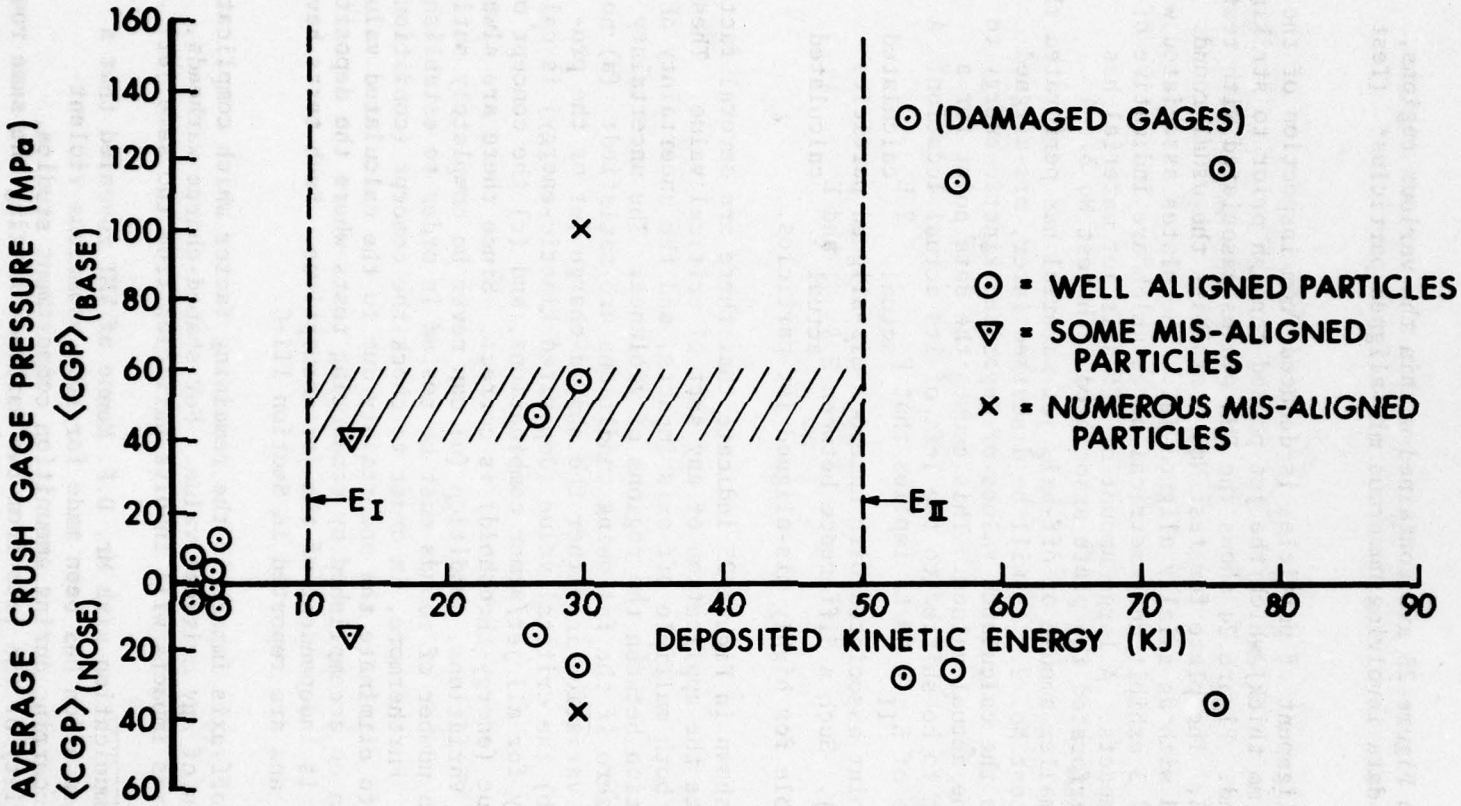

Figure 23. A Plot of the Deposited Kinetic Energy and Average Crush-Gage Pressure-Readings Associated with Tests Number 1 through 10

All the data in Figure 23 are contained within the various regions, except for the data involving numerous mis-aligned particles* (Test No. 3).

This misalignment of particles is deduced from inspection of the RHA plate (9.7 mm thick) which the jet passed through prior to striking the 105 mm round. Figure 24 shows the RHA plates associated with tests No. 1 through 3. The plate for test No. 2 exhibits the usual round hole associated with an axially aligned jet. The plates associated with tests No. 1 and 3 exhibit unsymmetrical holes which are indicative of off-axis jet impacts. A large amount of off-axis jet material has impacted and perforated the plate associated with test No 3. A considerably smaller amount of off-axis jet material has perforated the plate used in test No. 2. As will be discussed later, mis-aligned particles cause the calculated values of deposited kinetic-energy to be less than the actual values. This causes the data point for a mis-aligned jet to be shifted to the left of its actual location. A threshold value of E_{II} = 50 kJ implies that $E_{actual} \simeq 2\ E_{calculated}$ for the data point associated with numerous mis-aligned particles (see Figure 23). Such a difference between E_{actual} and $E_{calculated}$ is quite possible for highly mis-aligned jet-particles.

The data shown in Figure 23 indicate that there are several factors which complicate the application of any sort of critical value. These factors involve both multiple off-axis impacts, and the uncertainty ΔE of the demarcation between the regions of violence. The uncertainty ΔE approaches zero if the following conditions are satisfied: (a) no round-to-round variation in either the shaped-charge jet or the propellant bed, (b) the critical value (deposited kinetic-energy) is calculated exactly for all jet/armor combinations, and (c) the concept of a critical value (energy-threshold) is correct. Since there are always round-to-round variations, condition (a) can never be completely satisfied. Hence, a number of rounds must be tested in order to establish both E and ΔE. Furthermore, in order to check the concept (condition c), one needs to eliminate the uncertainty due to the calculated value of E. This can be accomplished by conducting tests where the deposited kinetic-energy is independent of the jet assumptions. Such tests have been conducted and are reported in Section III-C.

Multiple off-axis impact is the remaining factor which complicates the application of any critical value. For shaped-charge warheads, multiple off-axis impacts will involve particles from the same jet**.

---

* Private communication with Mr. D.F. Menne of VMT revealed that a similar observation has been made for some anomalous violent-reactions occurring during ammunition compartment studies.

** The probability of the jets from two warheads hitting the same round of ammunition is quite low. If multiple jets attack the same round, the spacing (both spatial and temporal) between impacts is a critical parameter which must be considered.

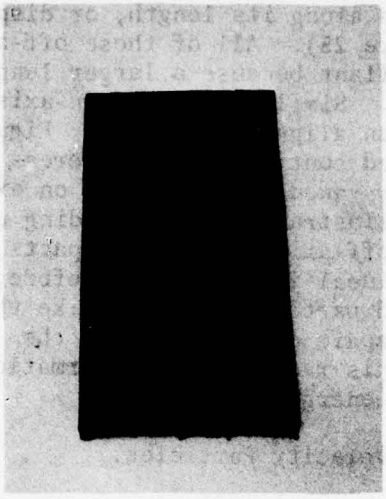

TEST No. 1

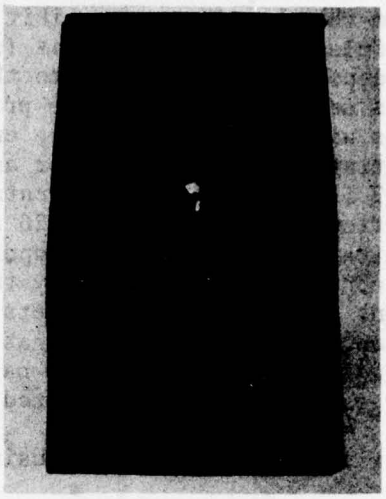

TEST No. 3

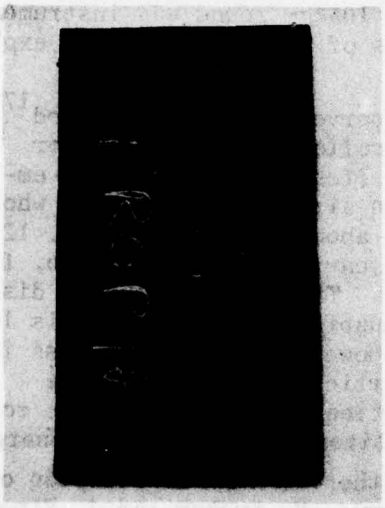

TEST No. 2

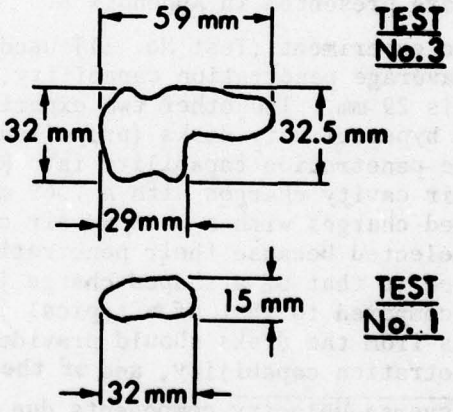

HOLE CONTOURS

Figure 24. Holes Induced in 9.7 mm Thickness of RHA by Jets Associated with Tests 1 through 3

These off-axis impacts are due to continuous jets which either curve* away from the shot-line or exhibit waviness along its length, or dispersed jet-particles traveling off-axis (see Figure 25). All of these off-axis impacts deposit more energy into the propellant because a larger length of jet is used to perforate the propellant. Similarly, yawed on-axis particles will also deposit more energy than aligned particles. Figure 26 illustrates the situation for an inclined continuous-jet, whereas Figure 27 is a schematic representation for yawed jet-particles on axis. The equations shown in Figures 26 and 27 illustrate that, depending upon the inclination and other jet conditions, off-axis and yawed impacts can deposit considerable more energy than the ideal-jet case. Therefore, if situations arise where curved jets or yawed particles might strike the ammunition, it is recommended that radiographic observations of the jet's condition be made. Then, based on this radiographic information, a better estimate of the deposited kinetic-energy can be made.

C. Verification of Hypothesis Using Hypervelocity Particles.

Since the calculated values of the jet's kinetic energy are dependent upon various assumptions concerning the jet, we would like to confirm the violence versus energy results by an independent method. If we used a hypervelocity particle whose mass was entirely expended in penetrating the propellant bed, then the deposited kinetic energy is known. Therefore, three experiments were conducted using hypervelocity particles of known mass and velocity. The 105 mm round was instrumented as discussed in Section IIA and the details of the hypervelocity experiments are presented in Appendix B.

One experiment (Test No. 11) used a hypervelocity aluminum rod[17] whose average penetration capability into rolled homogeneous armor (RHA) is 29 mm. The other two experiments (Tests No. 12 and 13) employed hypervelocity disks (propelled by an air-cavity charge[18]) whose average penetration capability into RHA is about 13 mm. Test No. 12 used air cavity charges with a 7.62 mm air cavity whereas test No. 13 employed charges with a 5.08 mm air cavity. These hypervelocity disks were selected because their penetration capability and velocity is low compared to that of a shaped-charge jet. However, the disk's mass is large compared to that of a typical jet particle. Therefore, the results from the disks should provide additional insight into the role of penetration capability, and of the deposited momentum versus energy.

*Transverse-velocity components due to either warhead fabrication or terminal flight-characteristics (J. Majerus, V. Kucher and J. Simon, "Influence of Transverse Velocity Upon The Penetration Performance of Shaped Charge Warheads," Ballistic Research Laboratory Memo. Report No. 2742, April 1977).

17. A Merendino, J.M. Regan, and S. Kronman, "A Method of Obtaining a Massive Hypervelocity Pellet From a Shaped Charge Jet," BRL Memorandum Report No. 1508, August 1963. (AD #425673)
18. J.H. Kineke and L.S. Holloway, "Macro-Pellet Projection With an Air Cavity High Explosive Charge, "BRL Memorandum Report No. 1264, April 1960. (AD #237944)

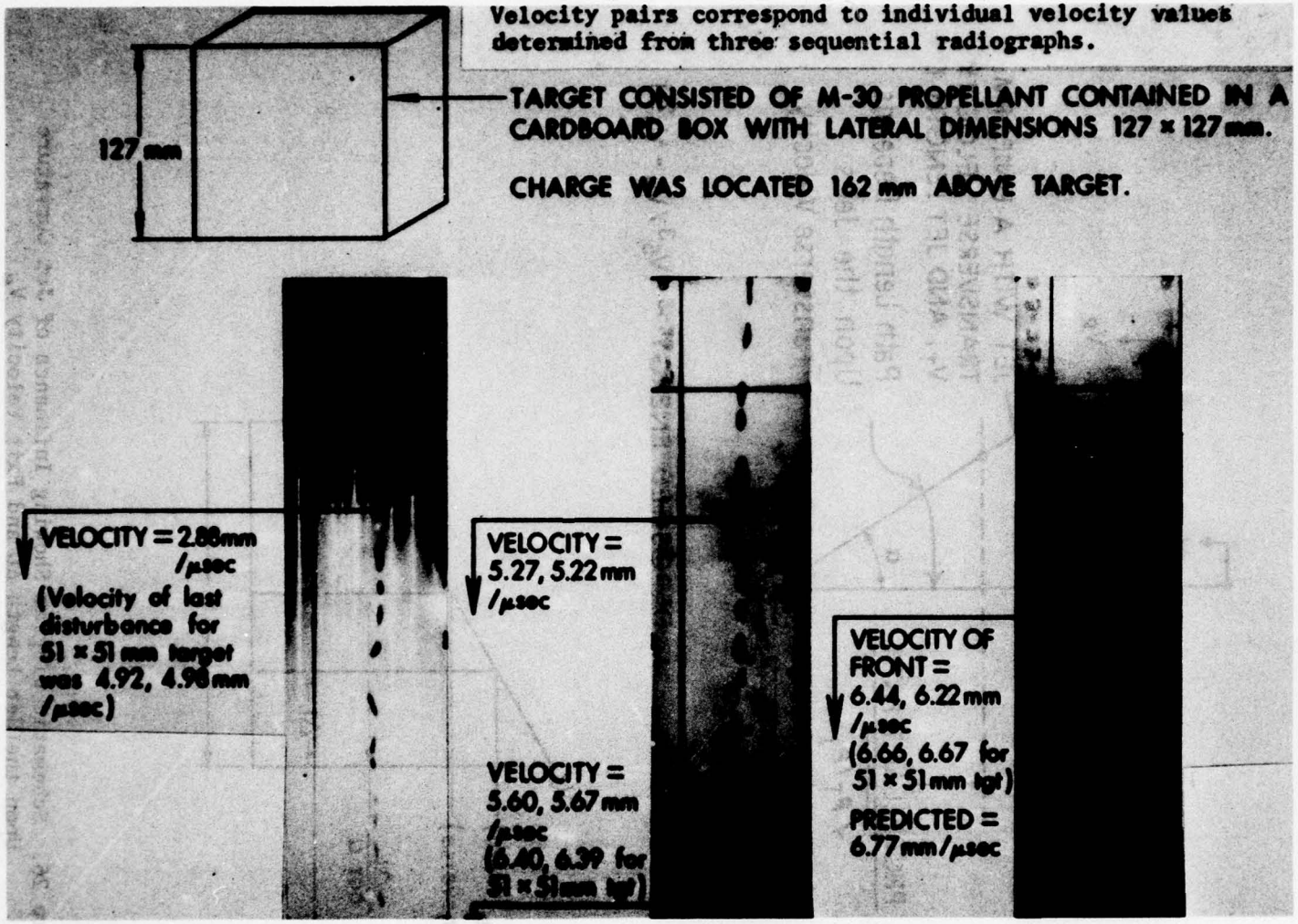

Figure 25. Radiographs Taken of a Shaped-Charge Jet after Passing Through M30 Propellant Beds of Various Sizes

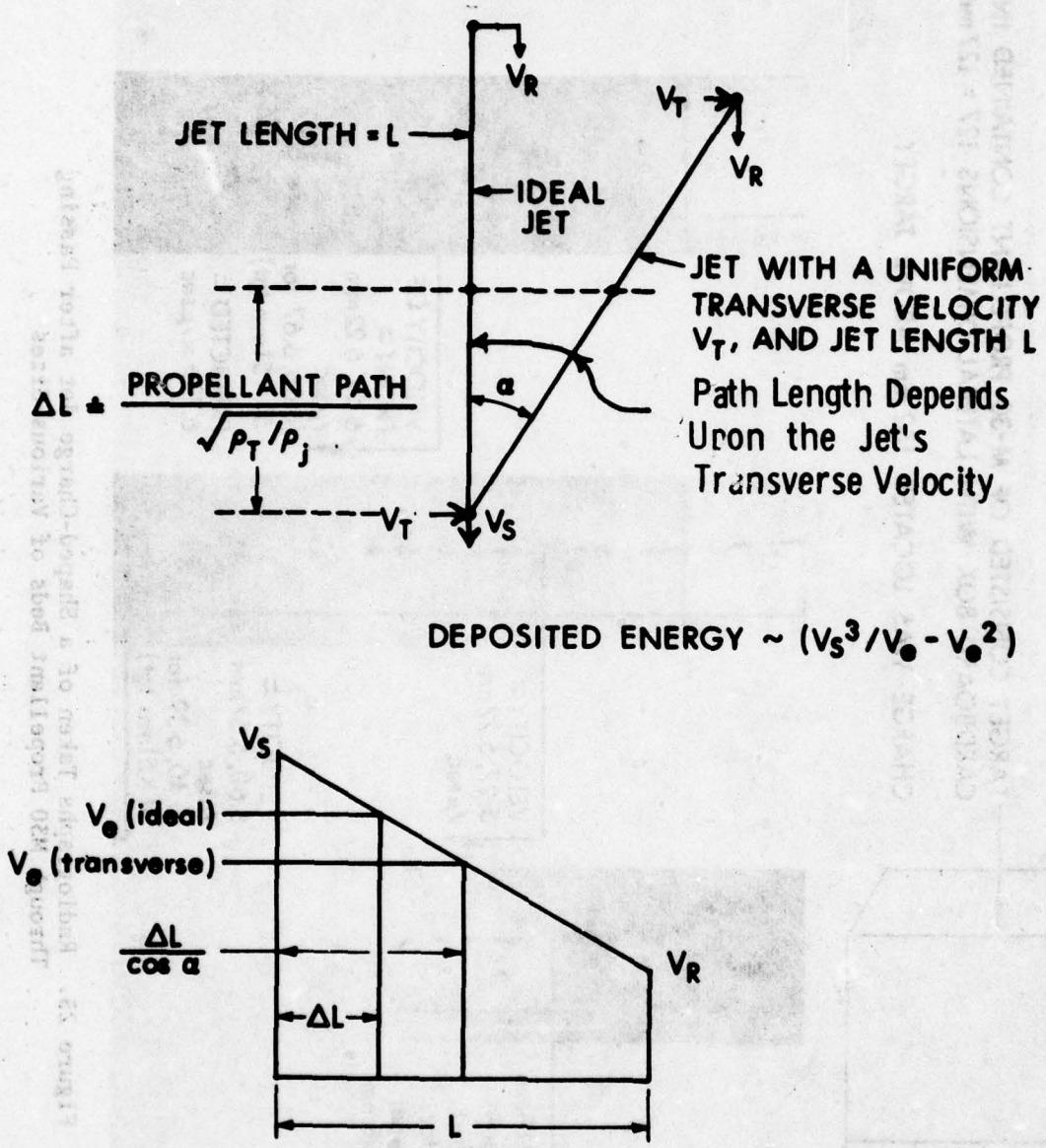

Figure 26. Schematic Diagram Showing Influence of Jet Curvature Upon the Jet Length ΔL and Exit Velocity V_e

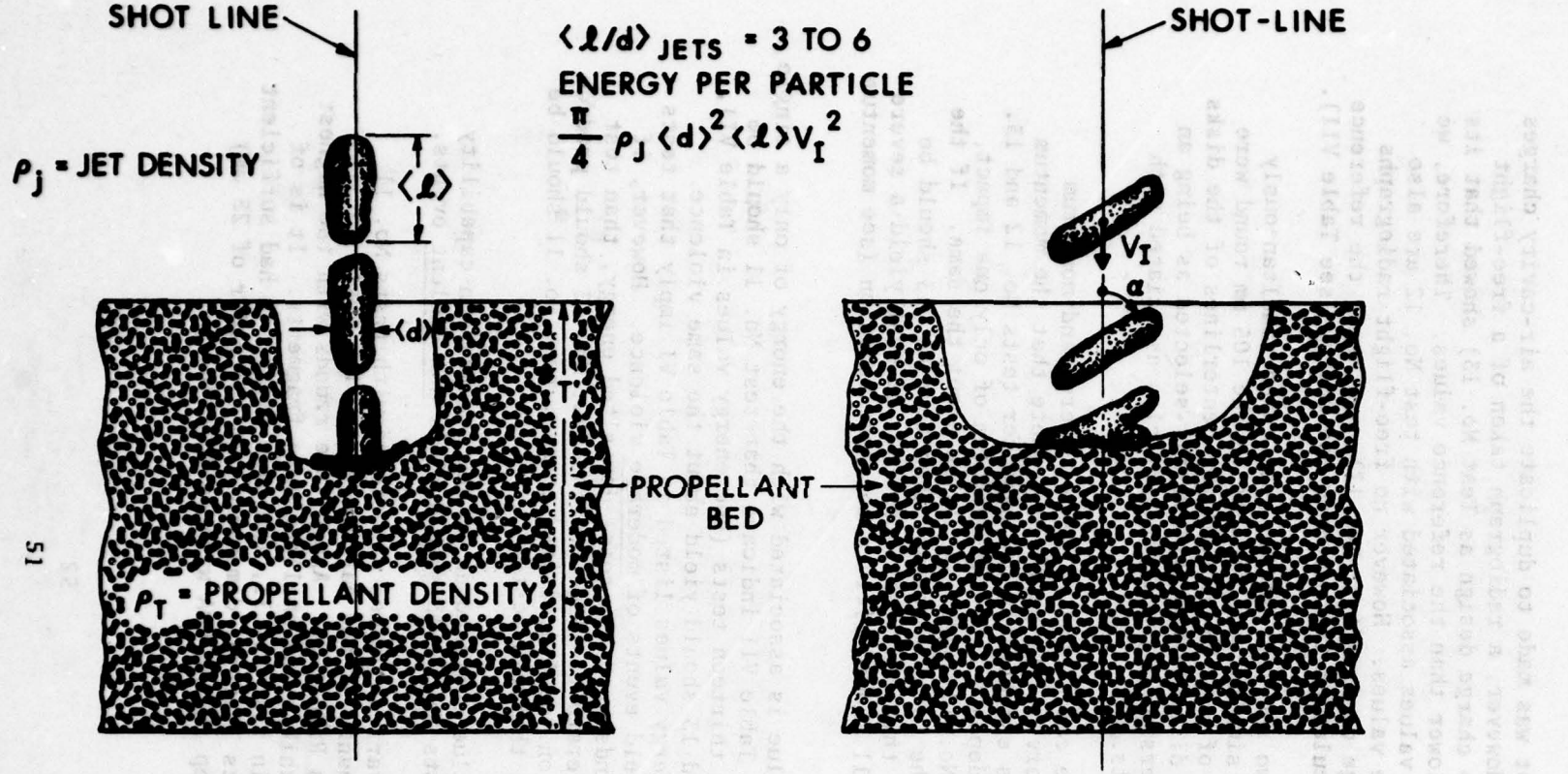

$$\text{No. OF PARTICLES CONSUMED} = \frac{T\sqrt{\rho_T/\rho_J}}{\langle \ell \rangle}$$

$$\frac{T\sqrt{\rho_T/\rho_J}}{\langle d \rangle + (\langle \ell \rangle - \langle d \rangle)\cos \alpha}$$

(assuming hemispherical nose on particles)

Figure 27. Schematic Diagram Showing Influence of Particle Yaw Upon Number of Particles Consumed

Note that an attempt was made to duplicate the air-cavity charges used in reference 18. However, a radiograph taken of a free-flight hypervelocity disk (same charge design as Test No. 13) showed that its mass and velocity were lower than the reference values. Therefore, we suspect that the actual values associated with test No. 12 are also lower than the reference values. However no free-flight radiographs were taken of this charge design (test No. 12), and hence the reference values were used in calculating the momentum and energy (see Table VII).

Test No. 12 used two and test No. 13 used three simultaneously detonated charges. The simultaneous impacts on the 105 mm round were separated by a distance of 50.8 mm between the centerlines of the disks (see Appendix B). This distance was arbitrarily selected as being an upper bound on the dispersion between jet particles associated with multiple off-axis impacts.

Table VII lists the calculated values of energy and momentum associated with the hypervelocity particles. Note that the momentum for a single particle is essentially the same for tests No. 12 and 13. Hence, if the violence depends upon the momentum of only one impact, the violence for tests No. 12 and 13 should be about the same. If the violence depends upon the total momentum, then test No. 13 should be the most violent of all thirteen tests, test No. 12 must yield a severe reaction, and test No. 11 should yield a moderate reaction (see momentum values in Table VI).

If the critical value is associated with the energy of only a single particle, the values in Table VII indicate that test No. 11 should be the most violent of all thirteen tests (see energy values in Table VI), whereas tests No. 12 and 13 should yield about the same violence. Furthermore, the jet-energy values listed in Table VI imply that tests No. 12 and 13 should yield events of <u>moderate</u> violence. However, if the critical value depends upon the <u>total</u> deposited energy, than test No. 12 should yield moderate violence whereas test No. 13 should produce a <u>severe</u> event. Based on total deposited energy, test No. 11 should be the most violent of all thirteen tests.

If the critical value corresponds to the penetration capability being $\geq$ 75 mm, then tests No. 11-13 should yield <u>non-violent</u> events.

Table VIII lists various values associated with tests No. 11 through 13 and the remnants of the cartridge case for tests No. 11 through 13 are shown in Figure 28. Again, the rounds with the highest crush-gage pressures exhibit the smallest case fragments. It is of interest to note that in test No. 11, the case fragments had sufficient energy to leave imprints (lateral dimensions on the order of 25 mm) several millimeters deep in the RHA witness material.

TABLE VII. CALCULATED VALUES FOR HYPERVELOCITY PARTICLES

Test Number	Type of Particle	Energy of Each Particle Joule	Momentum of Each Particle kg-m/s	Total Deposited Energy Joule	Total Deposited Momentum kg-m/s
11	Aluminum Rod	81,500	19.3	81,500	19.3
12	2 Simultaneous Steel Disks	21,700*	14.6*	43,400*	29.2*
13	3 Simultaneous Steel Disks	16,800 (27,900*)	14.5 (19.5*)	50,400 (83,700*)	43.5 (58.5*)

* Based on the velocity and mass given in Reference 18.

TABLE VIII

VALUES ASSOCIATED WITH THE TESTS USING HYPERVELOCITY PARTICLES

Test Number	Type of Particle	Mass of Each Particle grams	Velocity of Each Particle km/s	Penetration Capability mm	Percentage of Propellant Recovered After Impact	Time Required After Impact for Base Plate to Travel 6.3 mm μs	Crush-Gage Pressure Readings Base MPa	Crush-Gage Pressure Readings Nose MPa
11	Aluminum rod	2.3(±5%)	8.36(±5%)	29	11	454	>133** 110	83,35 29,25
12	2 Simultaneous Steel Disks	4.88*	2.98*	13	53	1,153	3 @ 43 36	22,5.5
13	3 Simultaneous Steel Disks	6.2 (6.80*)	2.33 (2.87*)	13	27	632	>133** 106,81,43	9.7

* These values were taken from Reference 18

** Exceeded capacity of copper crush-gage.

Based upon the results shown in Table VIII and the cartridge-case damage, tests No. 11 and 13 are ranked as severely violent whereas test No. 12 is moderately violent. Note that test No. 11 was at least as violent as test No. 7 and, based upon the general debris and the imprints left on the RHA witness, may have been more violent than test No. 7. Since none of the events were non-violent, the results in Table VIII refute any criterion based upon penetration capability. Furthermore, the observed violence is contrary to the trends predicted for either single-particle momentum or total deposited-momentum. However, the predicted violences based upon the total deposited-energy are in agreement with the observed violences.

Both the jet energy data and the hypervelocity data are plotted in Figure 29. The energy values for the hypervelocity particles are the values associated with the total number of particles used in each test (see Table VII). Other than test No. 12, whose calculated energy value is probably too high, the hypervelocity particle results agree quite well with the results associated with the shaped-charge jets. This gives credence to the energy values calculated for the various conditions of the shaped-charge jets.

IV. SUMMARY

Our investigation has demonstrated that there are three types of violence associated with shaped-charge jet/propellant reactions. These types were labeled as: 1. a non-violent type which is similar to hydrostatically rupturing the case due to the localized hydrodynamic jet-pressure, 2. a moderately-violent type whose violence is similar to an electrically ignited round, and 3. a severely-violent type whose violence is similar to a deflagration of high explosive.

In the non-violent event, the cartridge case remains essentially intact, 40-70% of the propellant can be recovered after the test, and crush-gage pressures are 3-15 MPa. In the moderately-violent event, the cartridge case ruptures into numerous large-to-small pieces with some cartridge base-plate, and the average crush-gage pressures (at the base) are 40-60 MPA. The amount of recovered propellant for this event ranged from 9-22% for jet impact and was 53% for the hypervelocity particles. In a severely-violent event, the cartridge case ruptures into many medium-to-small pieces with no cartridge case remaining attached to the base-plate, and the average crush-gage pressures (at the base) are $\geq$ 100 MPa. The amount of recovered propellant (for this event) ranged from 9-16% for jet impact and 11-27% for the hypervelocity particles.

A variety of jet-parameters were investigated for *a priori* prediction of both the type of violence and the ranking of events within any specific type. These jet-parameters were striking velocity, impact pressure, jet diameter, penetration capability and the jet's momentum or kinetic energy deposited into the propellant bed. Of these parameters,

TEST NO. 11

HYPERVELOCITY
ALUMINUM ROD

TEST NO. 13

THREE SIMULTANEOUS
HYPERVELOCITY DISCS

TEST NO. 12

TWO SIMULTANEOUS
HYPERVELOCITY DISCS

Figure 28. Cartridge-Case Remnants Associated with Tests No. 11 through 13

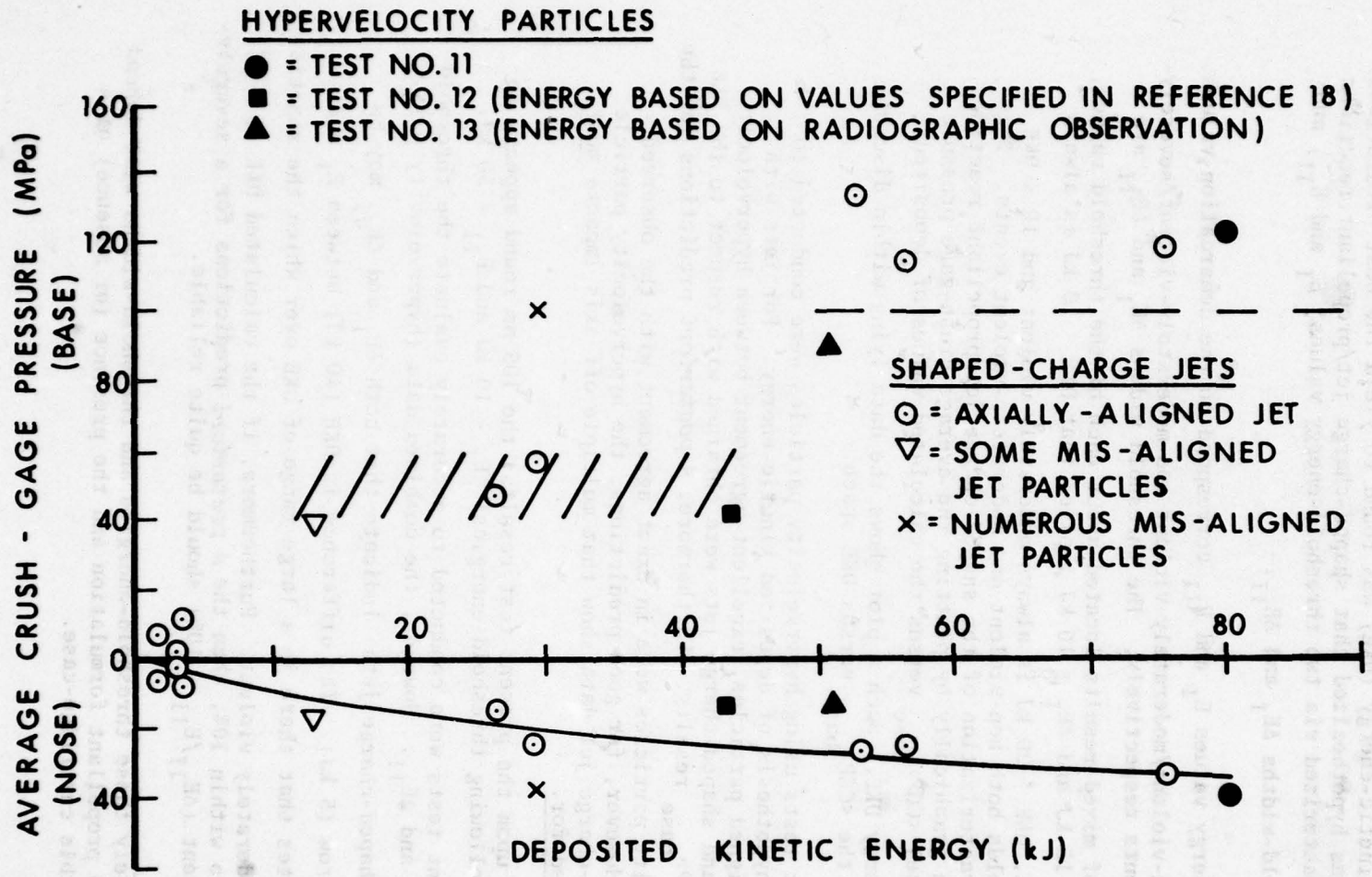

Figure 29. Correlation Between Deposited Kinetic-Energy and Average Crush-Gage Pressures for Both Shaped-Charge Jets and Hypervelocity Particles

deposited kinetic-energy (DKE) was found to yield the best predictions. Hence, it was hypothesized that shaped-charge jet/propellant reactions can be characterized via two threshold-energy values* E_I and E_{II}, and two threshold-widths ΔE_I and ΔE_{II}.

The energy values E_I and E_{II} correspond to the demarcation values between non-violent/moderately-violent and moderately-violent/severely-violent events respectively. The threshold widths ΔE_I and ΔE_{II} are the zones of mixed results located about each of the threshold values, e.g., $E_I \geq 15$ kJ and $\Delta E_I = 10$ kJ implies that DKE < 10 kJ is always non-violent, DKE > 20 kJ is always moderately violent and $10 \leq$ DKE ≤ 20 kJ yields both non-violent and moderately-violent events. This energy characterization of the shaped-charge jet/propellant reaction can be seen graphically by plotting the average crush-gage pressure (at the base) $\langle CGP \rangle_{base}$ versus the calculated values of deposited kinetic-energy DKE. Such a plot shows the data lying within discrete regions of the $\langle CGP \rangle_{base}$ versus DKE space.

Impact tests using hypervelocity particles were conducted to check the hypothesis of deposited kinetic-energy. For jets with axially-aligned particles, excellent agreement between hypervelocity particles and shaped-charge jets were obtained with respect to the DKE versus $\langle CGP \rangle_{base}$ results. Furthermore, *A posteriori* predictions for the hypervelocity particles were in exact agreement with the observed results. However, for good predictions, the hypervelocity particle and shaped-charge jet data show that multiple off-axis impacts must be accounted for.

Based upon the present test results, the 105 mm round appears to have the following threshold-energies: $E_I \simeq 10$ kJ and $E_{II} = 50$ kJ. Insufficient tests were conducted to accurately evaluate the threshold widths ΔE_I and ΔE_{II}. However, the combined data (hypervelocity particles and shaped-charge jets) indicate that both ΔE_I and ΔE_{II} may be fairly narrow (5 kJ). The difference in DKE (40 kJ) between E_I and E_{II} indicates that there is a large range of DKE over which the reaction is only moderately violent. Furthermore, if the calculated DKE is accurate to within 10%, then the *A posteriori* predictions for a severely-violent event ($\Delta E_{II}/E_{II} \simeq 10\%$) should be quite reliable.

---

* Most likely these threshold-energies and threshold-widths will depend upon the propellant formulation and the presence (or absence) of a combustible cartridge-case.

ACKNOWLEDGMENTS

The authors would like to thank Messrs. R. Carroll, J. Cullum, W. Jones and F. Harris who conducted the experiments described in this report.

APPENDIX A

FRAMING CAMERA OBSERVATIONS FOR TEST NO. 7

In this section the majority of the frame-by-frame observations for test No. 7 are shown. The frames missing are either those shown in Figures 17 through 22 or, the last 25 frames of observation. The time between each frame is 4.0 μs and the time shown in each figure refers to the time after impact.

The direction of jet travel is always from the top to the bottom of the photograph. The base of the cartridge case is always located to the left-hand side of the photograph.

PRECEDING PAGE BLANK-NOT FILMED

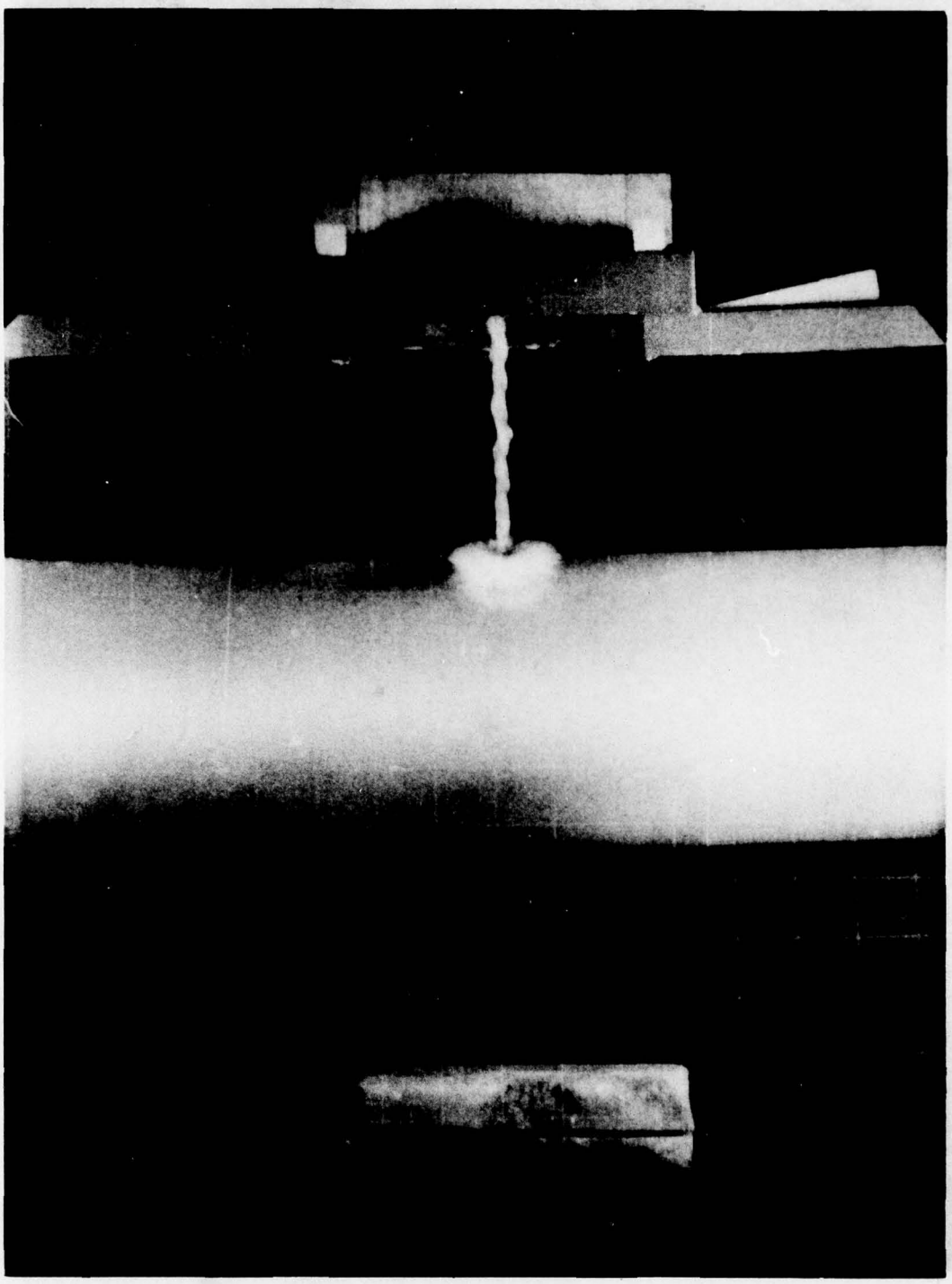

Figure A.1 Observation at 4 μs after impact

PRECEDING PAGE BLANK-NOT FILMED

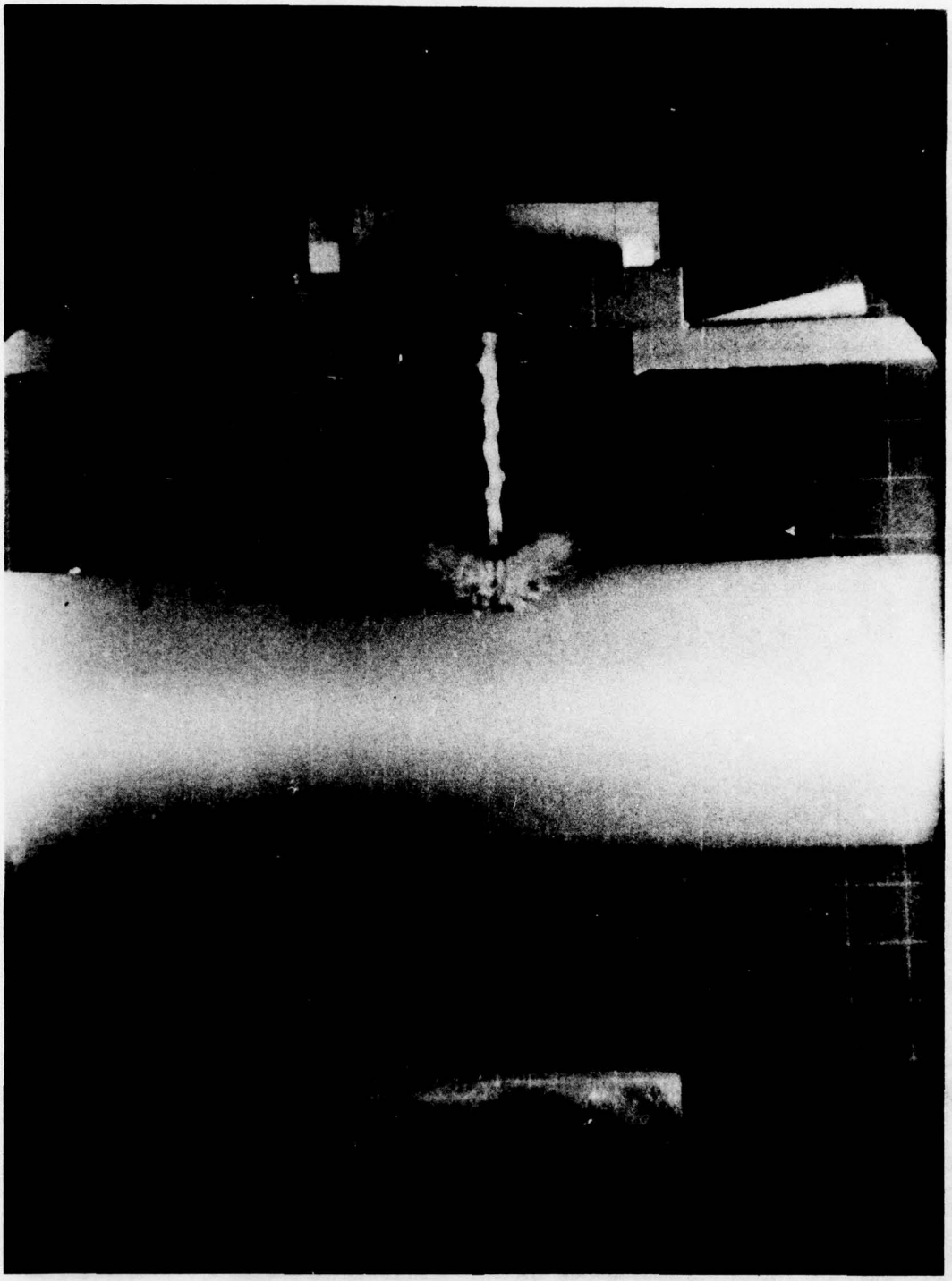

Figure A.2 Observation at 8 μs after impact

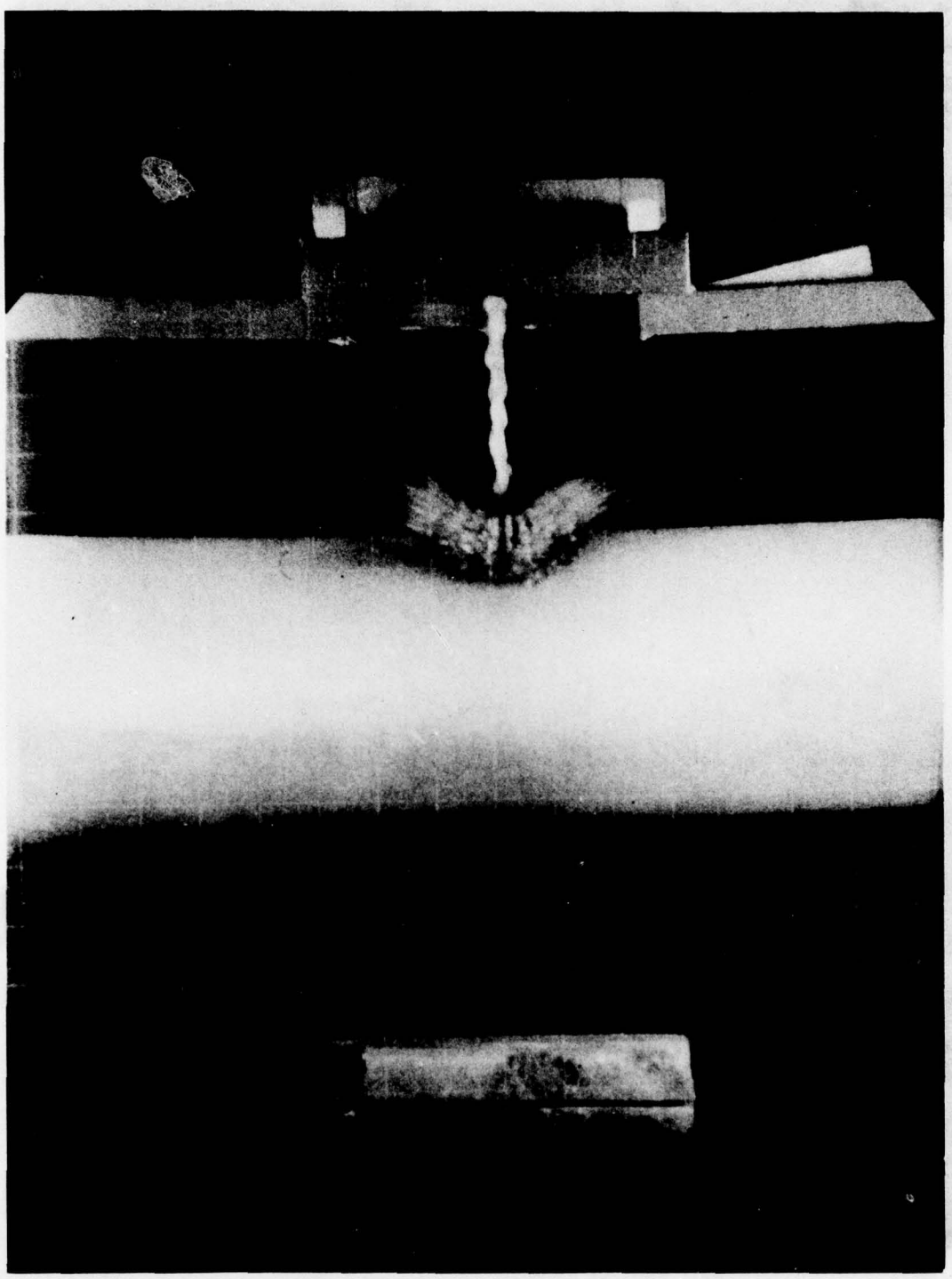

Figure A.3 Observation at 12 μs after impact

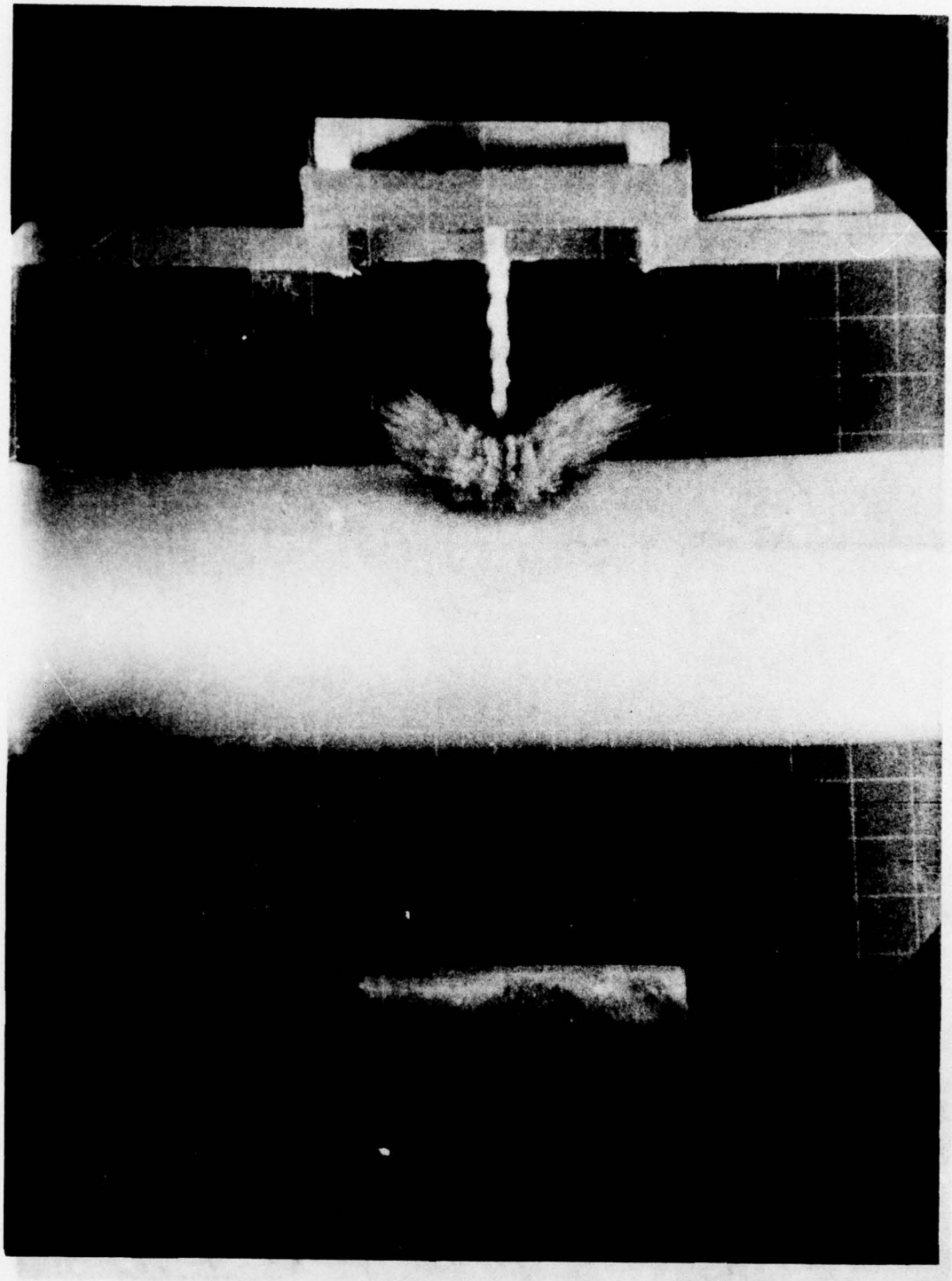

Figure A.4 Observation at 16 μs after impact

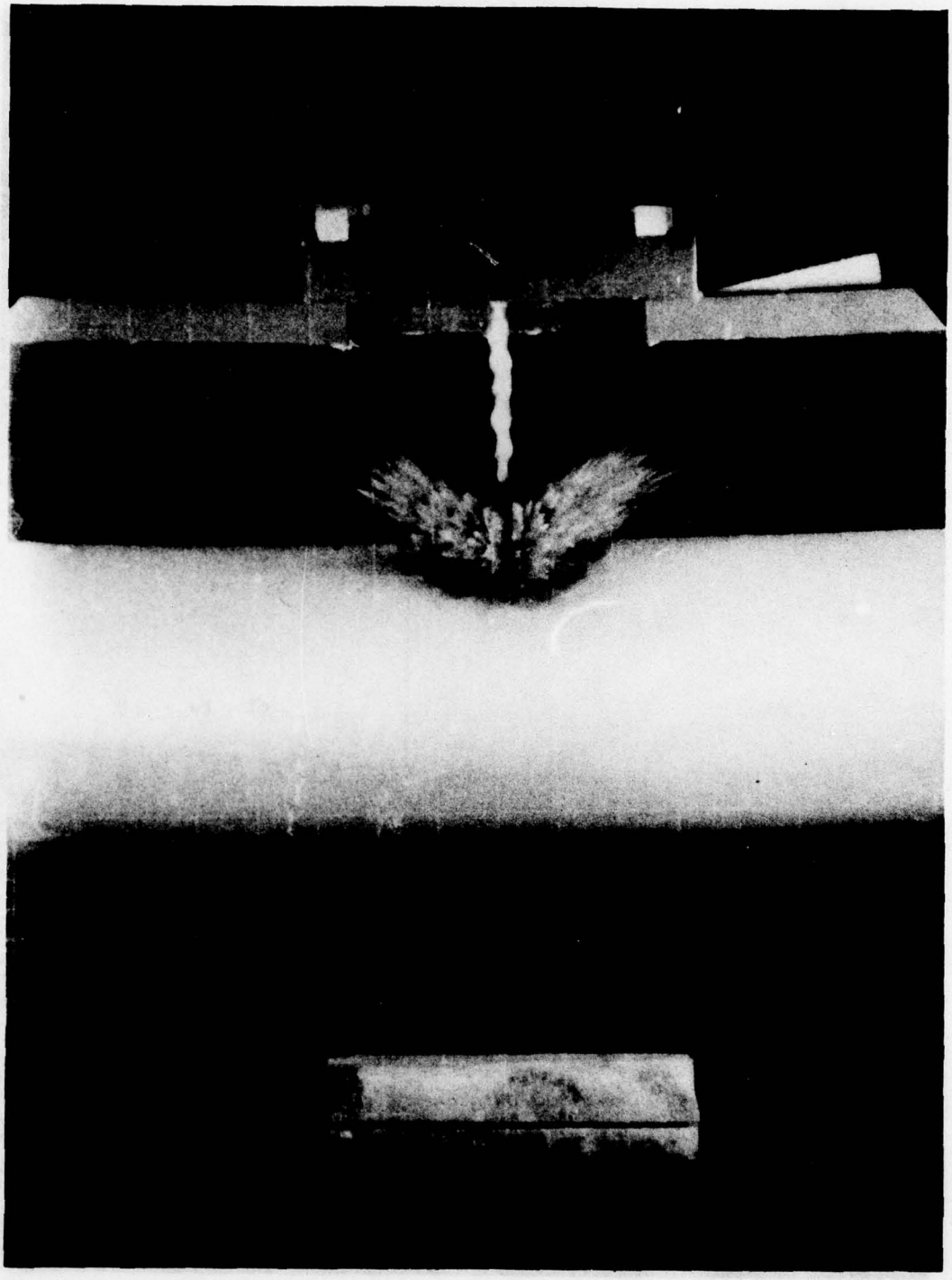

Figure A.5 Observation at 20 μs after impact

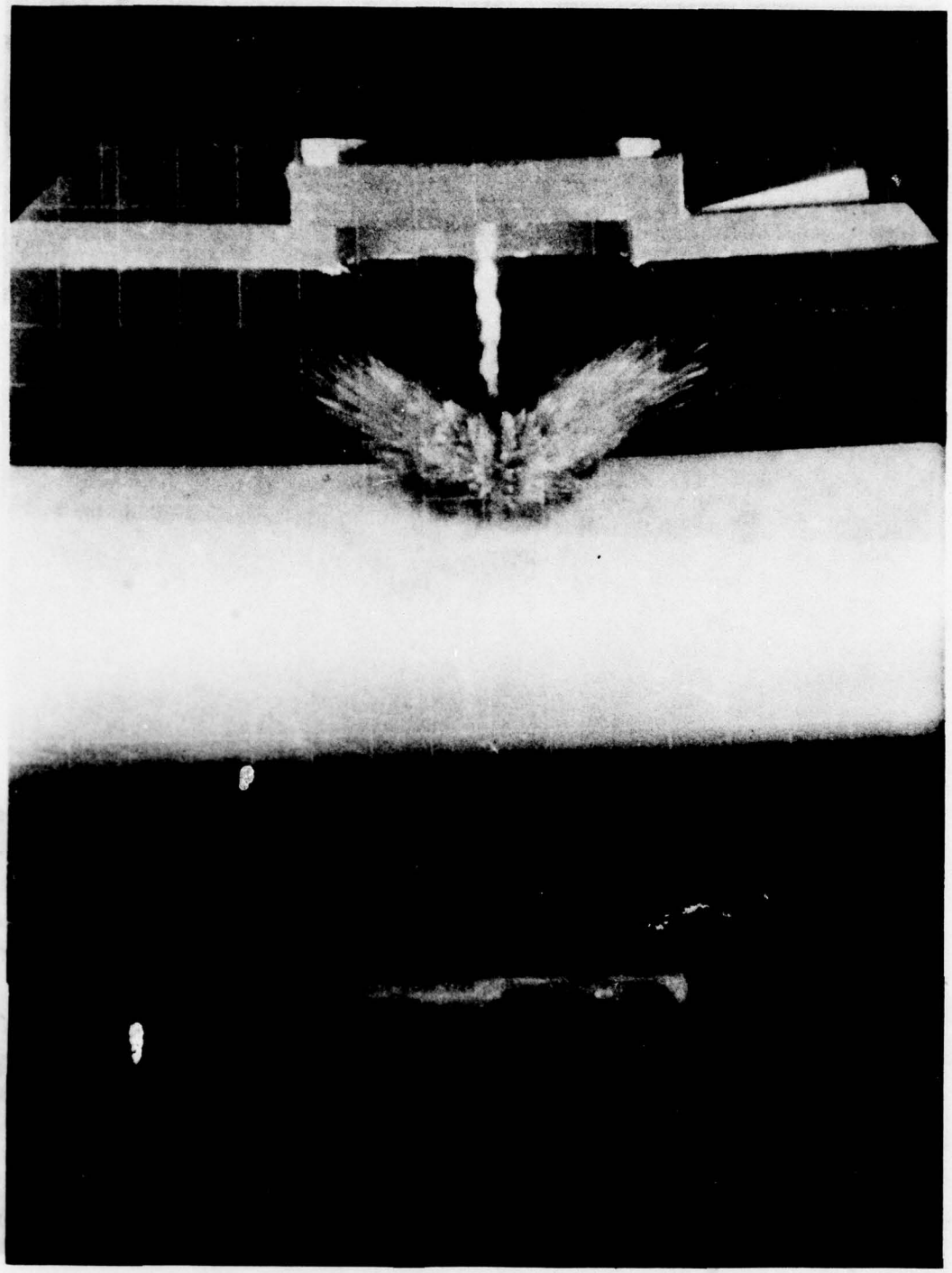

Figure A.6 Observation 24 μs after impact

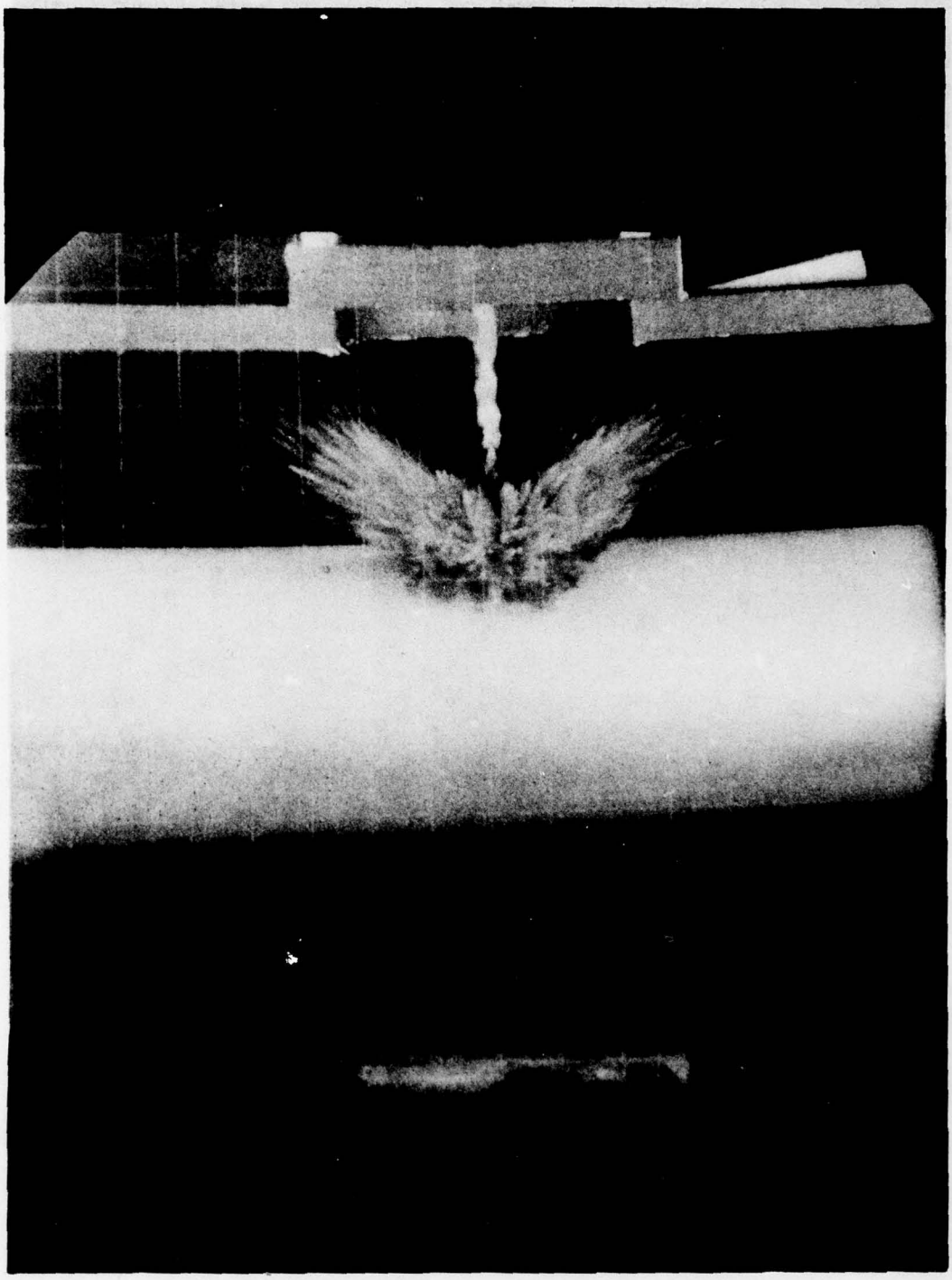

Figure A.7 Observation at 28 μs after impact

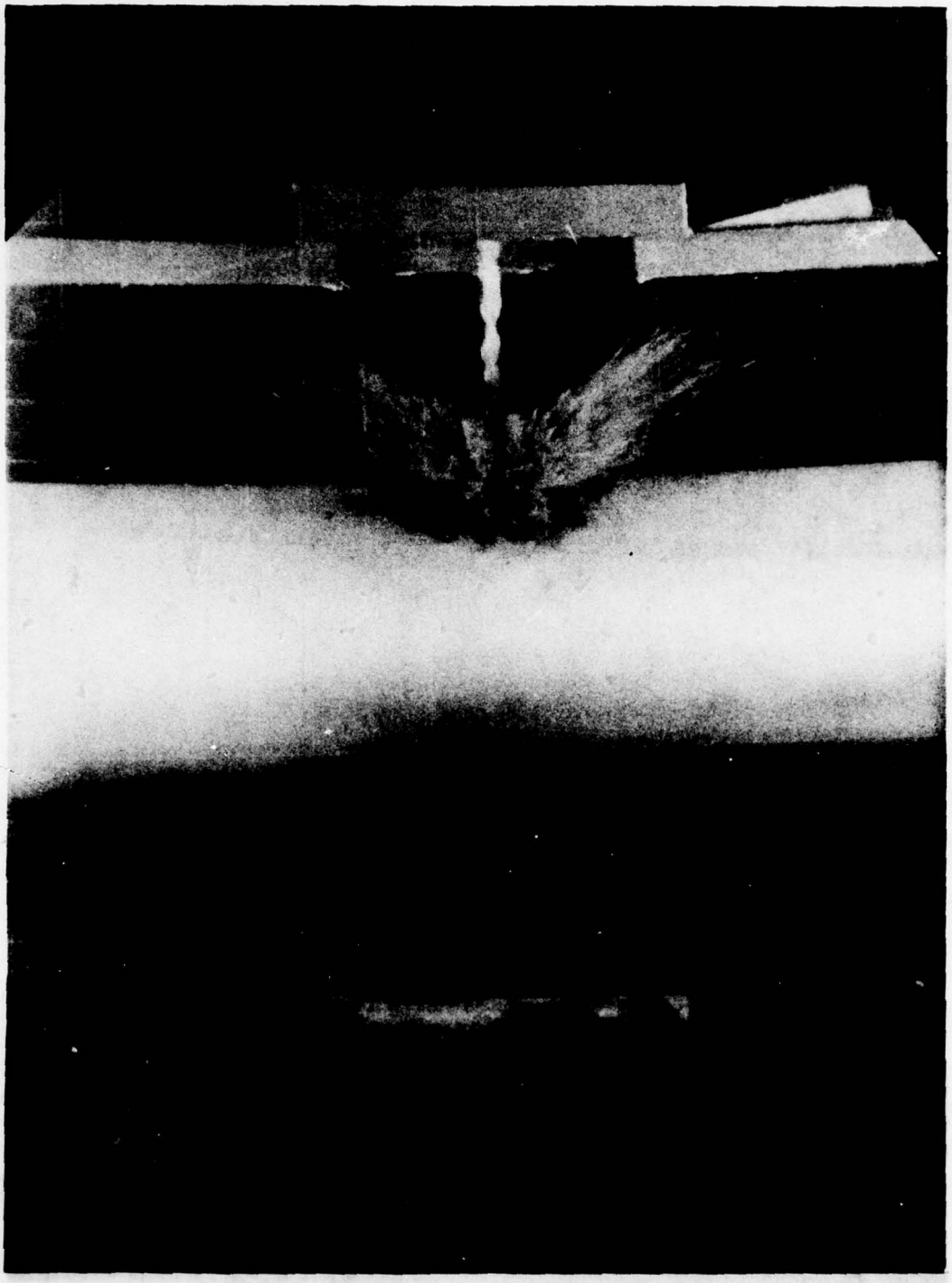

Figure A.8 Observation at 32 μs after impact

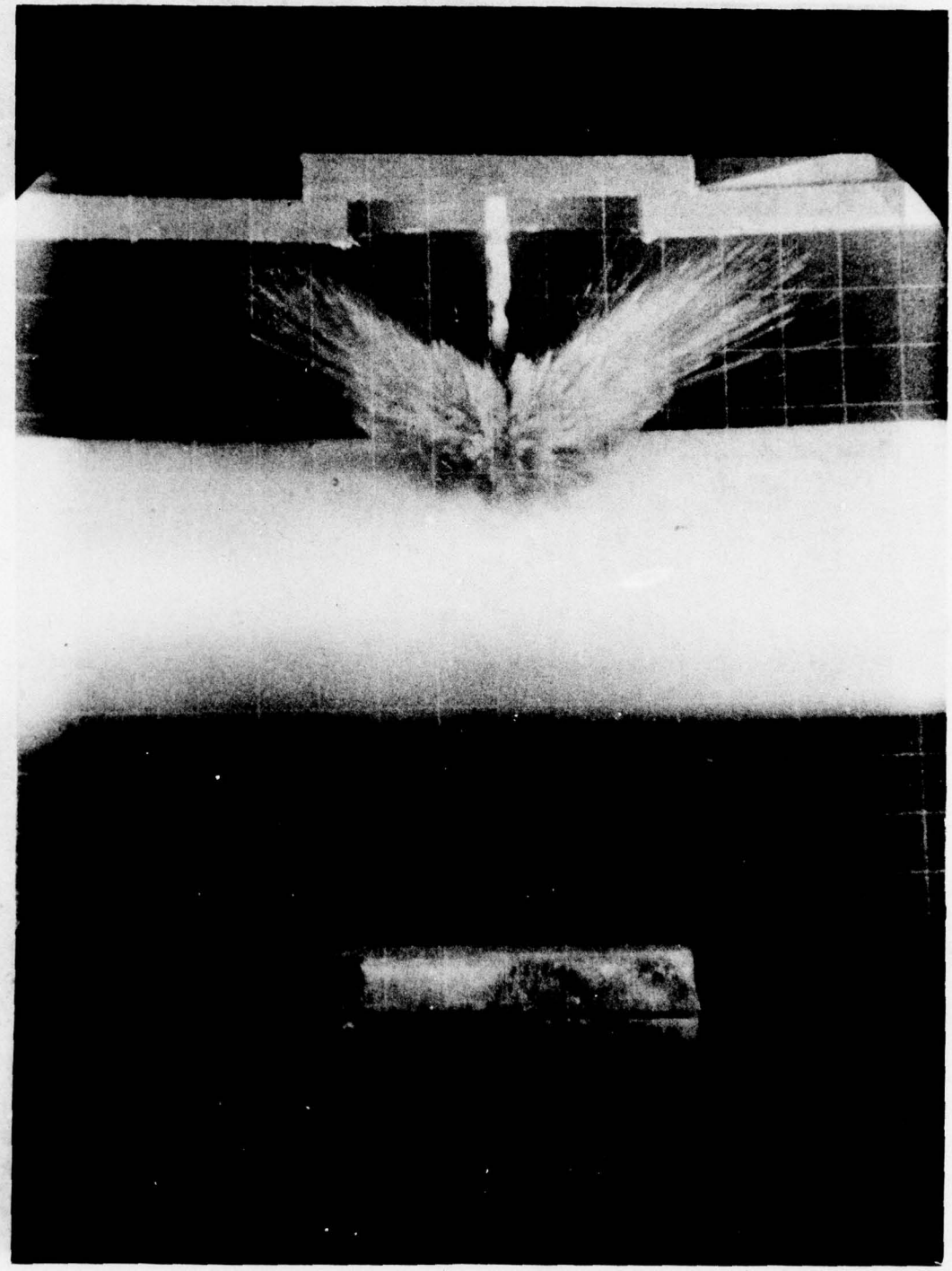

Figure A.9 Observation at 36 μs after impact

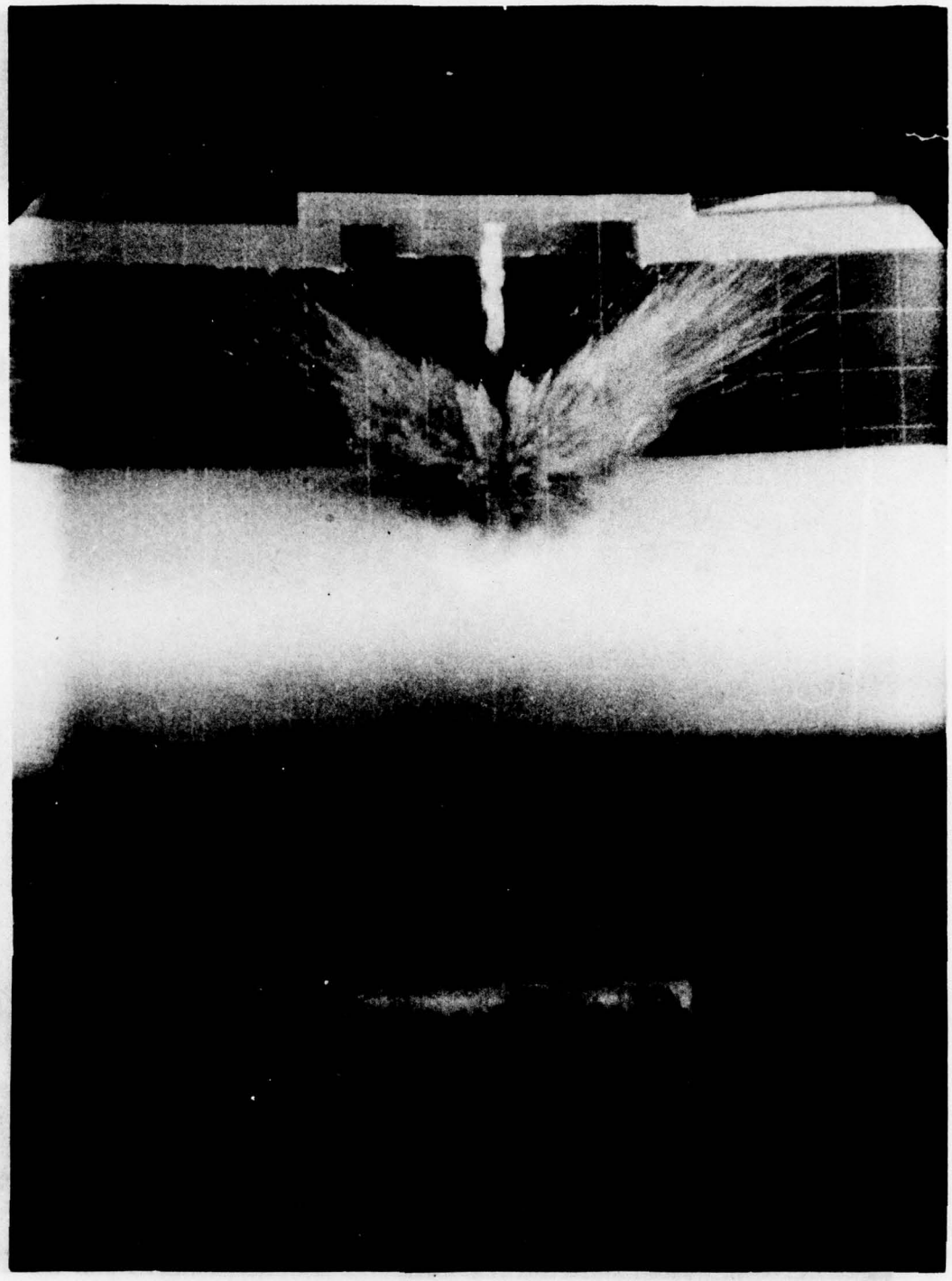

Figure A.10 Observation at 40 us after impact

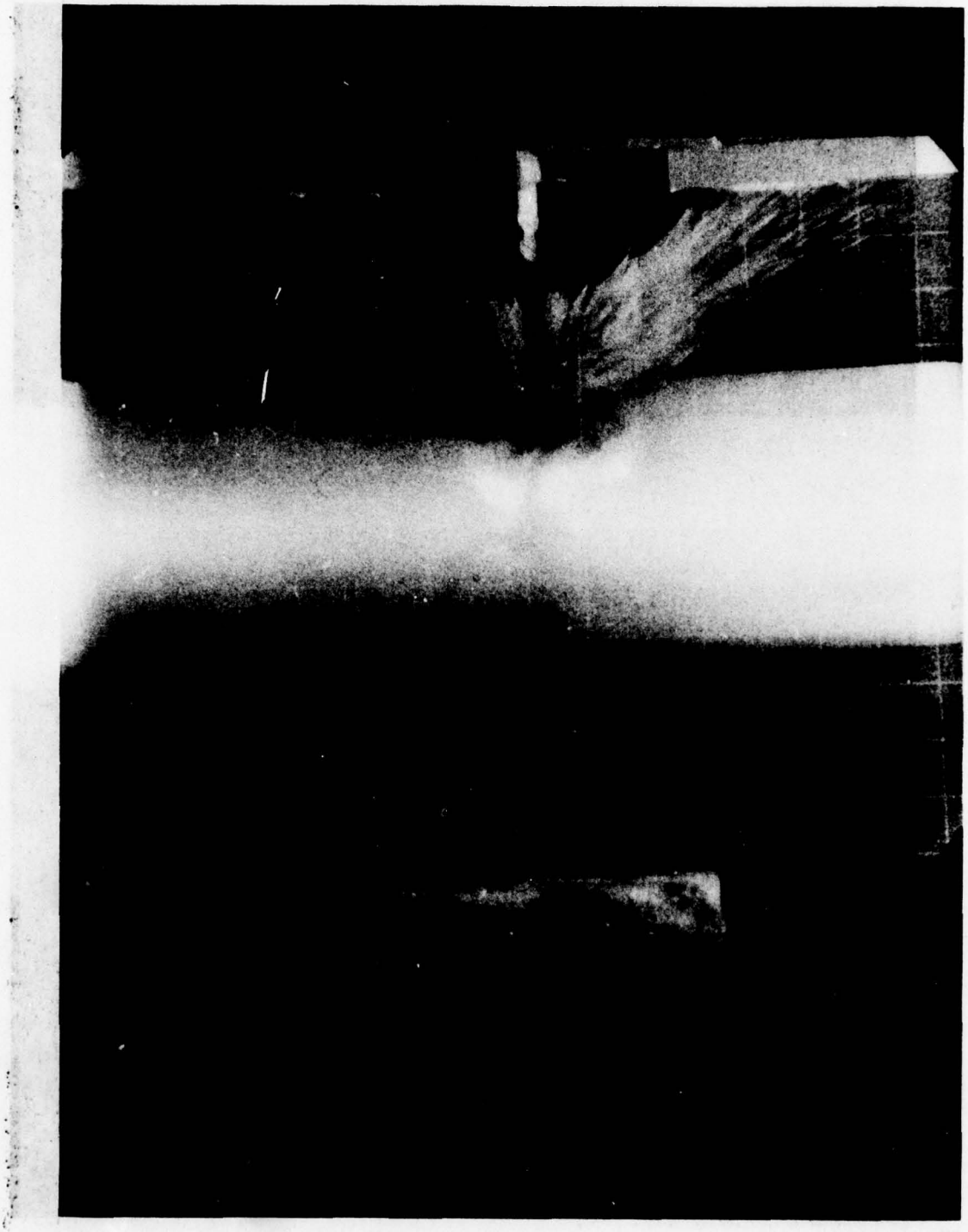

Figure A.11 Observation at 44 μs after impact

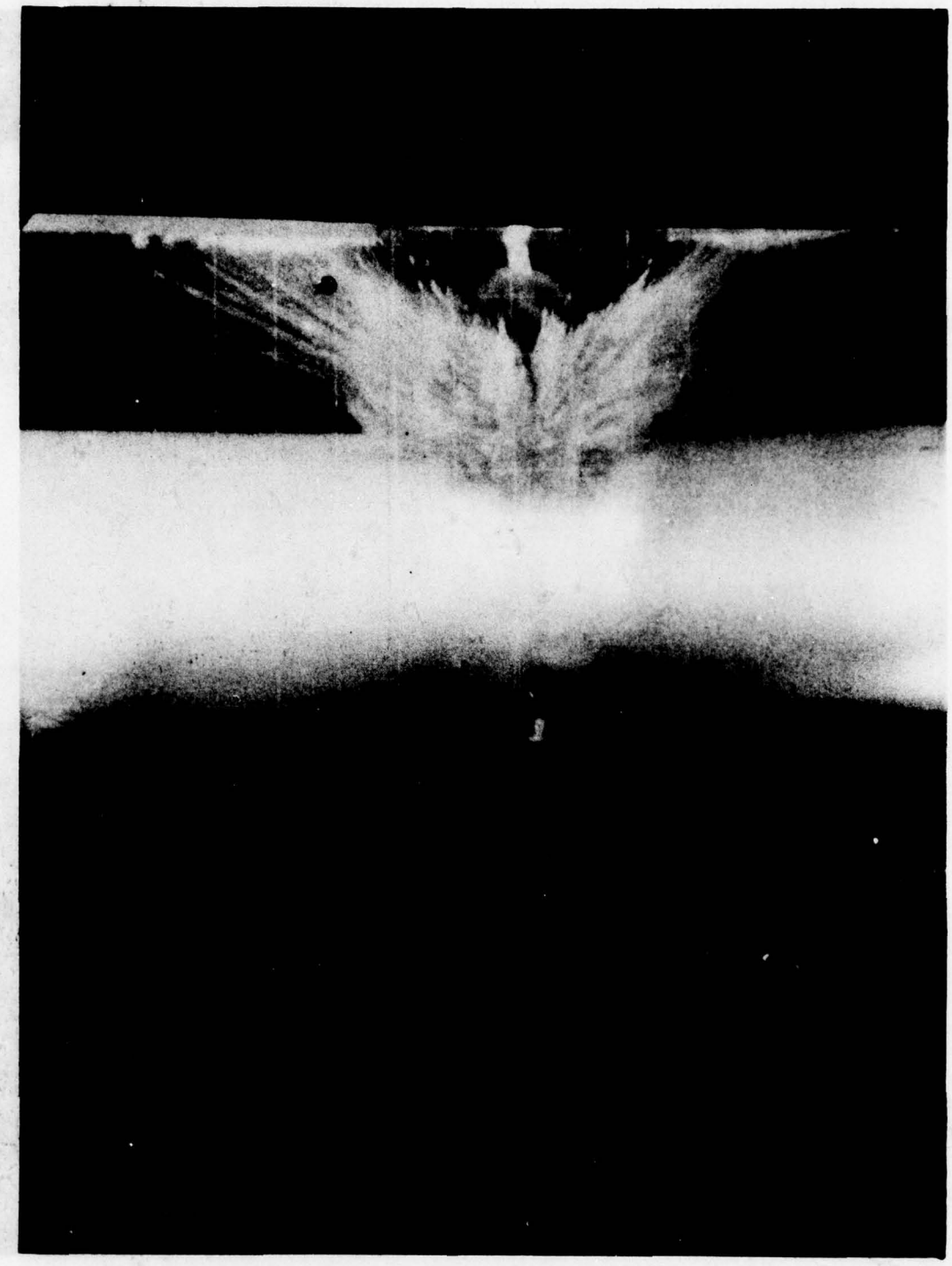

Figure A.12 Observation at 56 μs after impact

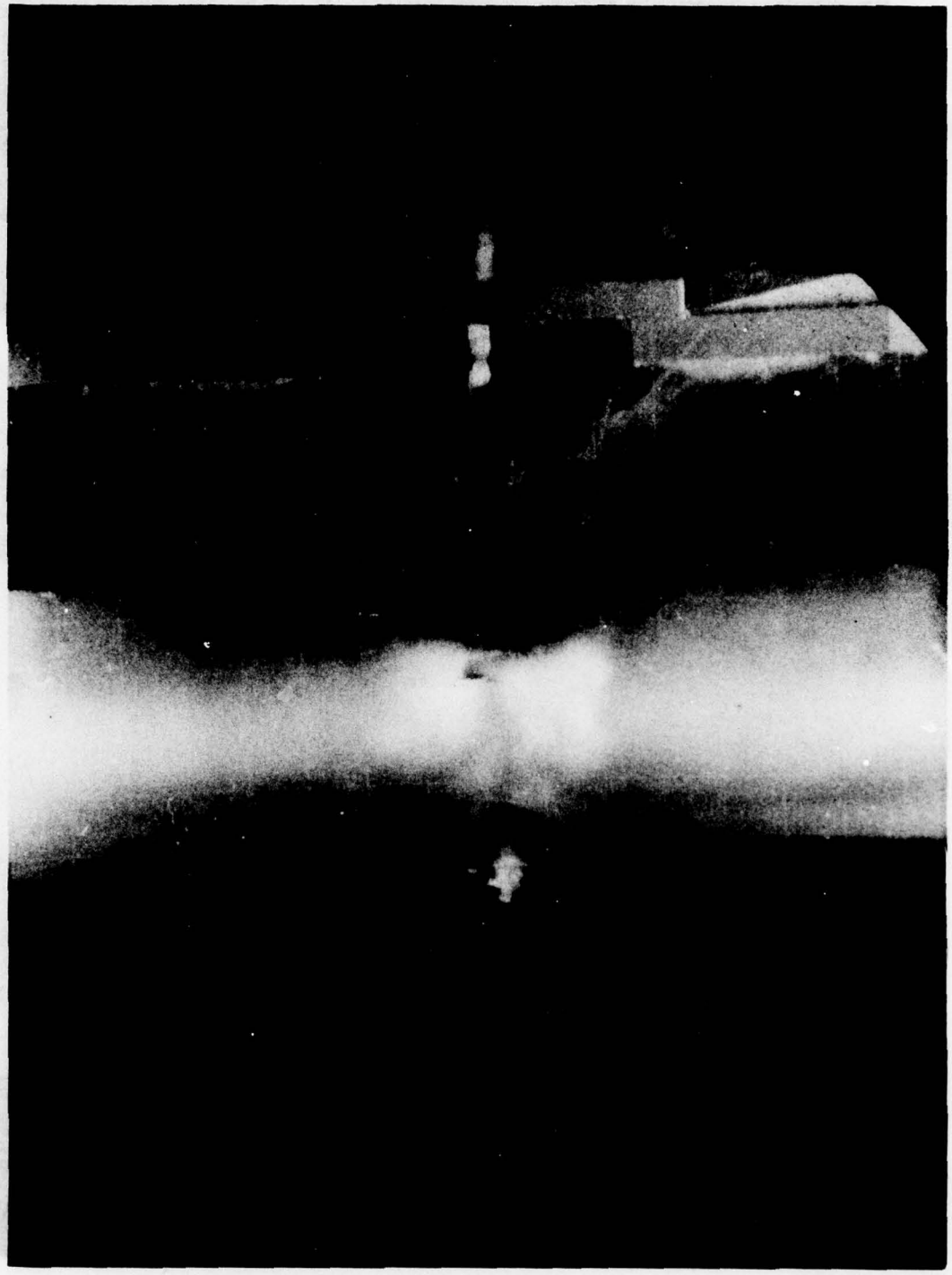

Figure A.13 Observation at 60 μs after impact

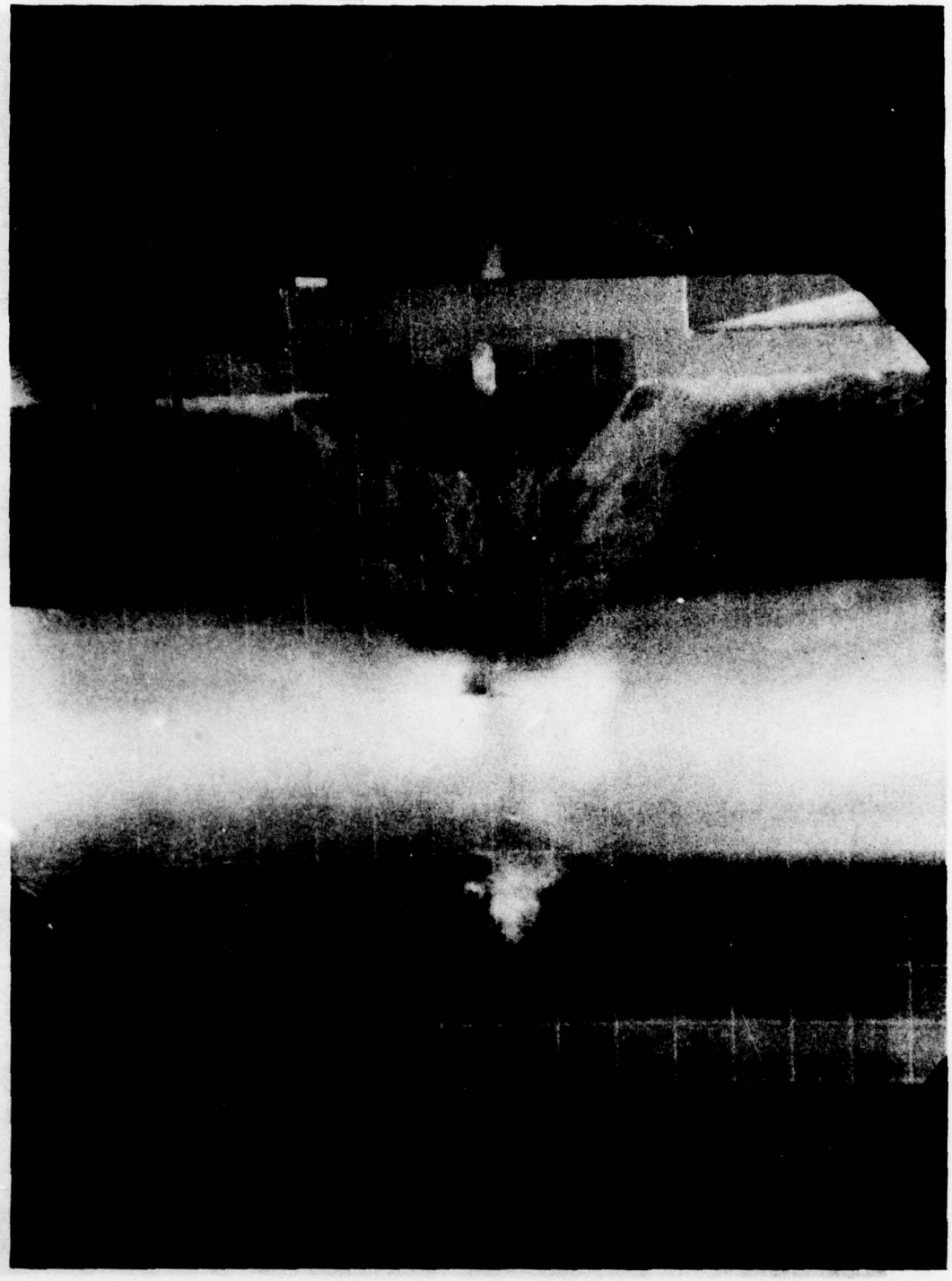

Figure A.14 Observation at 64 μs after impact

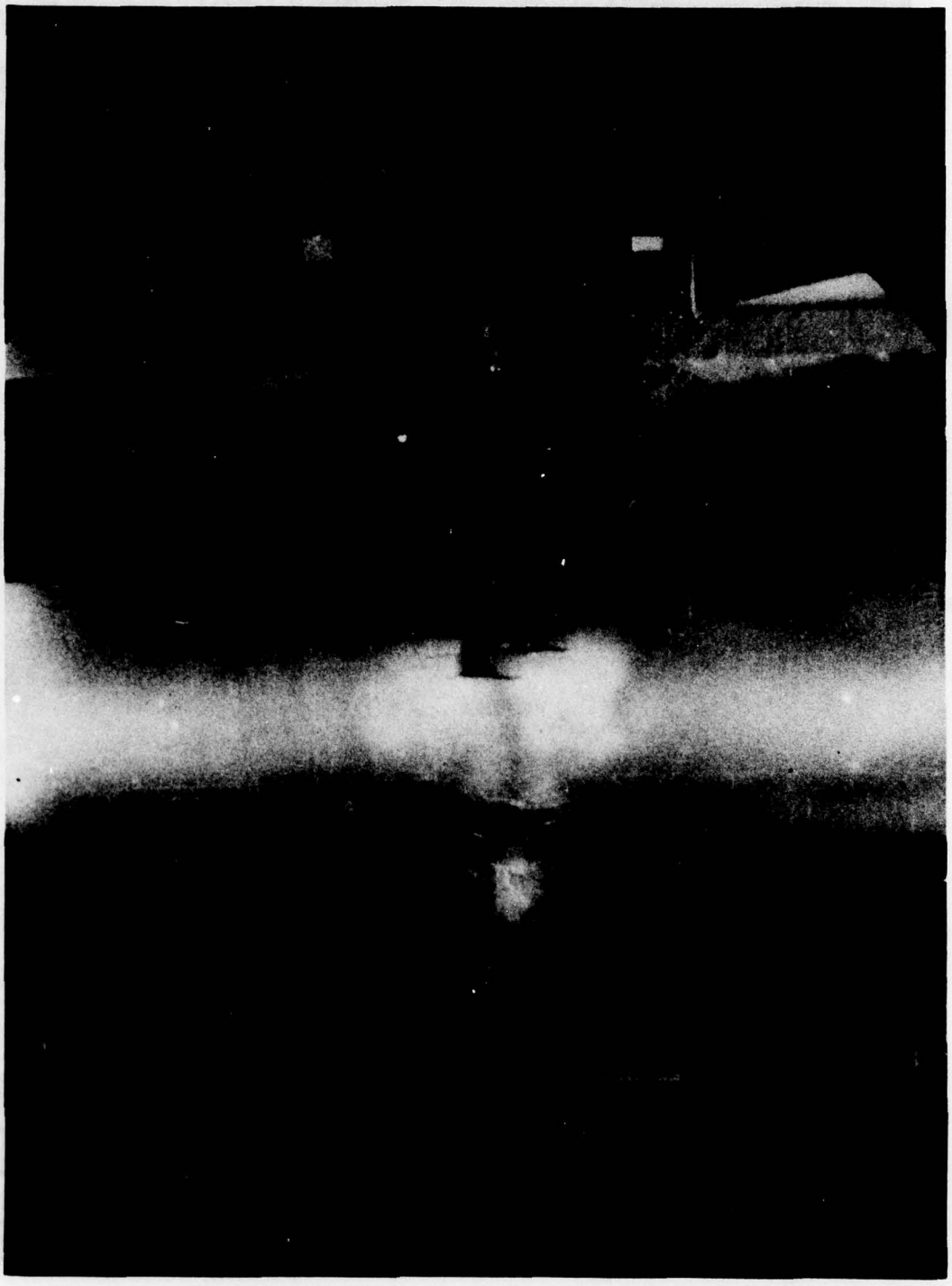

Figure A.15 Observation at 68 μs after impact

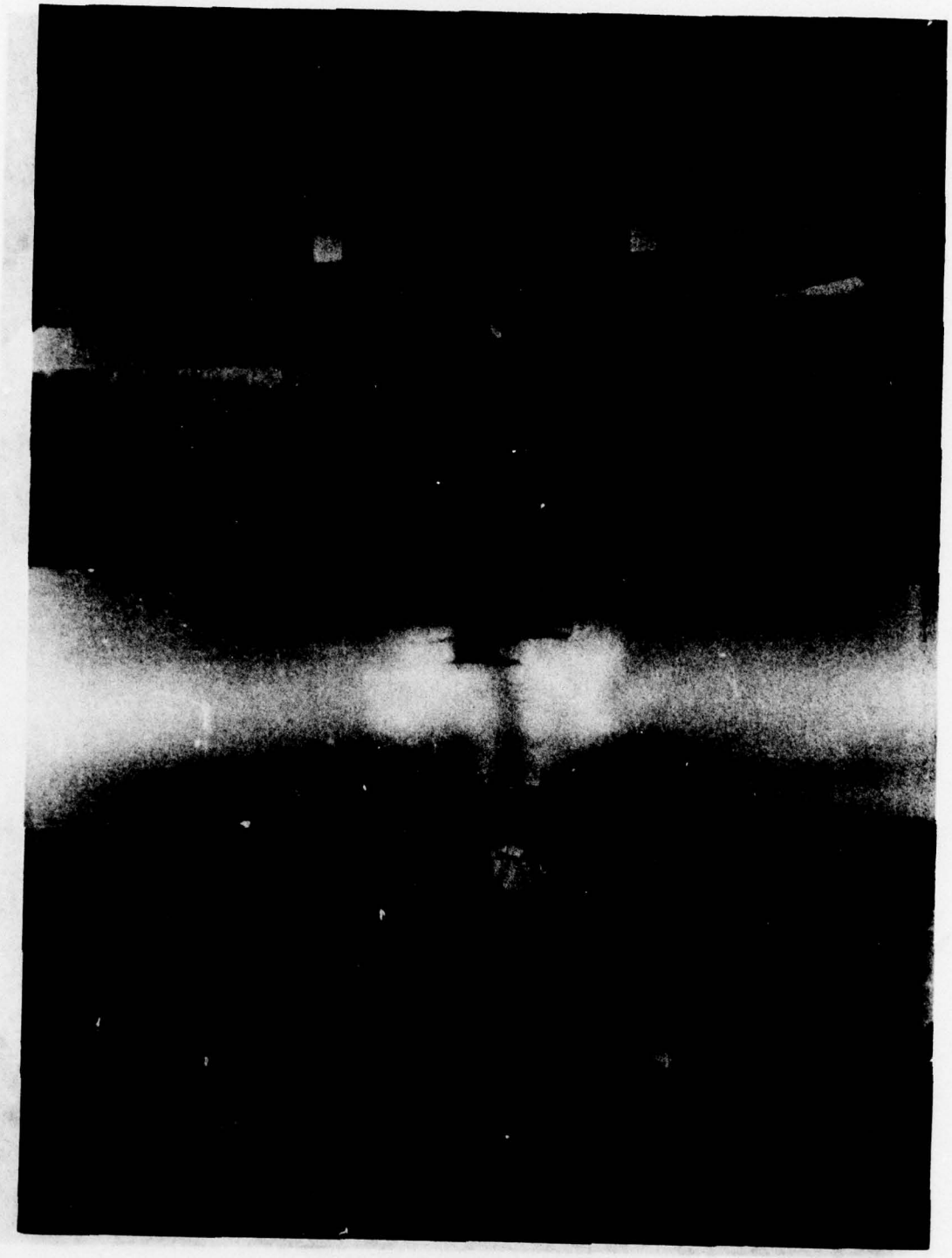

Figure A.16 Observation at 72 μs after impact

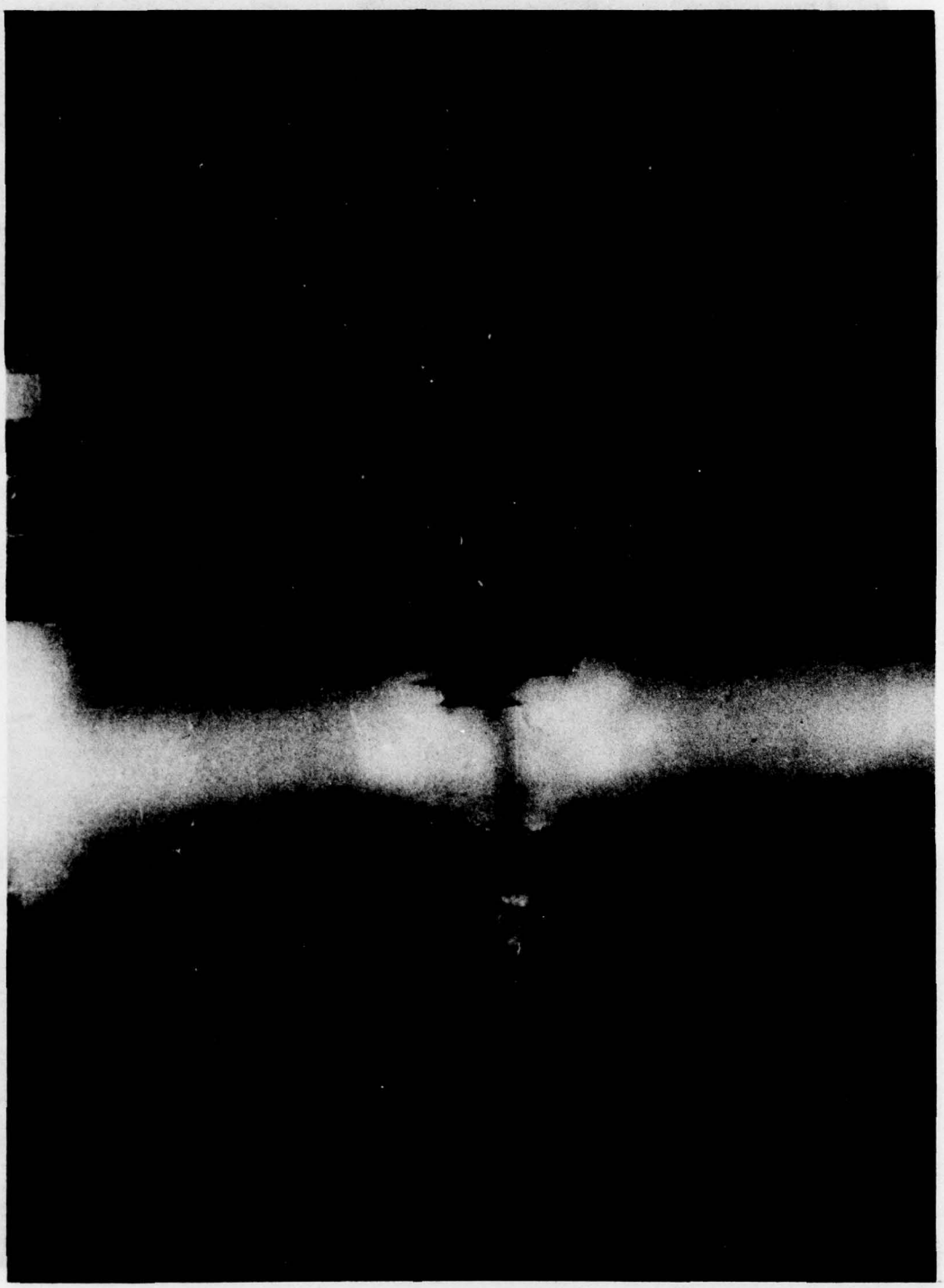

Figure A.17 Observation at 76 μs after impact

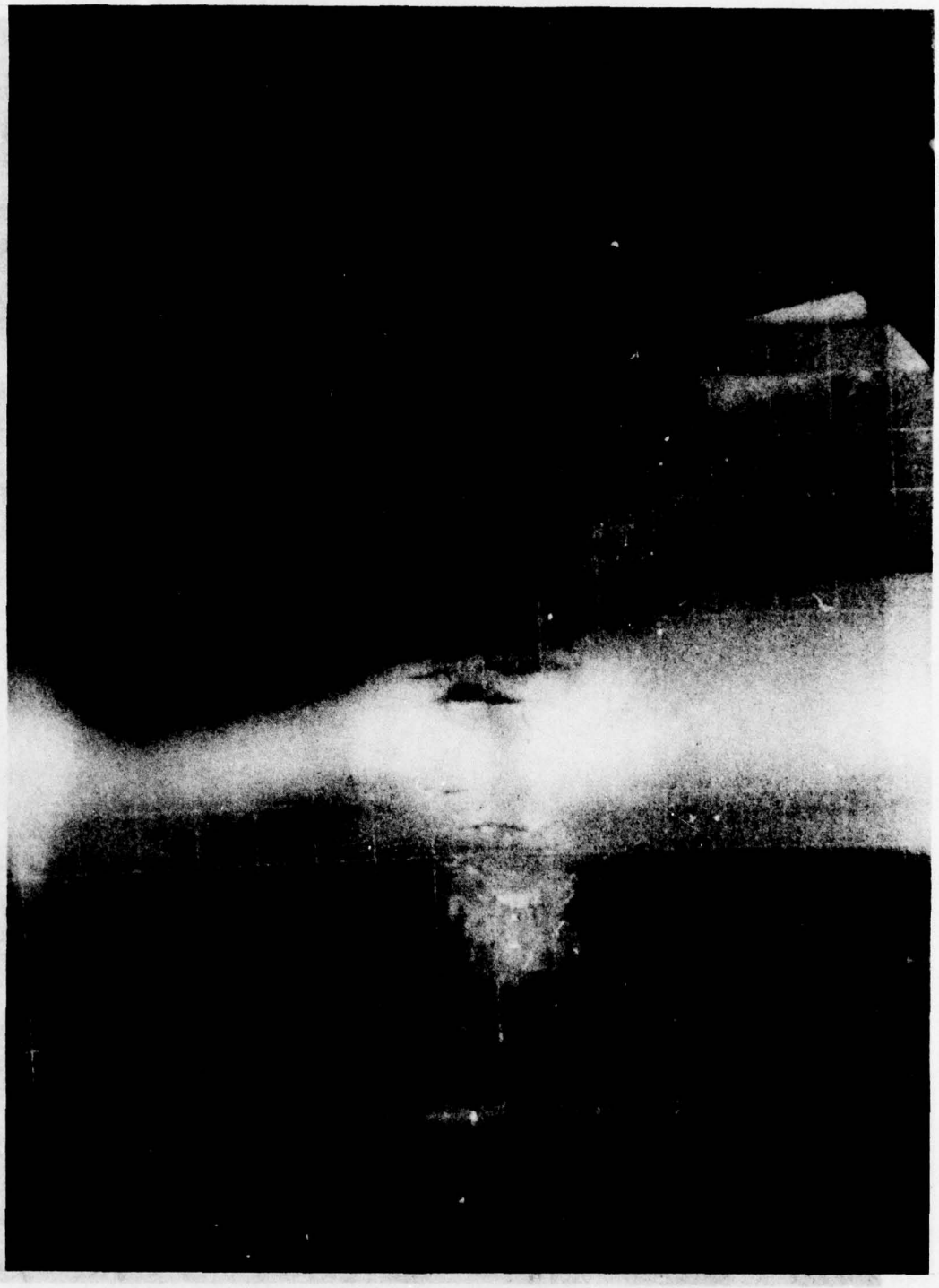

Figure A.18 Observation at 80 μs after impact

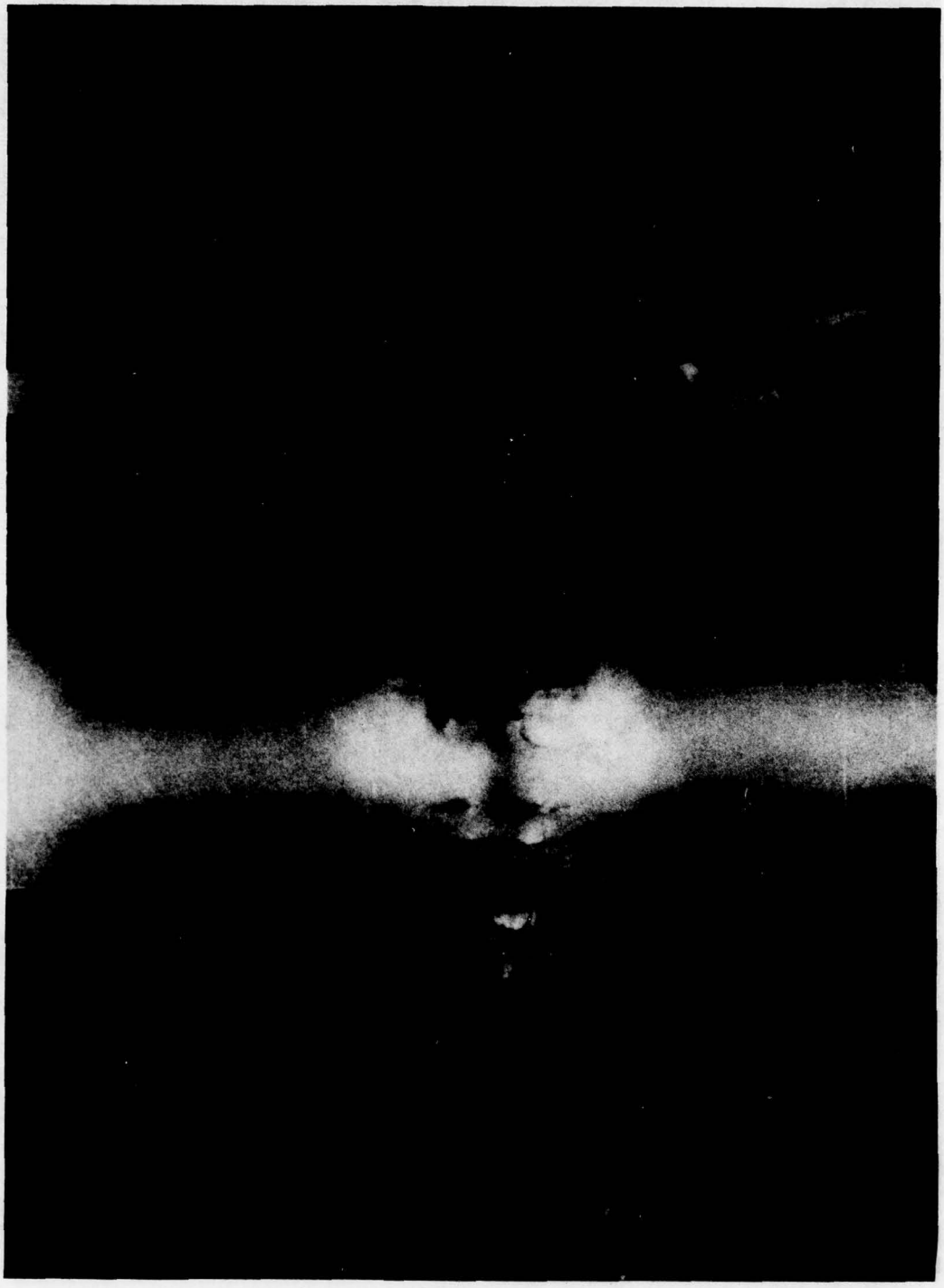

Figure A.19 Observation at 84 μs after impact

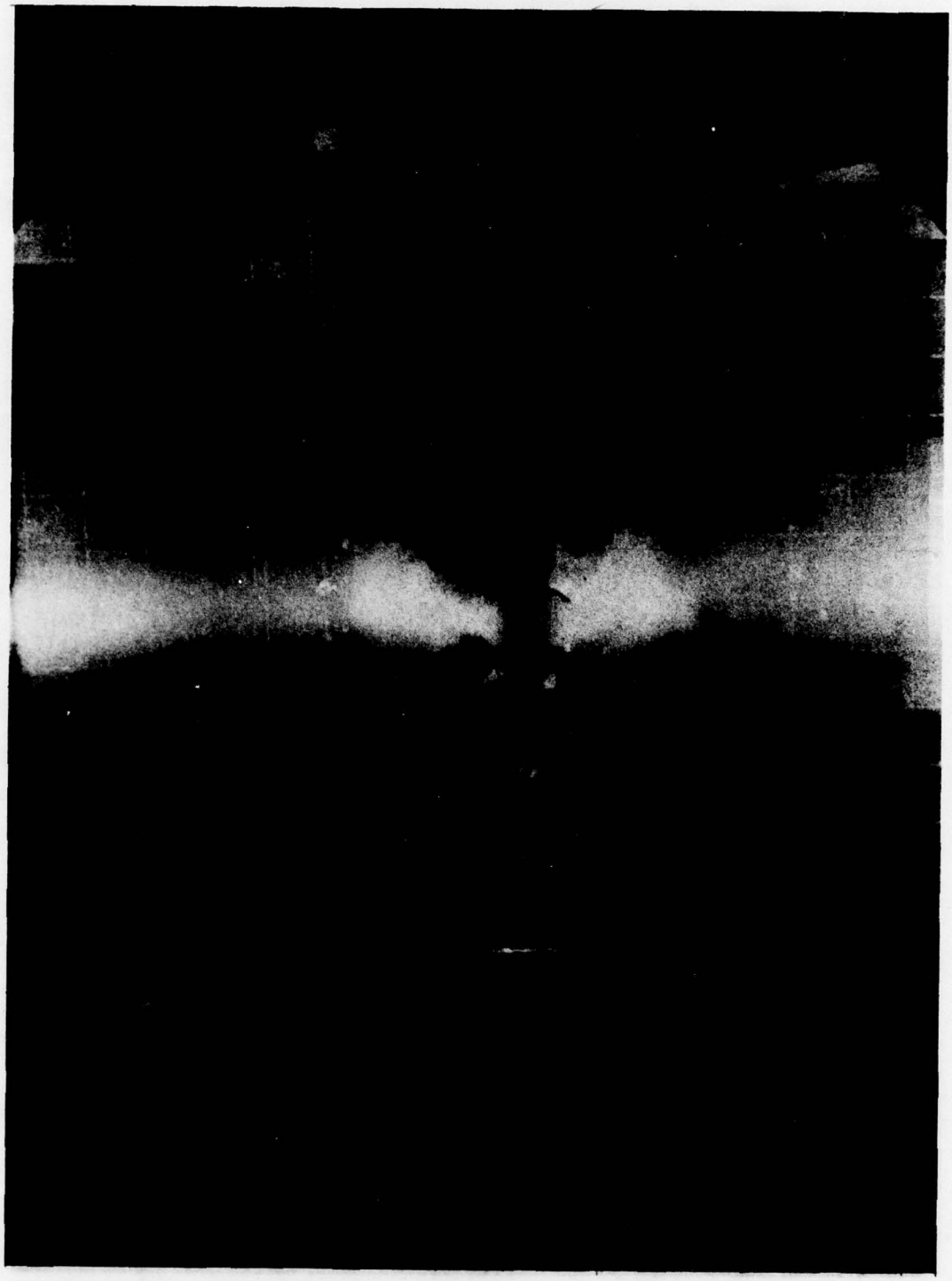

Figure A.20 Observation at 92 μs after impact

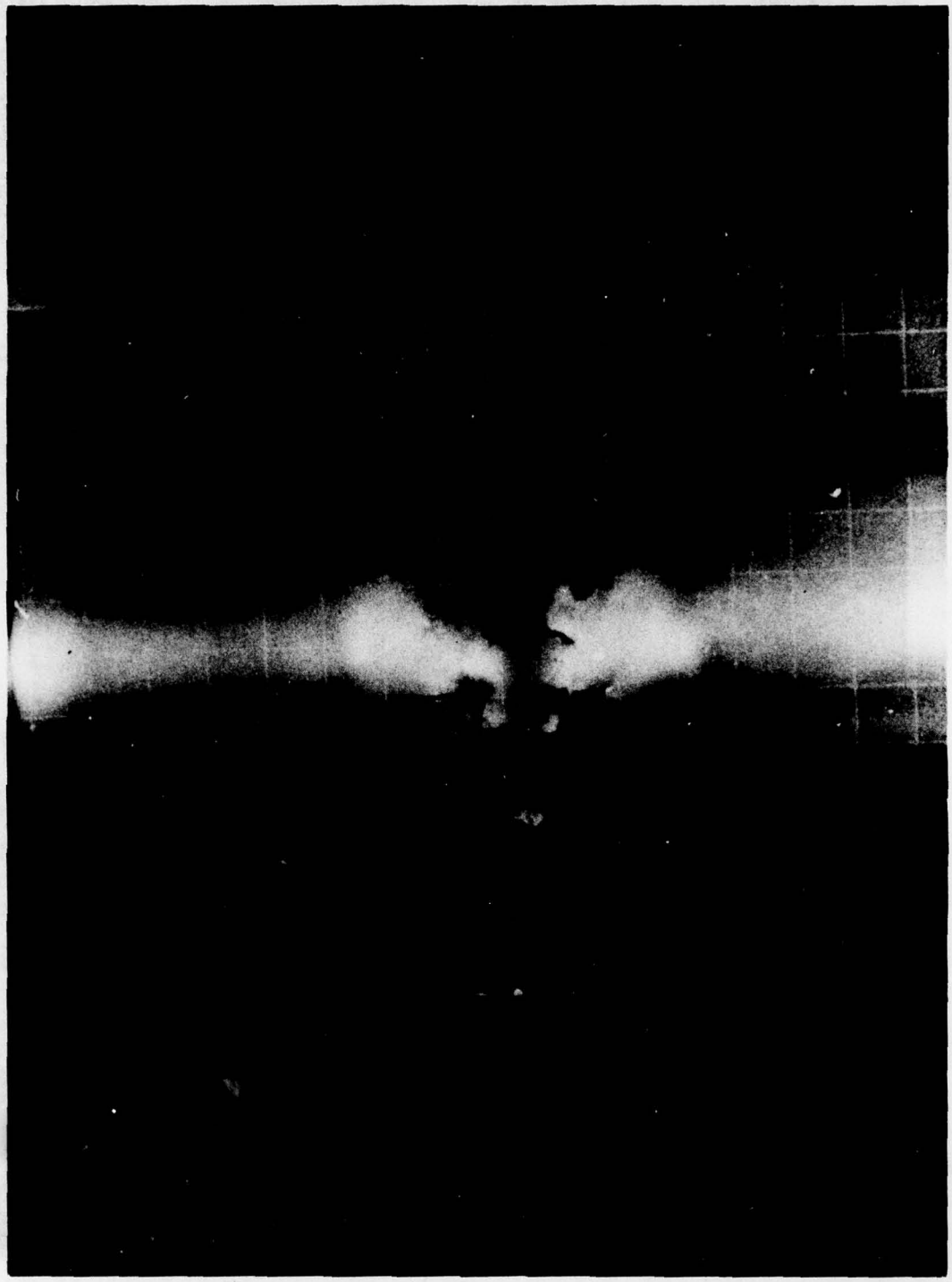

Figure A.21 Observation at 96 μs after impact

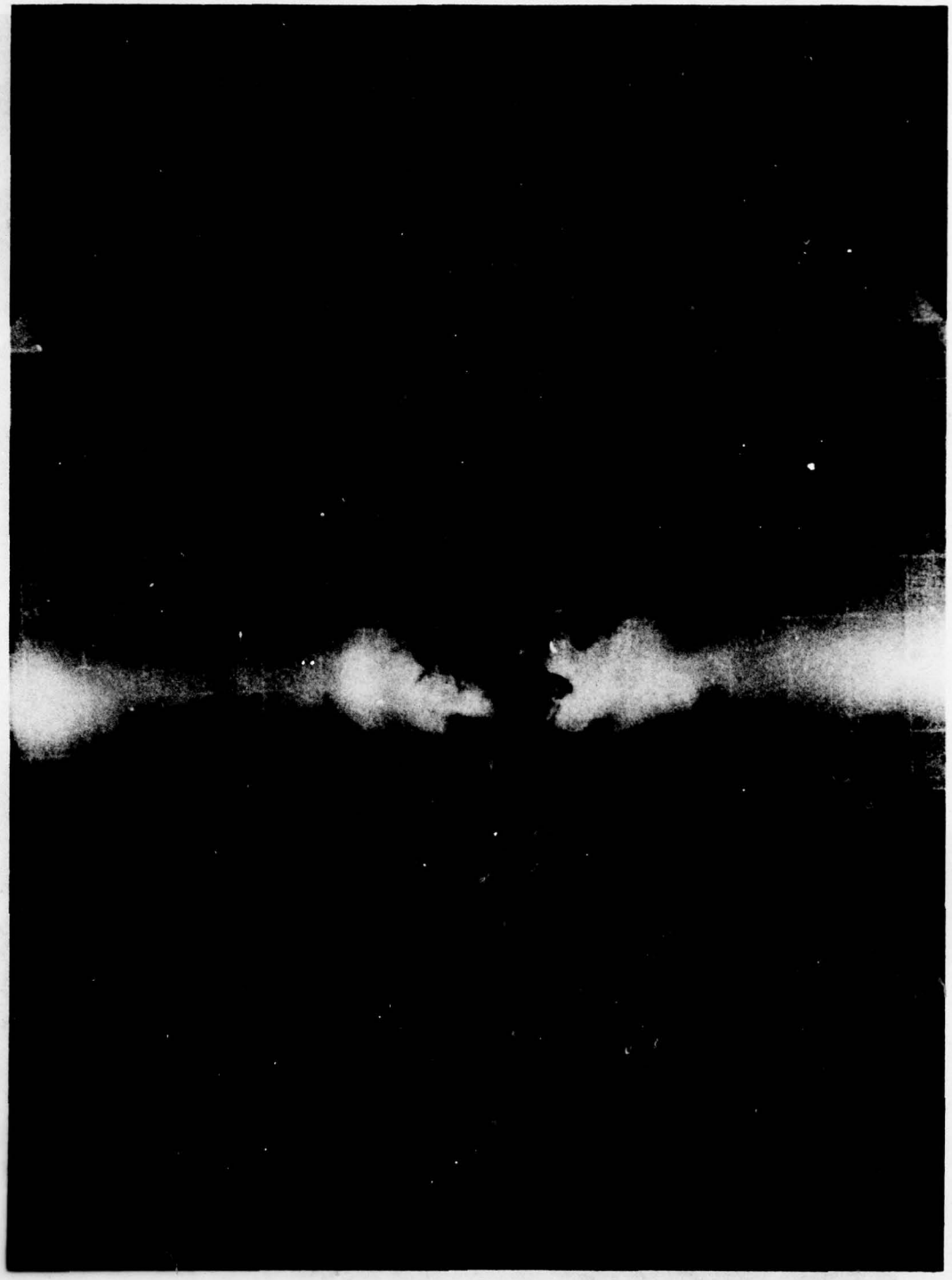

Figure A.22 Observation at 100 μs after impact

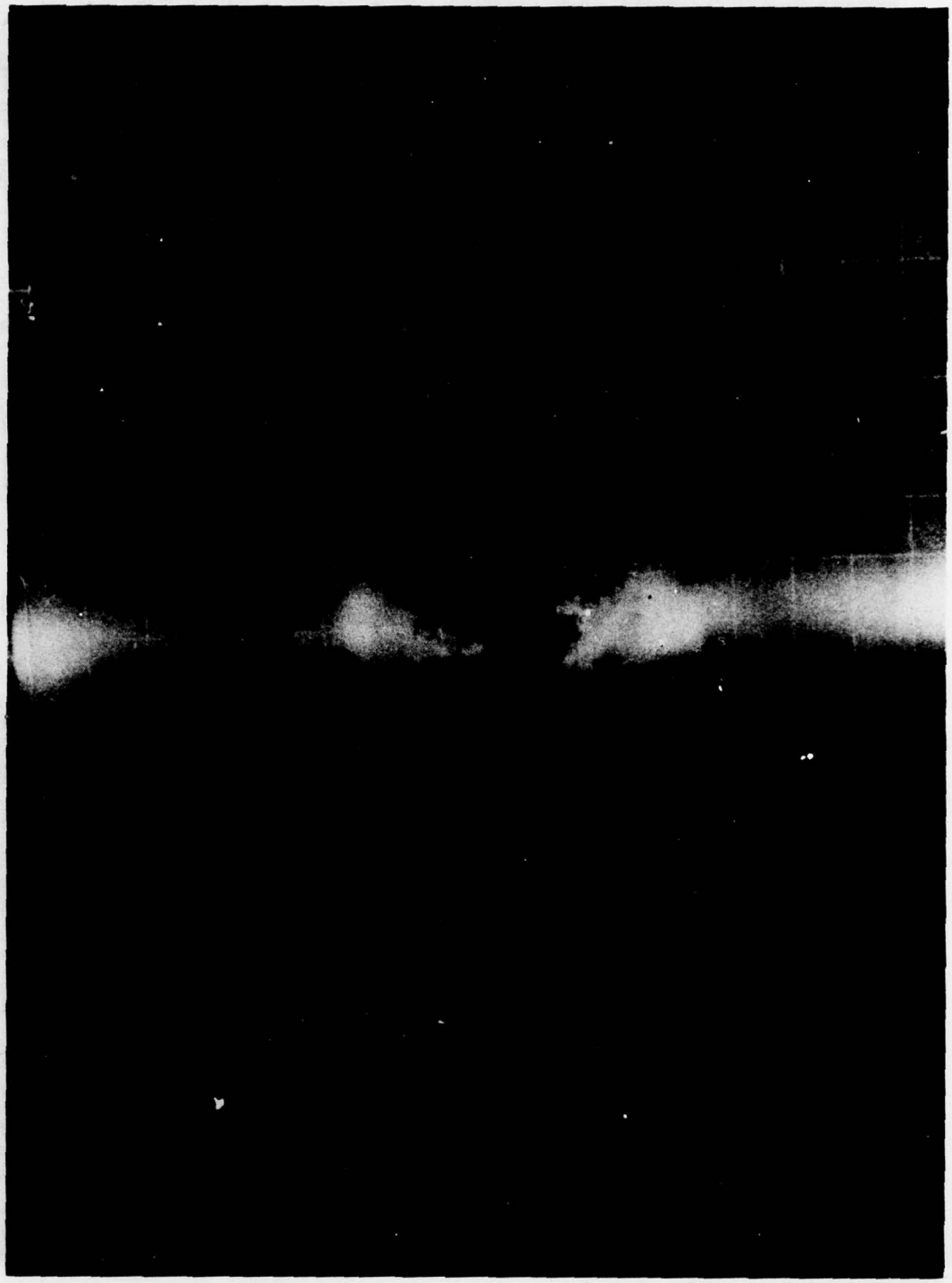

Figure A.23 Observation at 104 μs after impact

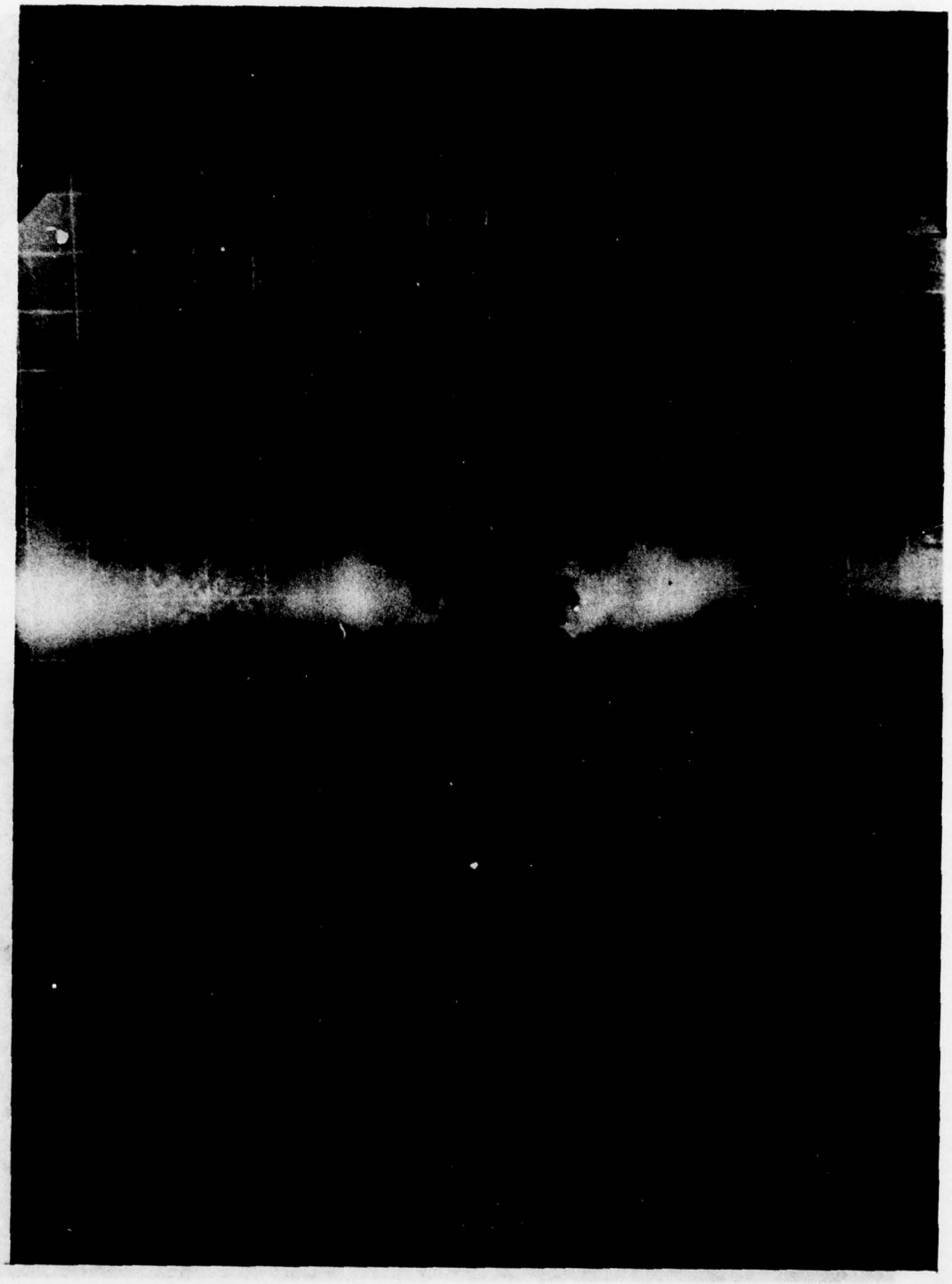

Figure A.24 Observation at 108 μs after impact

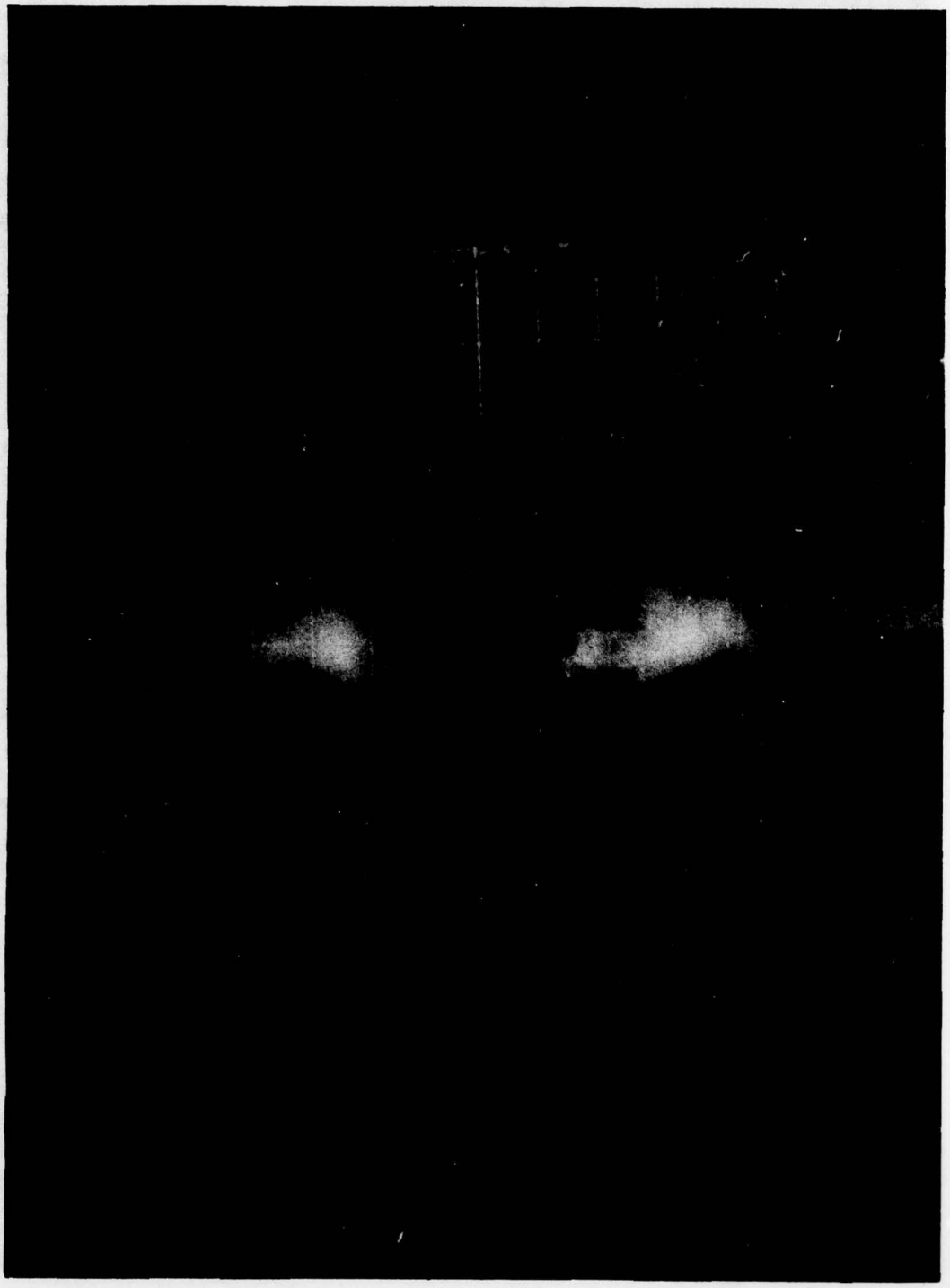

Figure A.25 Observation at 116 μs after impact

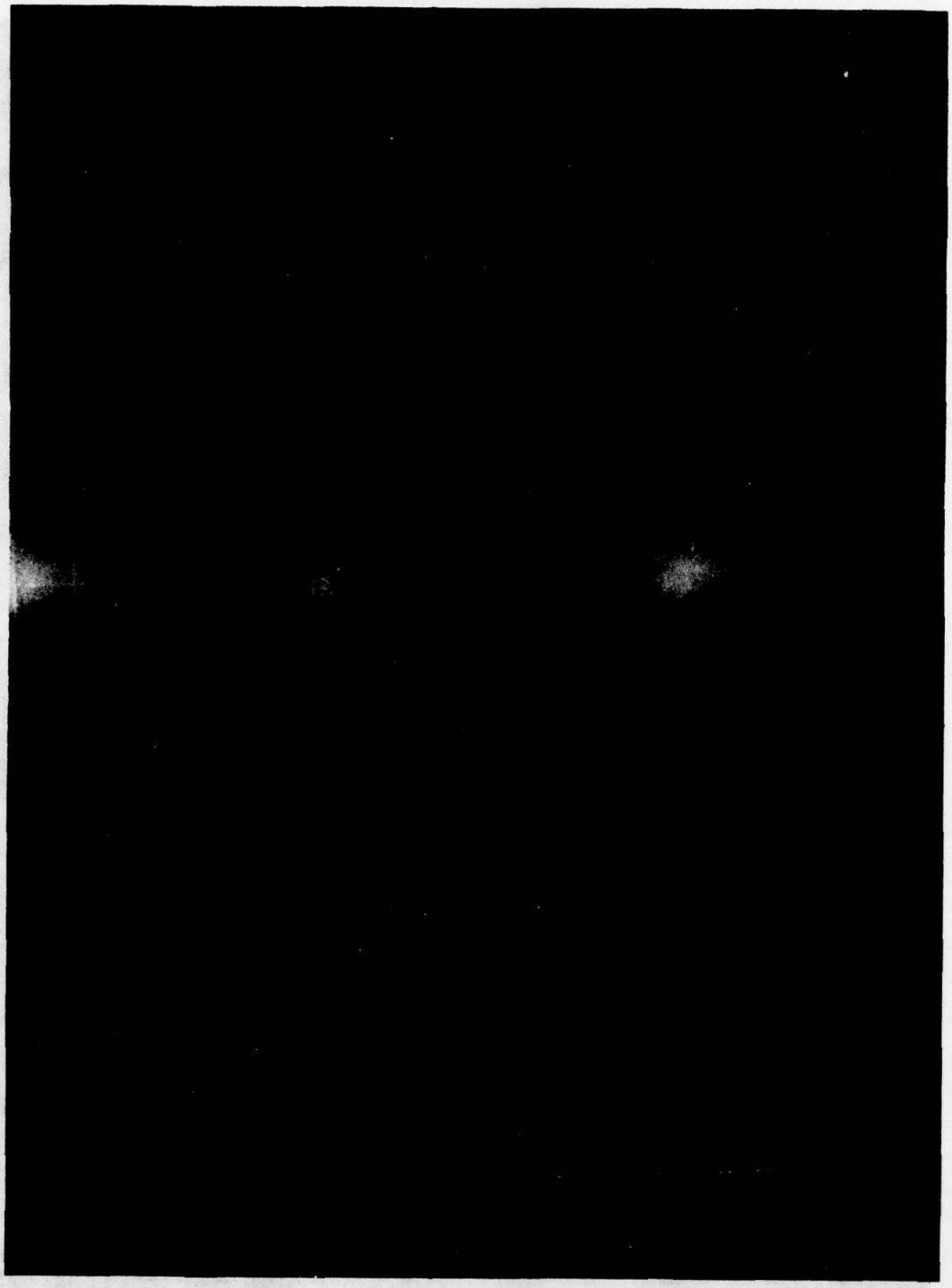

Figure A.26 Observation at 120 μs after impact

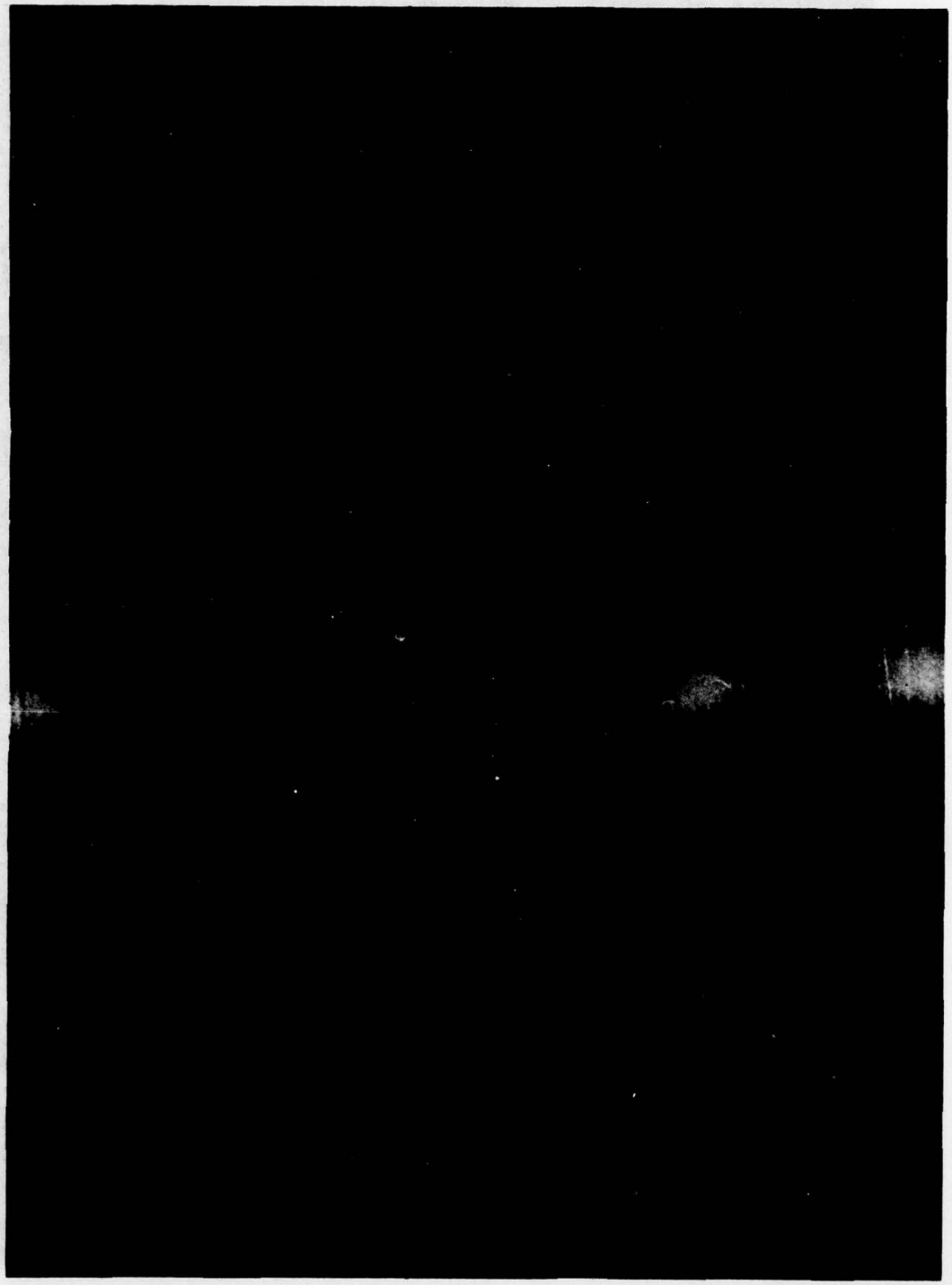

Figure A.27 Observation at 124 μs after impact

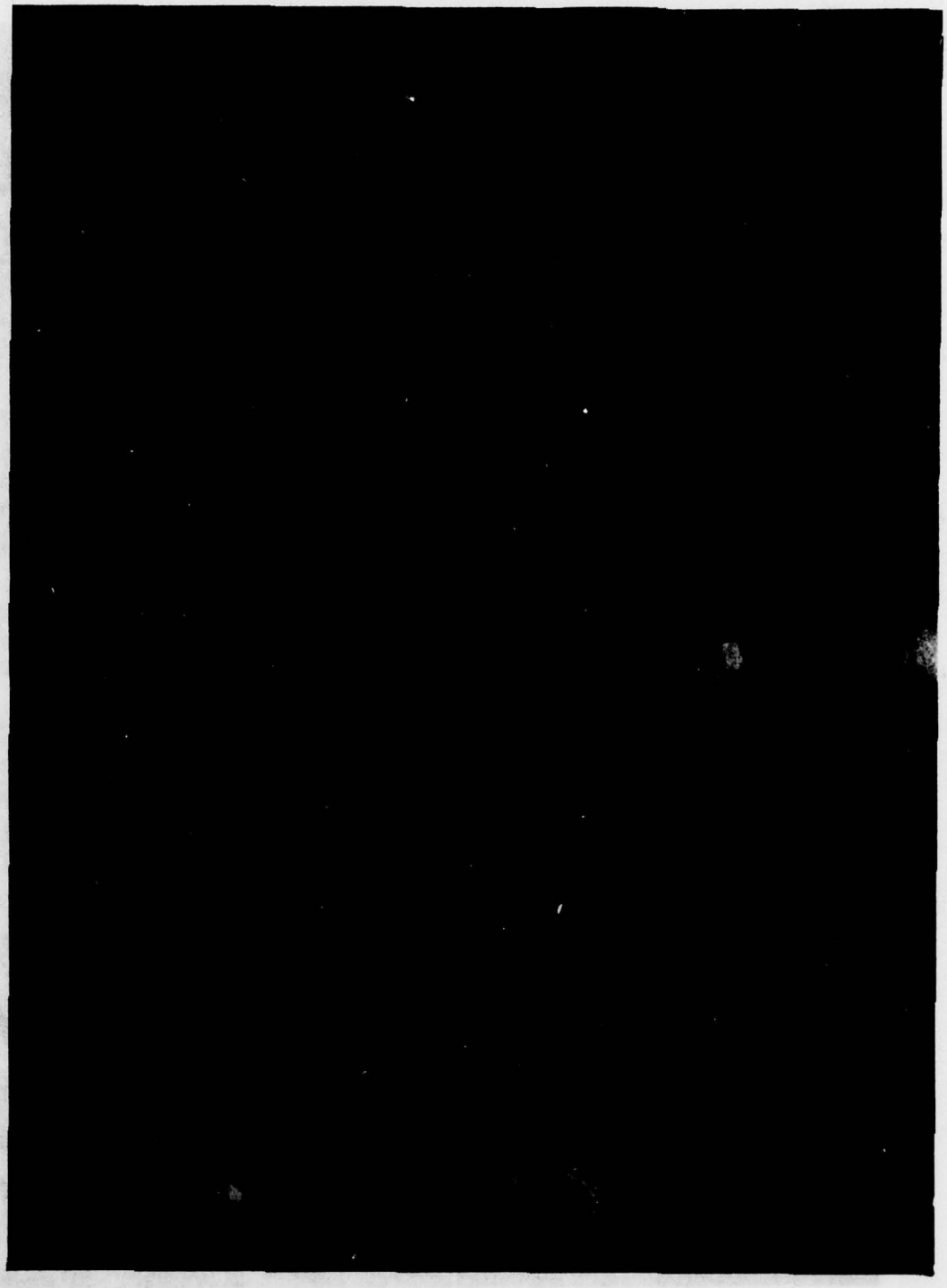

Figure A.28 Observation at 128 μs after impact

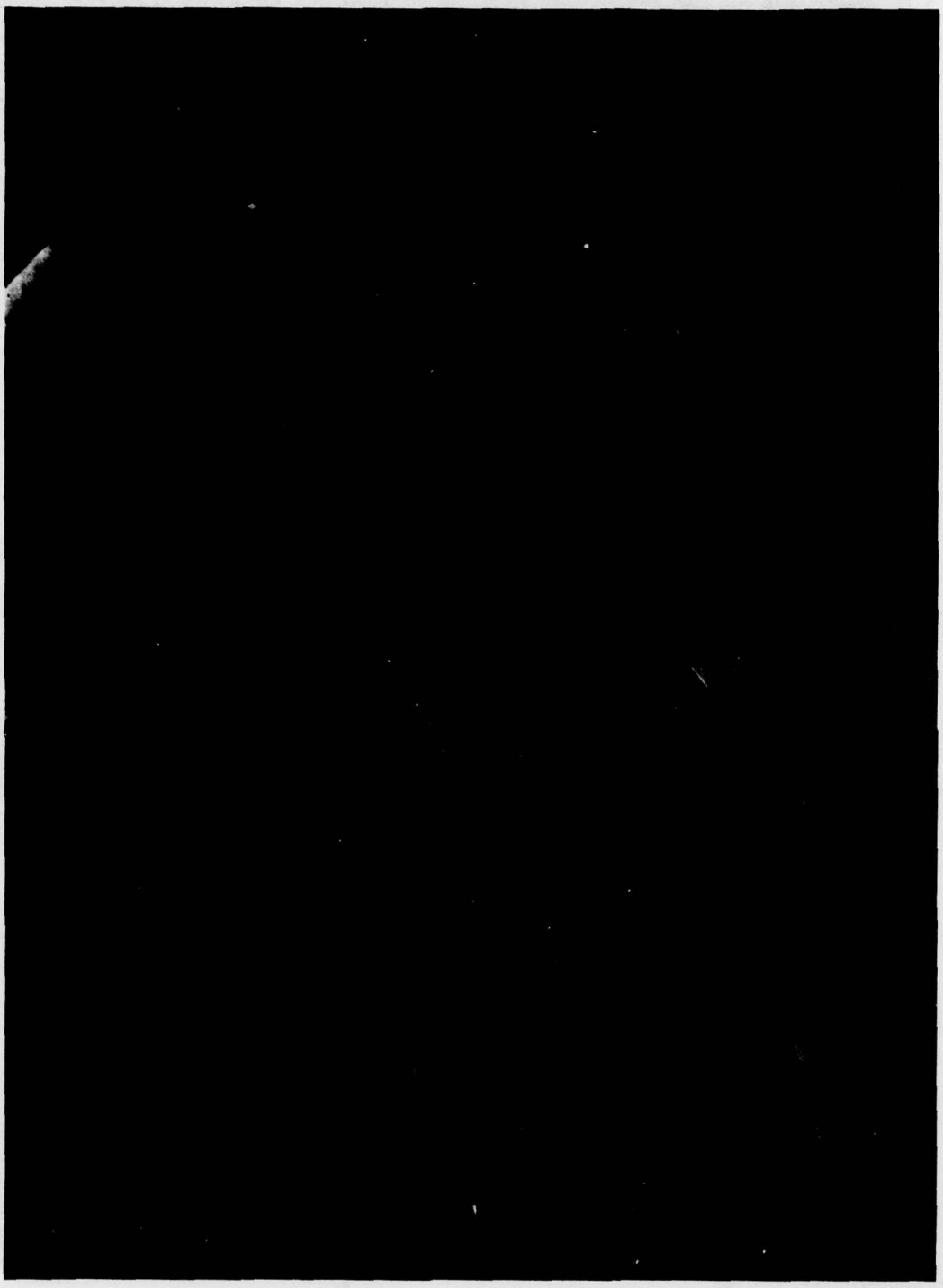

Figure A.29 Observation at 132 μs after impact

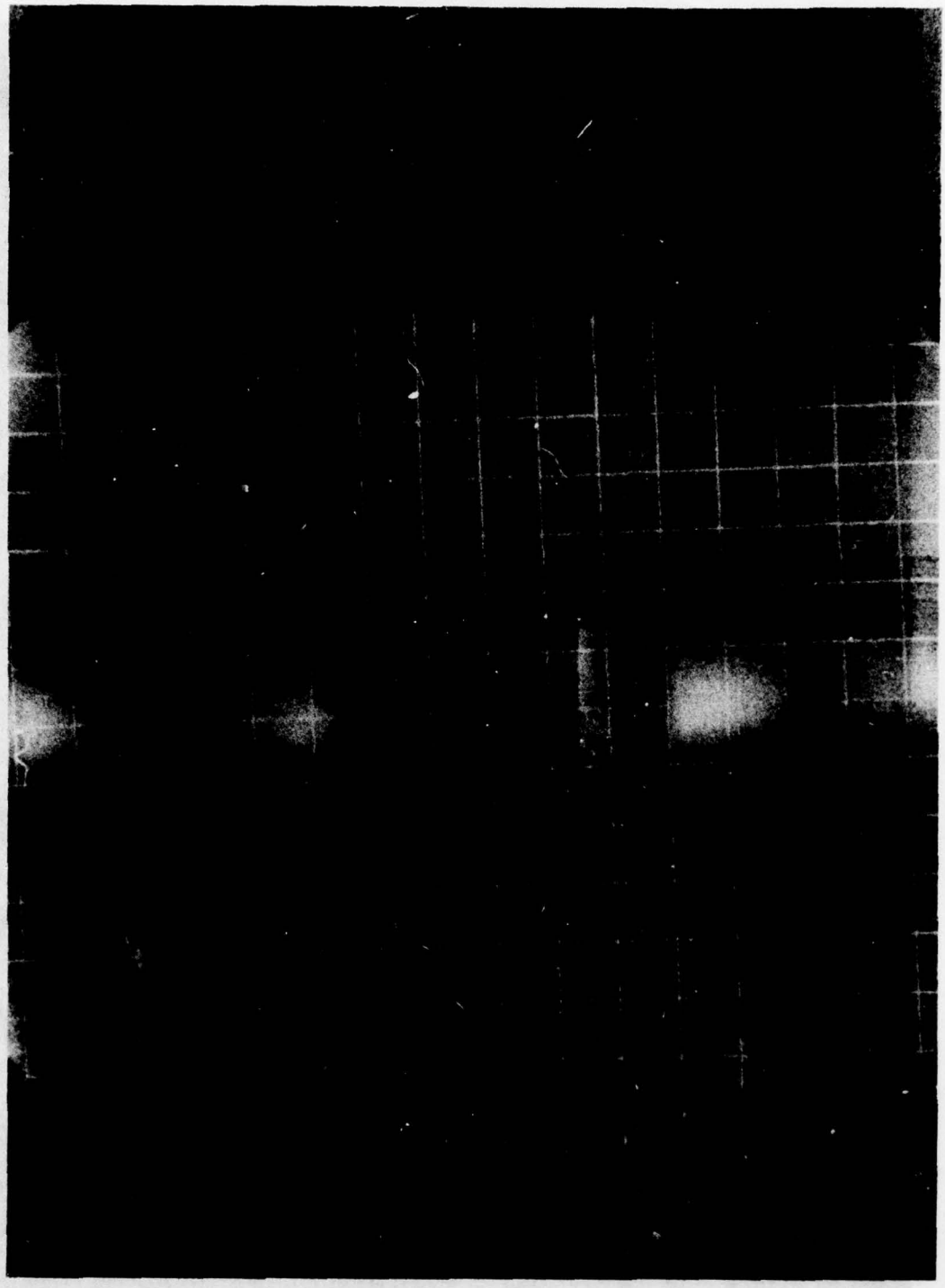

Figure A.30 Observation at 136 μs after impact

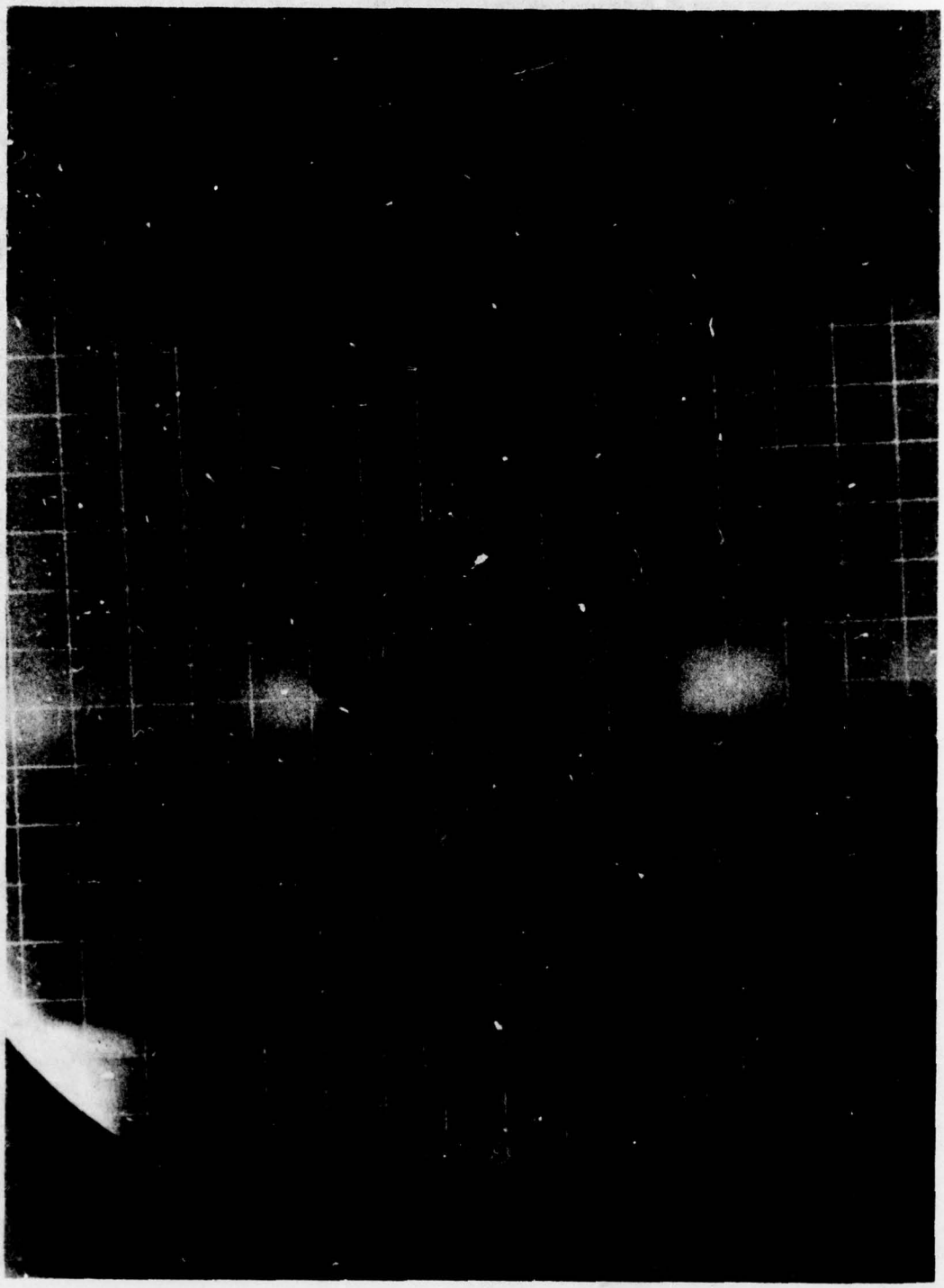

Figure A.31 Observation at 140 μs after impact

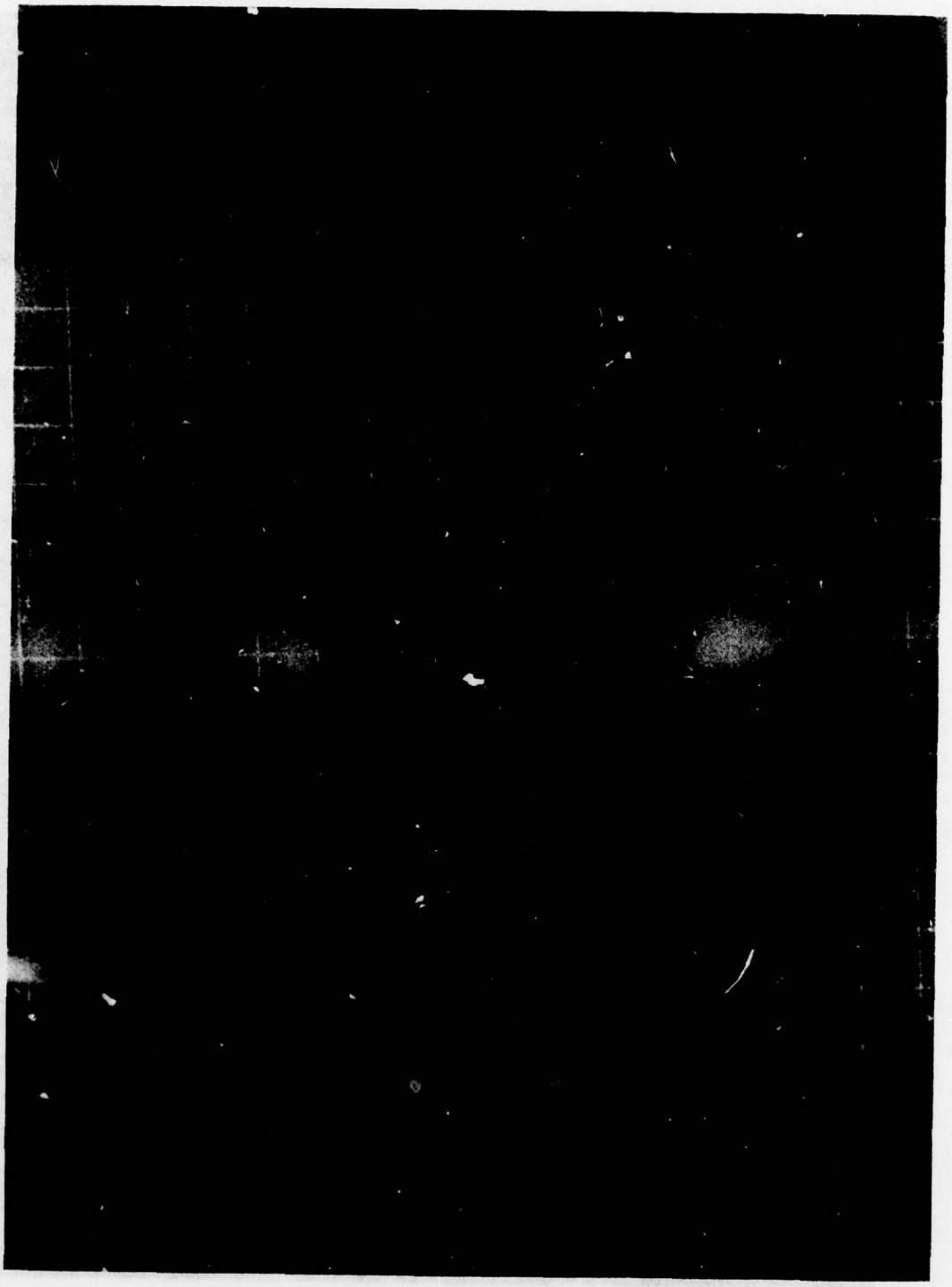

Figure A.32 Observation at 144 μs after impact

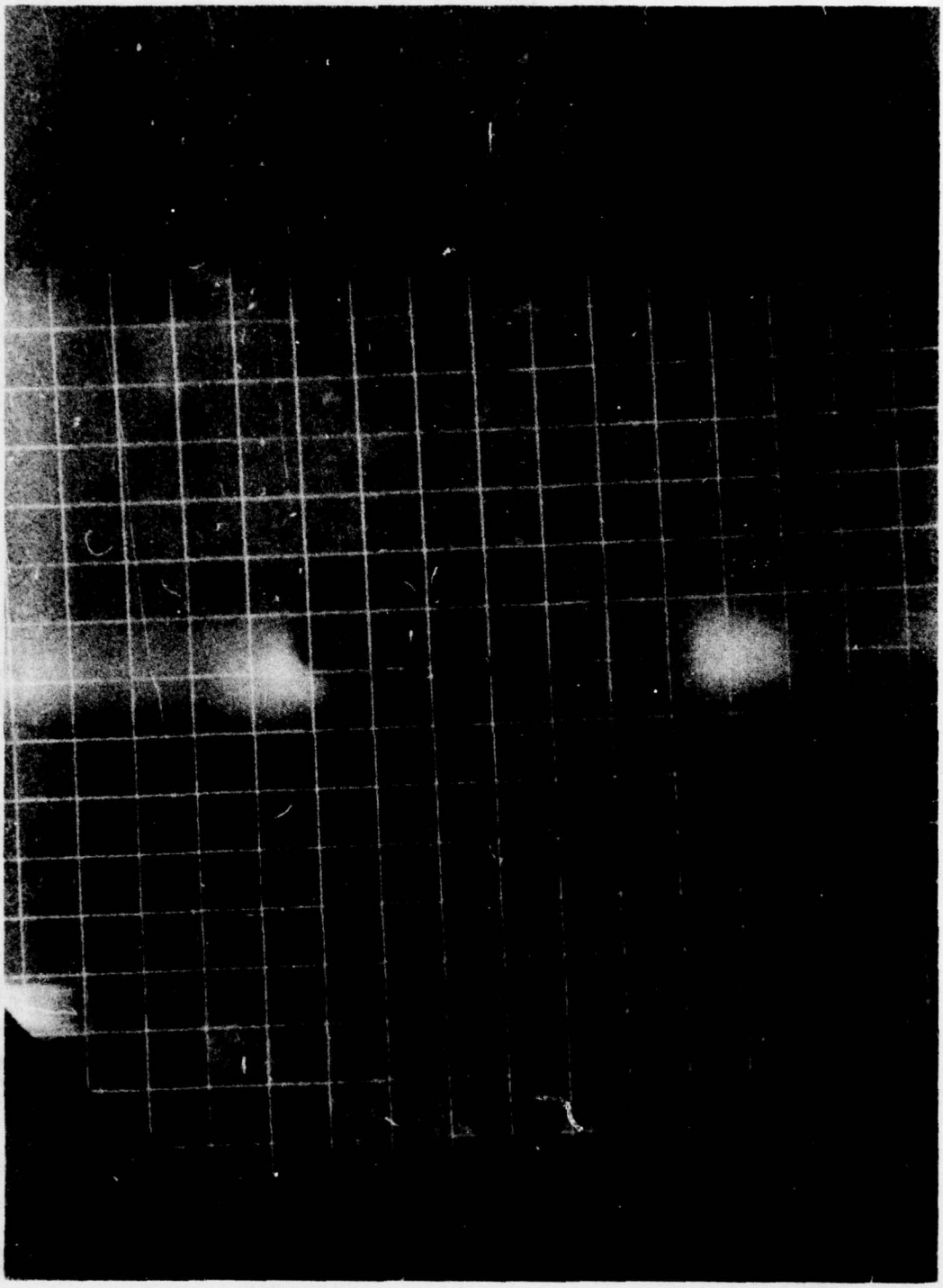

Figure A.33 Observation at 148 μs after impact

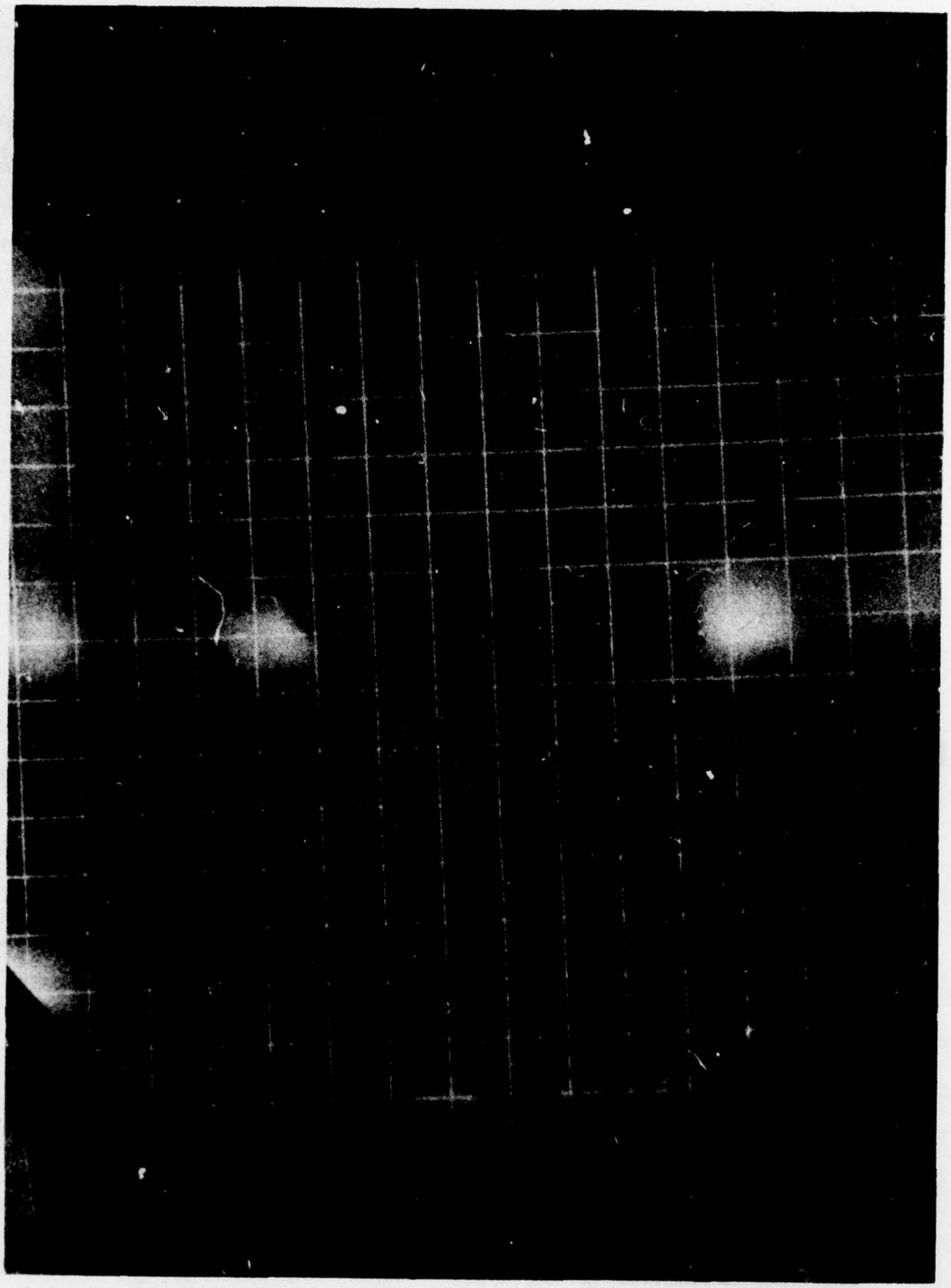

Figure A.34 Observation at 152 μs after impact

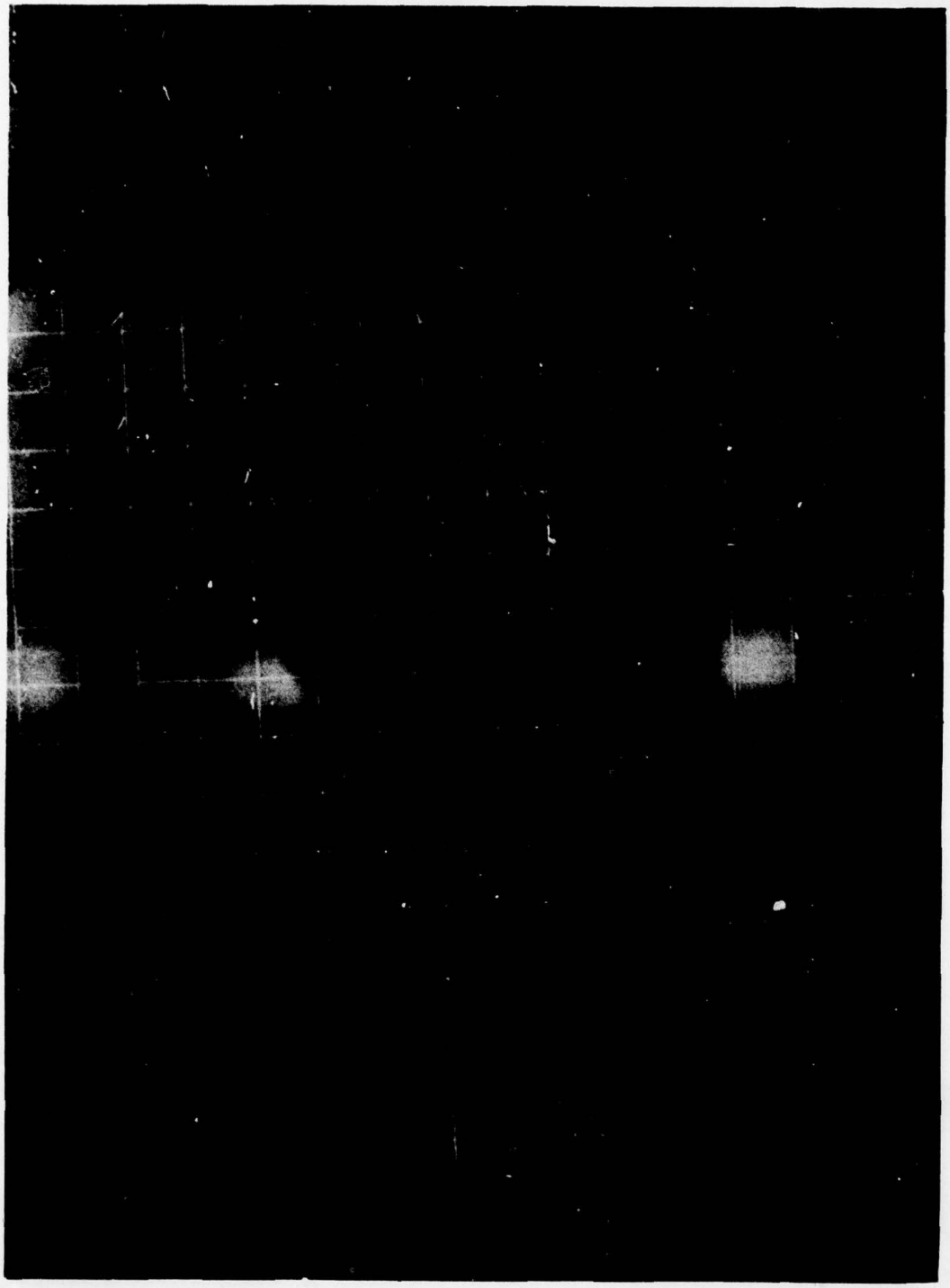

Figure A.35 Observation at 156 μs after impact

AD-A062 299 ARMY ARMAMENT RESEARCH AND DEVELOPMENT COMMAND ABERD--ETC F/G 19/1
OBSERVATIONS OF SHAPED-CHARGE JET/M30 PROPELLANT REACTIONS.(U)
SEP 78 J N MAJERUS, A B MERENDINO

UNCLASSIFIED ARBRL-TR-02108 SBIE-AD-E430 142 NL

2 OF 2
ADA
062299

END
DATE
FILMED
3 79
DDC

APPENDIX B

EXPERIMENTAL PROCEDURE FOR USING HYPERVELOCITY PARTICLES

The lead particle in a shaped-charge jet is essentially a non-stretching hypervelocity rod[17]. It is possible to isolate this particle, and any desired length of stretching jet-material following it, from the remaining material which normally exists in a jet. This isolation is accomplished by placing at the liner's base an acrylic plastic-inhibitor within the shaped-charge liner cavity, as illustrated in Figure B.1. The inhibitor prevents the basal portion of the liner from collapsing on itself and forming a jet. The amount of the basal portion of the liner that is inhibited depends upon how far the inhibitor enters the liner cavity and the size of the hole in the inhibitor. This hole is provided in the inhibitor to allow the uninhibited jet-material to pass through unperturbed.

The inhibitor effectively isolates the jet's portion of interest from all other jet material. However, there is a small amount of low velocity liner-material that trails along the path of the uninhibited jet. This material consists of uncollapsed liner-material and the slug from the collapsed portion of the liner. This material can be deflected laterally by detonating a semi-circular deflector-charge placed on the outside of the shaped-charge at the base of the conical cavity (see Figure B.1).

Figure B.2 shows a radiograph of the forward portion of the normal jet produced by the shaped-charge shown in Figure B.1 (without the inhibitor and semi-circular deflector-charge in place). The section labeled "portion of interest" contains the material for the desired energy-level described earlier in this report. Note that, in addition to the customary stretching-jet material, this particular shaped-charge produces a precursor ahead of the portion of interest. The authors desired to isolate the portion of interest from all other jet material. Therefore, in addition to inhibiting the formation of a major portion of the stretching jet, the precursor also had to be eliminated.

This elimination was done by placing 114 mm of polyethylene in the jet's path prior to impacting the 105 mm round. Also a steel plate, 25.4 mm thick with a 38.1 mm diameter hole through it, was placed on top of the polyethylene to trap the deflected low-velocity liner-material. Figure B.3 presents a radiograph, taken at a later time than the radiograph shown in Figure B.2, showing the effect of the arrangement (see Figure B.1) upon the jet. Note that the portion of interest is completely devoid of precursor material and stretching jet except for the two particles that are contained within the portion of interest. Absence of deflected low-velocity liner-material was validated by a witness plate (see Figure B.4) which was free of impacts other than that produced by the lead particles.

PRECEDING PAGE BLANK-NOT FILMED

A photograph of the overall test arrangement used for the impact study is shown in Figure B.5. This photograph shows velocity screens for both the base and the nose at the projectile. However, no reliable readings were obtained for the screens associated with the projectile's nose.

The second set of hypervelocity particles employed steel disks which are propelled by an air-cavity charge. Figure B.6 shows a cross-sectional drawing of such a charge. Reference 18 showed that the mass and velocity of the propelled disk can be varied by charging the height of the air-cavity. Figure B.7 shows a radiograph of the hypervelocity disk associated with an air-cavity height of 5.08 mm. In this radiograph the disk is about the same distance from the base of the charge as used in test No. 13. Figure B.8 shows photographs of the arrangements used for tests No. 12 and 13. Again, the velocity screens for the nose did not function properly.

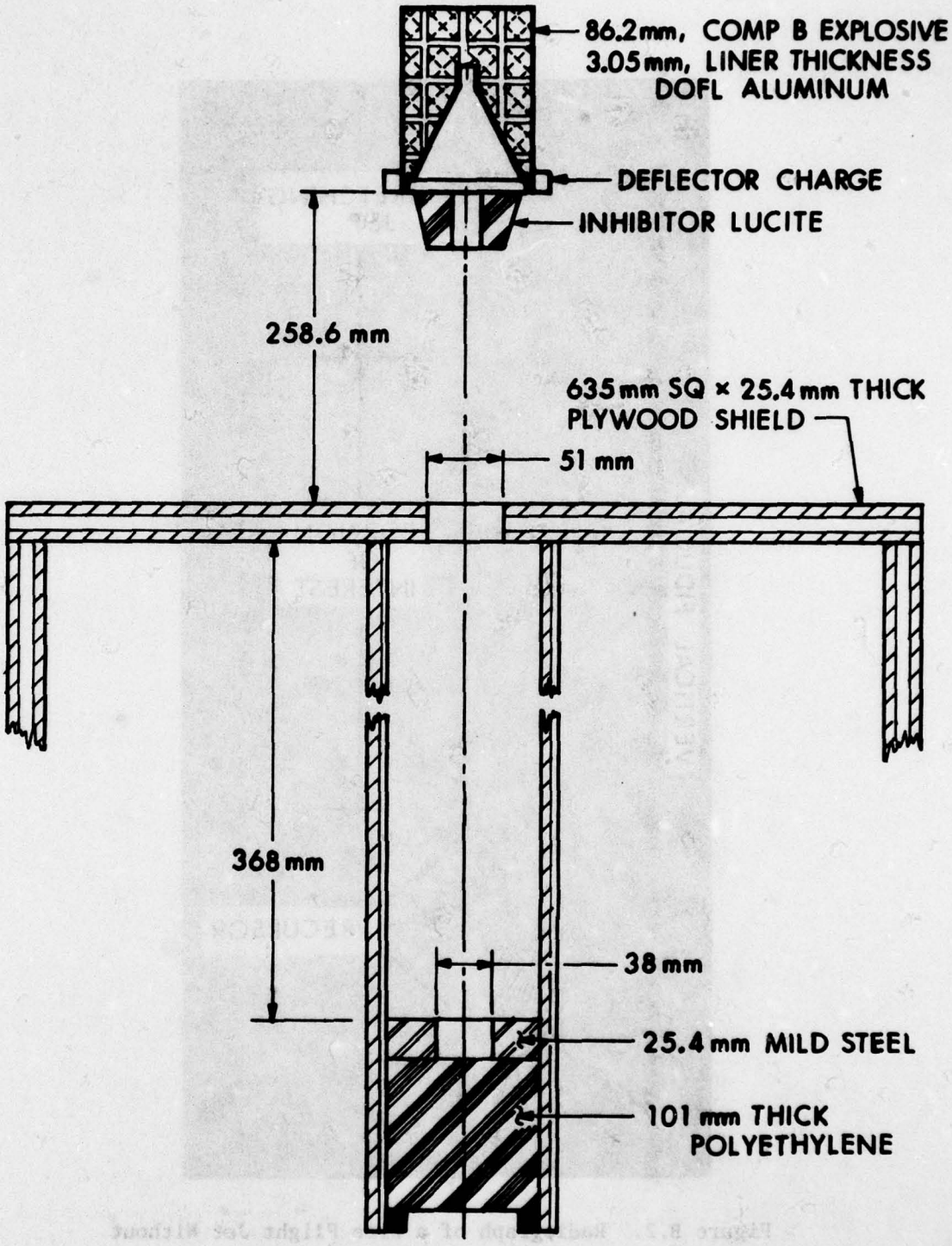

Figure B.1. Schematic Diagram of Arrangement Used for Obtaining a Hypervelocity "Rod"

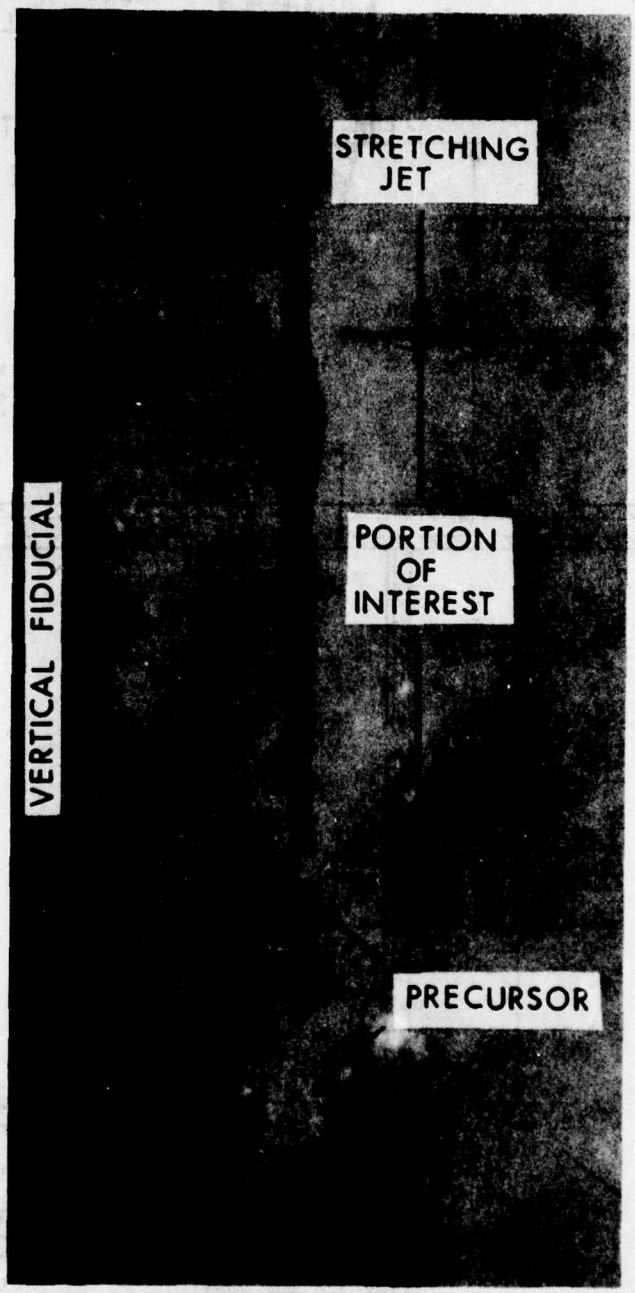

Figure B.2. Radiograph of a Free Flight Jet Without an Inhibitor

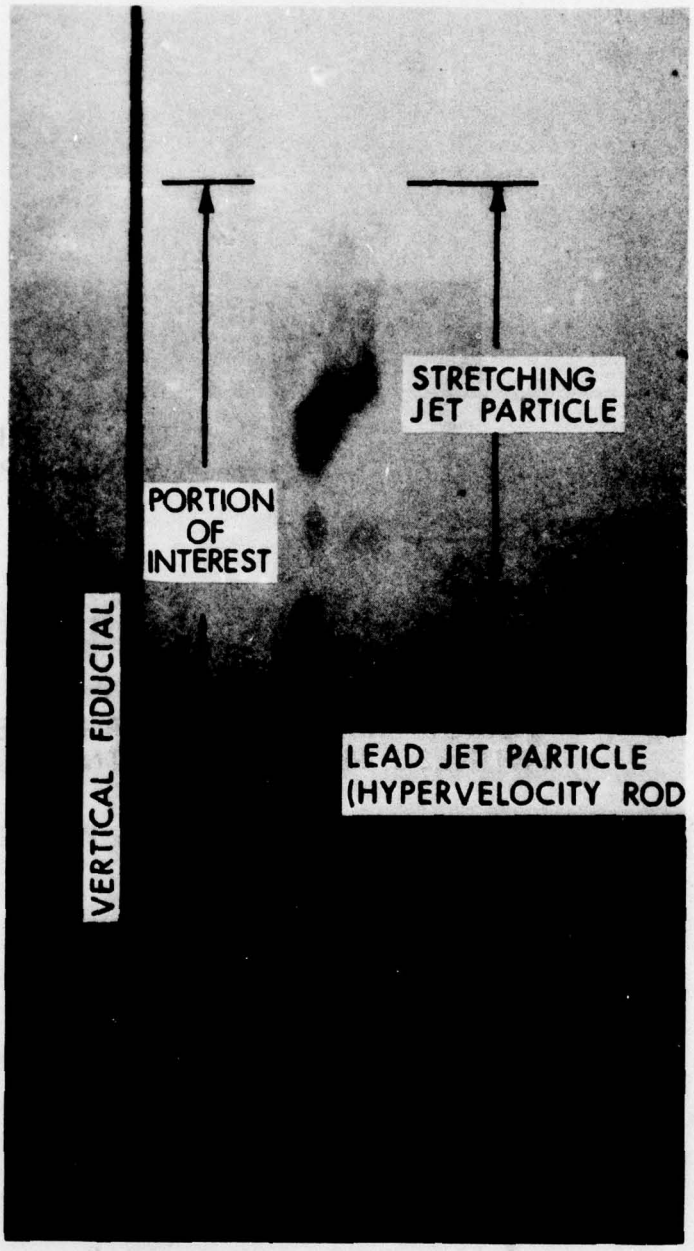

Figure B.3. Radiograph of an Inhibited Jet After Passing Through the Material Shown in Figure C.1

Figure B.4. Photograph of Steel Witness-Plates Associated With the Jet Shown in Figure B.3

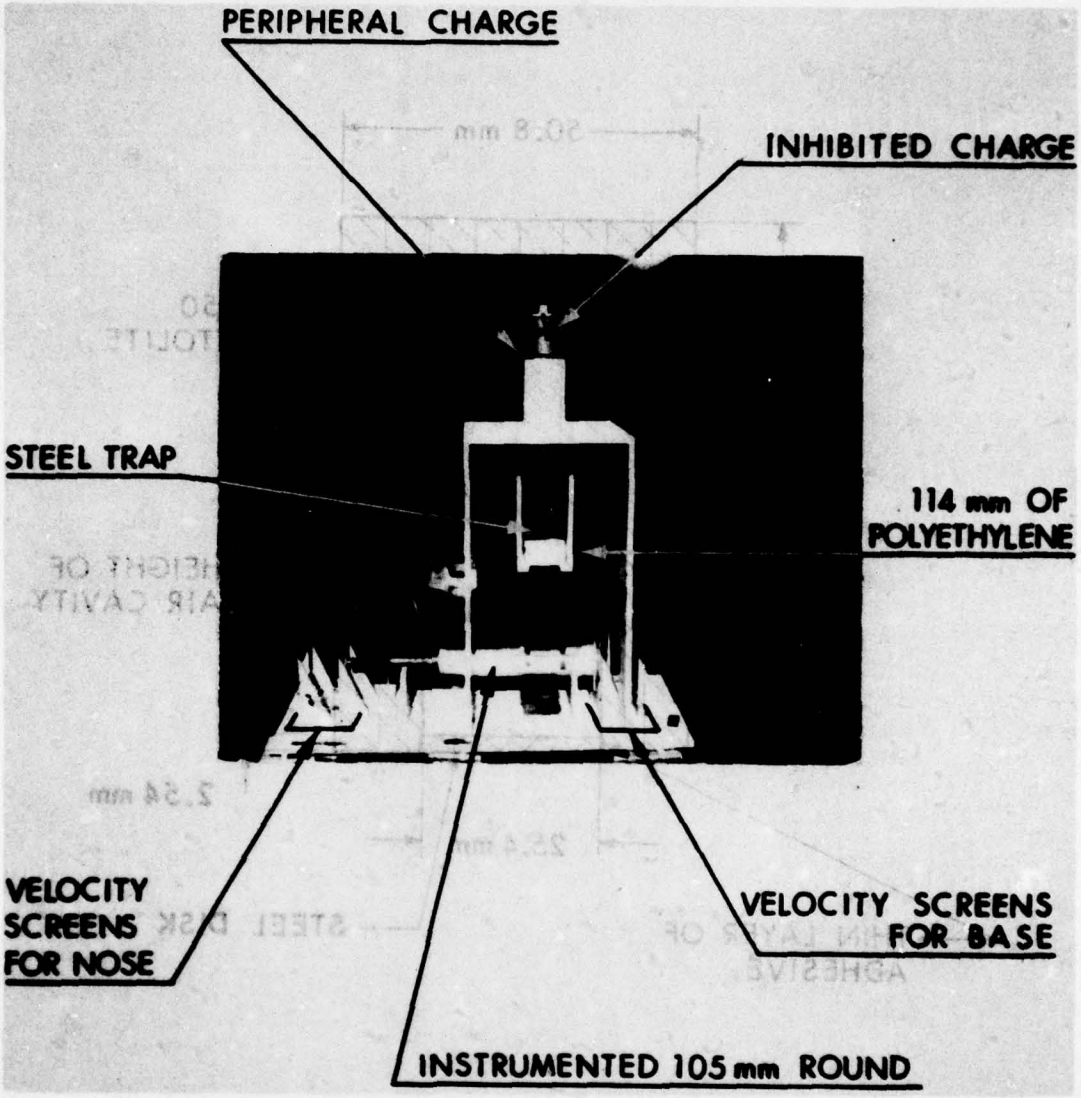

Figure B.5. Photograph of Overall Arrangement for Test No. 11

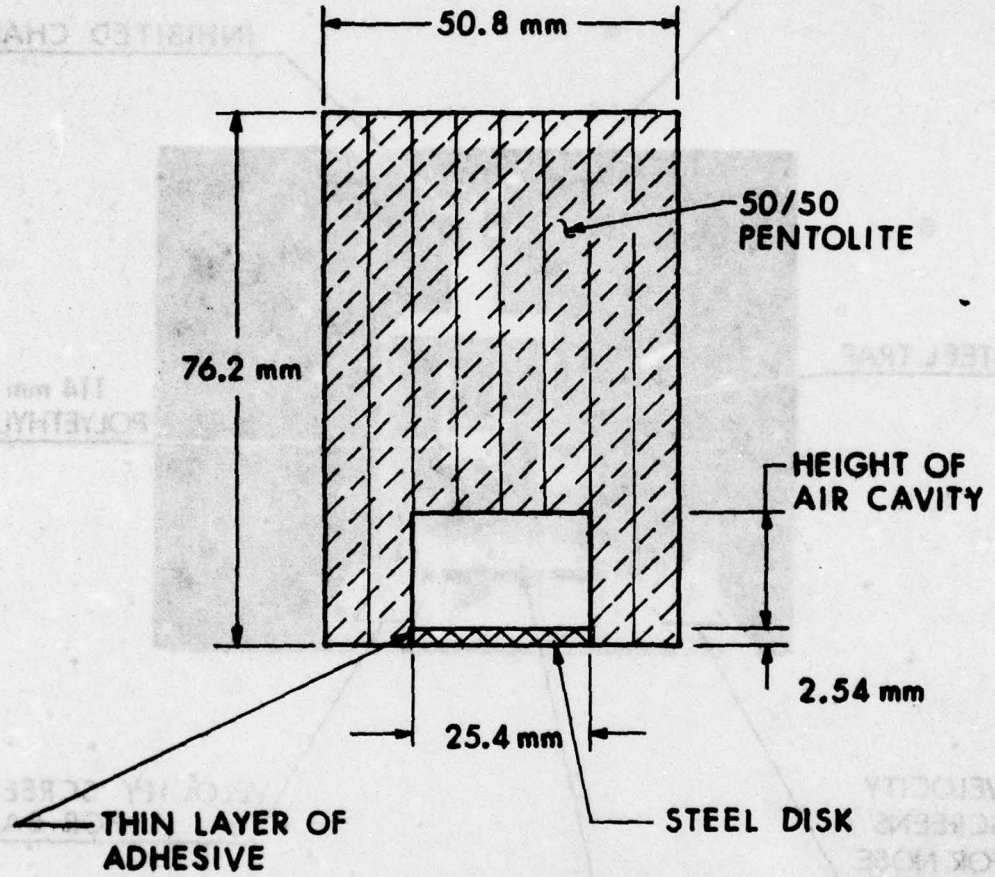

Figure B.6. Schematic Diagram of Air-Cavity Charges Used for Producing Hypervelocity Disks

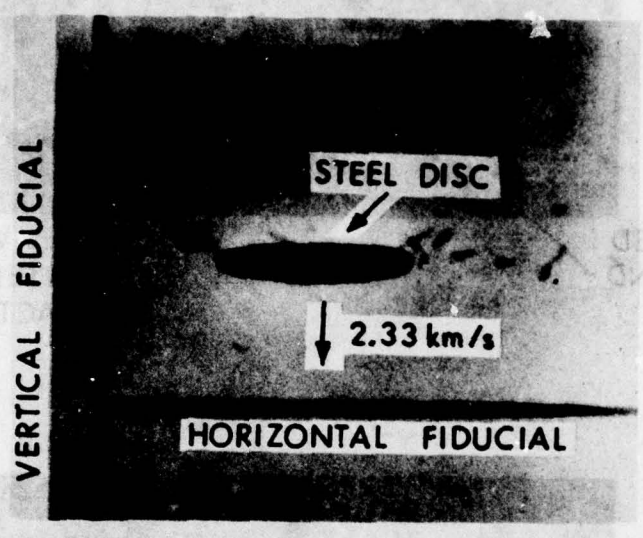

Figure B.7. Radiograph Taken of a Free Flight Hypervelocity Disk Associated With an Air-Cavity Depth of 7.62 mm

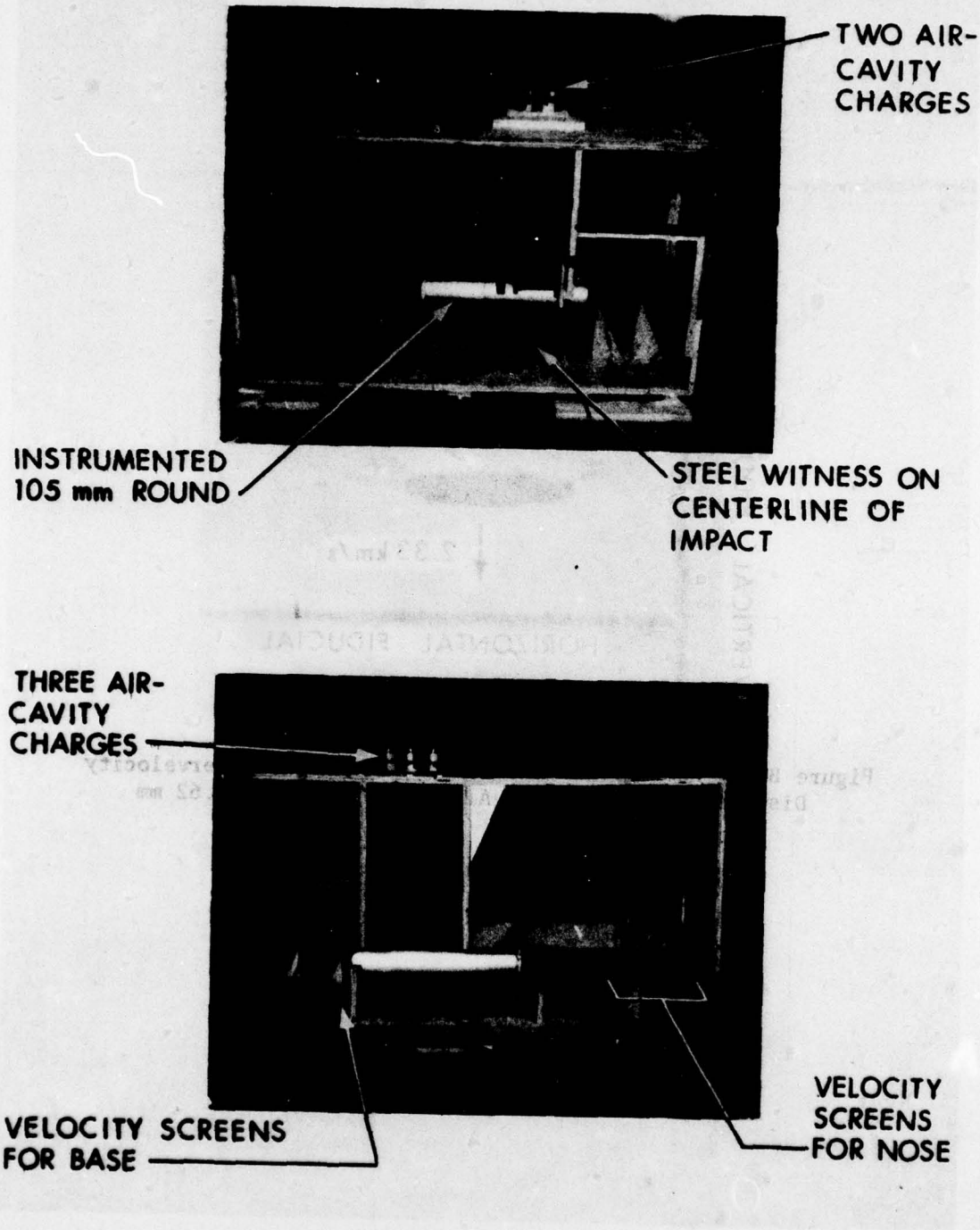

Figure B.8. Photographs of Overall Arrangement for Tests No. 12 and 13

APPENDIX C

IONIZATION PROBE TEST

A direct measure of the propagation rates within a propellant bed initiated by a shaped-charge jet was obtained using ionization probes imbedded within the propellant bed. Figure C.1 shows a schematic diagram of the test arrangement.

The 81 mm shaped-charge jet has a tip velocity around 7.6 km/s and a jet diameter ≃ 5 mm at that standoff distance (2.3) cone diameters). The amount of deposited energy is around 100 kilojoules. This condition was selected as being an extreme case for jet initiation of a propellant bed.

The ionization probe consisted of a twisted pair of cotton sheathed, 0.30 mm diameter copper-wires. The temperatures associated with the propagating disturbance burn off the thin cotton sheath and short circuit the pair of wires. The leads from each probe were run along the interface between the propellant bed and the plywood cover. The plywood cover was used to shield the leads from any fragments or detonation products associated with the detonation of the shaped charge. Each probe lead was connected to an oscilloscope which had an open-shutter camera attached.

The camera's film recorded the oscilloscope's wave form which started when the jet passed through the start trigger (a thin sandwich of brass, Mylar® and brass). After starting, each signal from an ionization probe would cause a blip to occur at some location on the waveform. The time between each signal was obtained by measuring the distance along the wave form between each blip. Malfunction of any single probe would be readily seen since consecutive probes have opposite polarity.

The measured times are listed in Table C.I and the computed average-velocity between stations is also given. These velocities were computed using the fact that the jet requires 3.3 ± 0.1 μs to travel the distance from the trigger (t ≡ 0) to the top of the propellant bed.

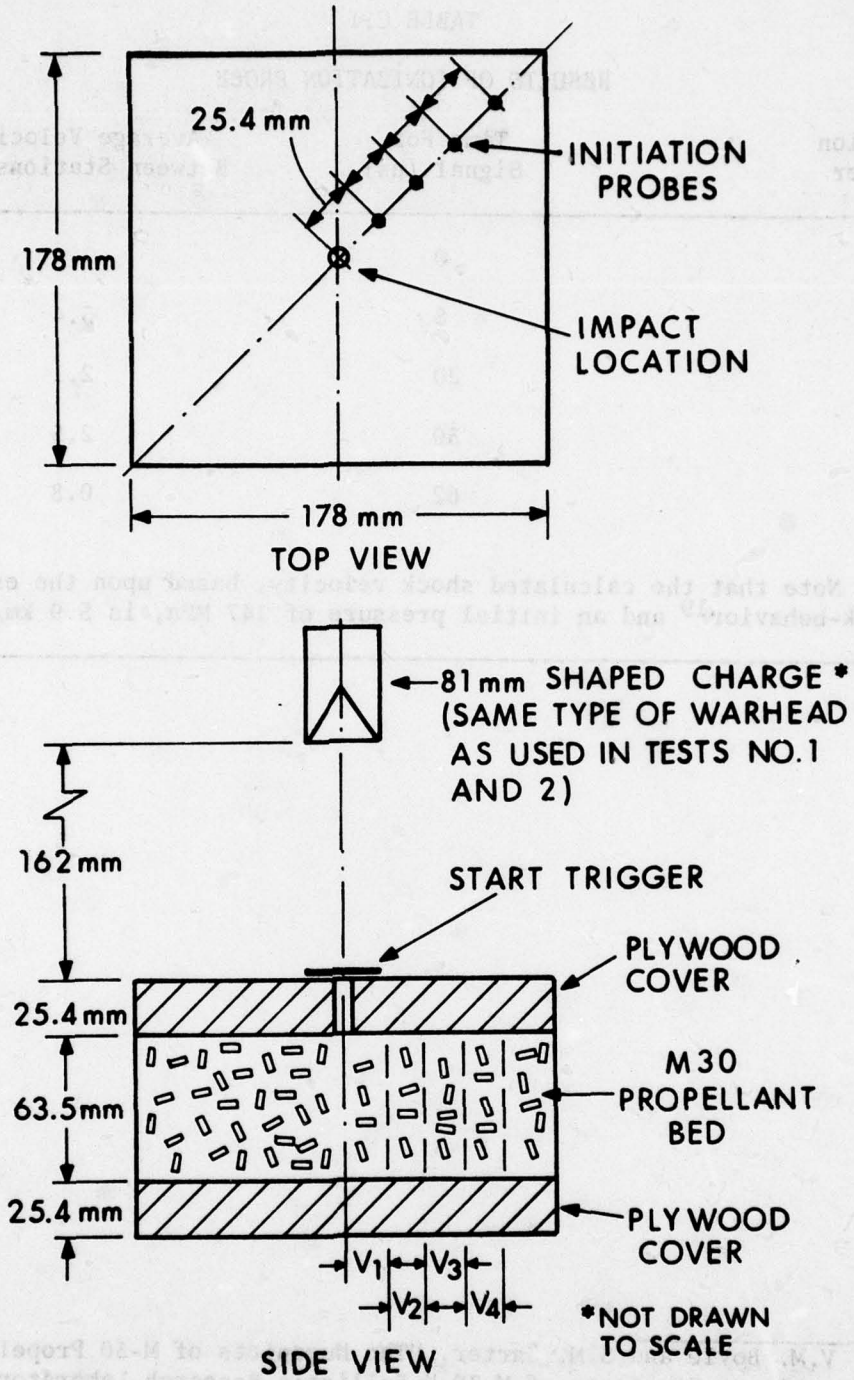

Figure C.1. Schematic Diagram of Arrangement Used for Ionization-Probe Test

PRECEDING PAGE BLANK-NOT FILMED

TABLE C.I

RESULTS OF IONIZATION PROBE

Station Number	Time For Signal (μs)	Average Velocity Between Stations (km/s)
0	0	
1	8	5.4
2	20	2.1
3	30	2.5
4	62	0.8

Note that the calculated shock velocity, based upon the estimated shock-behavior[19] and an initial pressure of 147 MPa, is 5.9 km/s.

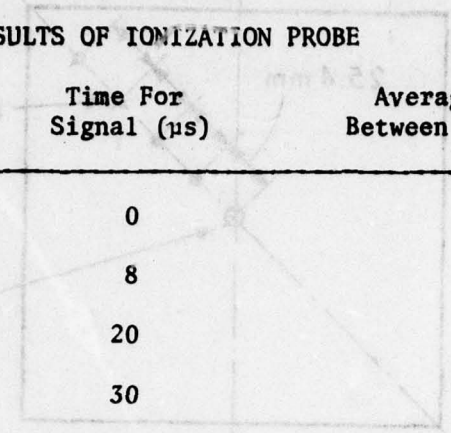

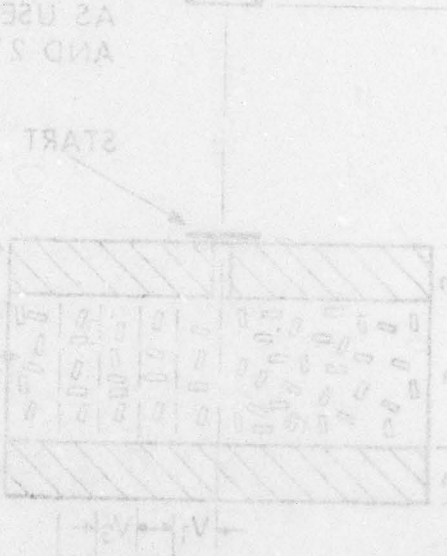

19. V.M. Boyle and S.M. Carter, "The Hugoniots of M-30 Propellant and an Inert Simulator of M-30," Ballistic Research Laboratory, IMR No. 351, February 1975. (not available)

DISTRIBUTION LIST

No. of Copies	Organization
12	Commander Defense Documentation Center ATTN: DDC-TCA Cameron Station Alexandria, VA 22314
1	Commander US Army Materiel Development and Readiness Command ATTN: DRCDMD-ST 5001 Eisenhower Avenue Alexandria, VA 22333
1	Commander US Army Aviation Research and Development Command ATTN: DRSAV-E 12th and Spruce Streets St. Louis, MO 63166
1	Director US Army Air Mobility Research and Development Laboratory Ames Research Center Moffett Field, CA 94035
1	Commander US Army Electronics Rsch and Development Command Technical Support Activity ATTN: DELSD-L Fort Monmouth, NJ 07703
1	Commander US Army Communications Rsch and Development Command ATTN: DRDCO-SGS Fort Monmouth, NJ 07703
1	Commander US Army Missile Research and Development Command ATTN: DRDMI-R Redstone Arsenal, AL 35809
1	Commander US Army Missile Materiel Readiness Command ATTN: DRSMI-AOM Redstone Arsenal, AL 35809
4	Commander US Army Tank Automotive Research & Development Cmd ATTN: DRDTA-UL DRDTA-RCKA, Mr. H.Spiro DRDTA-ZE, Mr. C.Bradley DRDTA-RC, Mr. E.Jackovich Warren, MI 48090
1	Commander US Army Armament Materiel Readiness Command ATTN: DRSAR-LEP-L Rock Island, IL 61299
7	Commander US Army Armament Research and Development Command ATTN: Mr. T. Stevens Mr. G. Randers-Pehrson Dr. N. Clark Mr. J. Hershkowitz Mr. J. Pearson DRDAR-TSS (2 cys) Dover, NJ 07801
2	Commander US Army Materials and Mechanics Research Center ATTN: DRXMR-RF, J. Mescall Tech Lib Watertown, MA 02172
1	Project Manager XM1 Tank System ATTN: DRCPM-SA Warren, MI 48090

DISTRIBUTION LIST

No. of Copies	Organization
1	Director US Army TRADOC Systems Analysis Activity ATTN: ATAA-SL, Tech Lib White Sands Missile Range NM 88002
1	Assistant Secretary of the Army (R&D) ATTN: Asst for Research Washington, DC 20310
2	HQDA (DAMA-ZA; DAMA-AR) Washington, DC 20310
1	Commander US Army Research Office P. O. Box 12211 Research Triangle Park NC 27709
2	Chief of Naval Research Department of the Navy ATTN: Code 427 Code 470 Washington, DC 20325
2	Commander Naval Air Systems Command ATTN: Code AIR-310 Code AIR-350 Washington, DC 20360
1	Commander Naval Ordnance Systems Command ATTN: Code ORD-0332 Washington, DC 20360
2	Commander Naval Surface Weapons Center ATTN: Code DG-50 Code DX-21 Dahlgren, VA 22448
1	Commander Naval Surface Weapons Center ATTN: Code 730, Lib Silver Spring, MD 20910
2	Commander Naval Weapons Center ATTN: Code 4057 Code 45, Tech Lib China Lake, CA 93555
1	Commander Naval Research Laboratory Washington, DC 20375
1	USAF/AFRDDA Washington, DC 20311
1	AFSC/SDW Andrews AFB, DC 20311
1	US Air Force Academy ATTN: Code FJS-41 (NC) Tech Lib Colorado Springs, CO 80840
1	AFATL/DLJW (J. Foster) Eglin AFB, FL 32542
1	AFWL (SUL, LT Tennant) Kirtland AFB, NM 87116
1	AFAL/AVW Wright-Patterson AFB, OH 45433
1	AFLC/MMWMC Wright-Patterson AFB, OH 45433
2	Battelle Columbus Laboratories ATTN: Mr. Joseph E. Backofen Dr. Dale Trott 505 King Avenue Columbus, OH 43201

DISTRIBUTION LIST

No. of Copies	Organization
6	Director Lawrence Livermore Laboratory ATTN: Dr. J. Kury Dr. M. Wilkins Dr. E. Lee Dr. H. Hornig Dr. J. Knowles Tech Lib P. O. Box 808 Los Alamos, NM 87544
3	Chrysler Corporation ATTN: J. Yeats M. Hoffman R. Auyer 6000 E. Second Street Hopkins, MN 55343
1	Physics International Corp ATTN: Dr. L. Behrmann 2700 Merced Street San Leandro, CA 94577
1	Sandia Laboratories ATTN: Dr. W. Herrmann Albuquerque, NM 87115
1	Shock Hydrodynamics ATTN: Dr. L. Zernow 4710-4716 Vineland Avenue North Hollywood, CA 91602
1	Systems, Science & Software ATTN: Dr. R. Sedgwick P. O. Box 1620 La Jolla, CA 92037
1	Drexel Institute of Technology Wave Propagation Rsch Center ATTN: Prof. P. Chou Philadelphia, PA 19104
2	University of California Los Alamos Scientific Lab ATTN: Dr. J. Walsh Tech Lib P. O. Box 1663 Los Alamos, NM 87544
1	University of Denver Denver Research Institute ATTN: Mr. R. F. Recht 2390 S. University Boulevard Denver, CO 80210
	Aberdeen Proving Ground
	Dir, USAMSAA ATTN: J. Sperrazza B. Oehrli G. Johnson
	Cdr, USATECOM ATTN: DRSTE-SG-H